


January 2012

Corrosion Evaluation and Durability Estimation of Aluminized Steel Drainage Pipes

Mersedeh Akhoondan

University of South Florida, makhoond@mail.usf.edu

Follow this and additional works at: <http://scholarcommons.usf.edu/etd>

 Part of the [Civil Engineering Commons](#), and the [Materials Science and Engineering Commons](#)

Scholar Commons Citation

Akhoondan, Mersedeh, "Corrosion Evaluation and Durability Estimation of Aluminized Steel Drainage Pipes" (2012). *Graduate Theses and Dissertations*.

<http://scholarcommons.usf.edu/etd/4273>

This Dissertation is brought to you for free and open access by the Graduate School at Scholar Commons. It has been accepted for inclusion in Graduate Theses and Dissertations by an authorized administrator of Scholar Commons. For more information, please contact scholarcommons@usf.edu.

Corrosion Evaluation and Durability Estimation of
Aluminized Steel Drainage Pipes

by

Mersedeh Akhoondan

A dissertation submitted in partial fulfillment
of the requirements for the degree of
Doctor of Philosophy
Department of Civil and Environmental Engineering
College of Engineering
University of South Florida

Major Professor: Alberto A. Sagüés, Ph.D.
Delcie Durham, Ph.D.
Yusuf Emirov, Ph.D.
Xiao Li, Ph.D.
Gray Mullins, Ph.D.
Rajan Sen, Ph.D.

Date of Approval:
October 22, 2012

Keywords: Culverts, Service Life, Limestone Backfill, Natural Waters, Coating

Copyright © 2012, Mersedeh Akhoondan

DEDICATION

This work is dedicated to:

My best friend and soul mate, Emir Modarres, who has accompanied me through all the ups and downs of my life and without his unconditional love and support this work would not be possible.

My dear parents, Ali Akhoondan and Dr. Taraneh Bahary, and my beloved sister, Dr. Mandana Akhoondan, who believed in me, not just as a daughter and a sister, but as someone who can make a difference.

My dear professor, Dr. Alberto Sagüés, who, not only introduced me to the exciting world of corrosion science, but also taught me many valuable life lessons along the way.

My dear Uncle Majid, the rest of my family, colleagues, and friends for their help and encouragement.

ACKNOWLEDGMENTS

I would like to sincerely thank Dr. Alberto Sagüés, my mentor and supervisor for his sage advice, insightful criticism, and patient encouragement. Also, I wish to express my appreciation to Dr. Durham, Dr. Emirov, Dr. Li, Dr. Mullins, Dr. Nachabe Dr. Sen and Dr. Volinsky for serving as supervisory committee members and for their crucial remarks.

I gratefully acknowledge the support from the Florida Department of Transportation and the Federal Highway Administration in funding this research. Notably, I thank Mr. Mario Paredes, Project Manager, for his assistance and for providing us with the means to accomplish the project goal. The opinions, findings, and conclusions expressed here are those of the author and not necessarily those of the supporting agency. Special thanks to the University of South Florida Nanotechnology Research & Education Center for their help and for allowing me access to state-of-the-art instruments. I also appreciate the help of undergraduate assistants (Andrew Filippi, David Stump, Arish Sajwani, Paul Clark, Patrick Doyle, Randy Guillen, and Cesar Castaneda) for the acquisition of experimental data.

TABLE OF CONTENTS

LIST OF TABLES	iii
LIST OF FIGURES	iv
ABSTRACT	ix
1. BACKGROUND	1
1.1 Aluminized Steel Pipe	2
1.2 Relevant Corrosion Principles.....	5
1.2.1 Definitions	5
1.2.2 Polarization Behavior of Electrochemical Systems	7
1.2.3 Electrochemical Measurement Methods	10
1.2.4 Passivity.....	12
1.2.5 Pitting Corrosion.....	15
1.3 Corrosion Studies of Aluminum and Aluminized Steel	16
1.3.1 Corrosion of Aluminum.....	16
1.3.2 Corrosion of Aluminum-Iron Alloys.....	19
1.3.3 Corrosion Performance of Aluminized Steel.....	21
2. INTRODUCTION	28
2.1 Recent Corrosion Failures	28
2.2 Understanding Corrosion Causes and Open Issues	30
2.3 Objectives and Research Scope.....	34
3. EXAMINATION OF FIELD EVIDENCE	36
4. MECHANICAL DISTRESS IN SRAP RIBS.....	43
5. FORMULATION OF TEST SOLUTIONS.....	49
5.1 Specifications of Environmental Limits.....	49
5.2 Replication of Field Conditions	51
6. MODE A: EFFECT OF MECHANICAL DISTRESS ON CORROSION PERFORMANCE OF ALUMINIZED STEEL	54
6.1 Comparative Corrosion Evaluation of Severely Deformed and Flat Aluminized Steel	54
6.2 Comparative Corrosion Evaluation of Spiral Ribbed and Plain Corrugated Pipes	60
6.2.1 Preliminary Tests	60

6.2.2 SRAP vs PCAP in Non-flowing Waters	62
6.2.3 SRAP in Flowing Waters	71
6.3 Corrosion and Simulated Severe Manufacturing Distress.....	73
6.3.1 Laboratory Experiments	73
6.3.2 Corrosion Propagation Mechanism Modeling.....	80
7. MODE B: MECHANISM OF CORROSION PERFORMANCE IN WATER	
CONTACTING SAND AND LIMESTONE.....	91
7.1 Corrosion in Sandy Soil	91
7.2 Corrosion in Limestone Backfill.....	96
7.2.1 Introduction	96
7.2.2 Experimental Procedure.....	98
7.2.3 Results and Discussion.....	103
7.2.3.1 Solution pH.....	103
7.2.3.2 Corrosion Development - Physical Observations .	104
7.2.3.3 Corrosion Development - Electrochemical	
Behavior	106
7.2.3.4 Interpreting EIS Data: Control Specimens and	
Stage I of Flowing Water Condition	110
7.2.3.5 Interpreting EIS Data: Stage II.....	122
7.2.3.6 Comparison of EIS Results and Metallography	130
7.3 Summary	132
8. GENERAL DISCUSSION	135
8.1 Mode A Corrosion Issues.....	135
8.2 Mode B Corrosion Issues.....	138
9. CONCLUSIONS	140
10. FUTURE WORK.....	143
REFERENCES	145
APPENDICES	151
Appendix 1: Sample Polarization Diagrams of Al and Steel.....	152
Appendix 2: Example of Fit and EIS Raw Data for EIS Interpretation	
of Stage I, Stage II and Control Specimens.....	155
Appendix 3: Corrosion and Simulated Severe Manufacturing Distress..	174
Appendix 4: Limestone Composition Analysis by X-ray Fluorescence	
Spectrometry.	177
Appendix 5: Corrosion of Plain Corrugated Galvanized Steel Pipe	
Joining SRAP Segments	178
ABOUT THE AUTHOR.....	END PAGE

LIST OF TABLES

Table 1: Possible reactions in the Al-H ₂ O system	19
Table 2: Field failures.	28
Table 3: System of equations applied in the model	84
Table 4: Input parameters for finite element modeling.....	86
Table 5: List of specimens for limestone experiment.....	102
Table A-1: Exploratory polarization tests	154
Table A-2: EIS fit parameter values, SP 8	155
Table A-3: EIS fit values for Stage II.....	157
Table A-4: EIS analysis parameters for SP1.	162
Table A-5: EIS analysis parameters for SP2.	163
Table A-6: EIS analysis parameters for SP3.	163
Table A-7: EIS analysis parameters for SP4.	164
Table A-8: EIS analysis parameters for SP5.	165
Table A-9: EIS analysis parameters for SP6.	166
Table A-10: EIS analysis parameters for SP7.	167
Table A-11: EIS analysis parameters for SP8.	168
Table A-12: List of all specimens used for metallography analysis.....	169
Table A-13: Limestone composition	177

LIST OF FIGURES

Figure 1: Aluminized steel type 2 pipe.....	3
Figure 2: SRAP manufacturing process	5
Figure 3: Simple schematic of corrosion process in water.....	6
Figure 4: Simple polarization diagram showing anodic polarization functions and corrosion potential.	9
Figure 5: Polarization diagram of passive metals	13
Figure 6: Schematic of the passive film on aluminum.....	13
Figure 7: Pourbaix diagram for aluminum at 25 ⁰ C.....	14
Figure 8: Pitting corrosion process in NaCl solution	15
Figure 9: Estimated service life vs. pH at resistivity of 2.5 kΩ-cm	23
Figure 10: Premature failure of installed SRAP after 2 years of service at City of Largo, FL.....	29
Figure 11: Premature failure of installed SRAP after 10 years in service	30
Figure 12: Metallographic cross section of bent region and flat region of a ribbed specimen cut out from metal coupon..	37
Figure 13: Location of the bore, extracted coupon, and metallographic cross section of the coupon.....	39
Figure 14: The pipe coupon from a site that was near SR 212 failure.....	41
Figure 15: Photograph of in situ pipe located in Jacksonville, near Highland Glen and Beach Blvd..	42
Figure 16: Comparison of cumulative distributions of rib radius of curvature between samples from newly produced aluminized steel type 2 pipes made by two different manufacturers and from a pipe in service for 10 years at the Curlew Rd. site.....	45

Figure 17: Specimens before and after tensile test.	46
Figure 18: Metallographic cross-section of bend region	47
Figure 19: Metallographic cross-section of tensile test at the necking zone	48
Figure 20: Tensile specimens before and after few days immersed in simulated natural waters	48
Figure 21: The FDOT chart for estimation of years to perforation of 16-gage aluminized steel Type 2 culvert pipes.	50
Figure 22: Typical pipe layout.....	52
Figure 23: Dimple specimens	55
Figure 24: Coating damage due to deformation of aluminized steel type 2	56
Figure 25: Three-electrode cell configuration for dimple specimens.....	58
Figure 26: Visual comparison of corrosion development in formed and flat specimens immersed in solution S at 26 days of exposure.....	59
Figure 27: Three-electrode cell configuration for the SRAP experiment.....	61
Figure 28: Corrosion progression of small ribbed specimens in solution S	62
Figure 29: Average E_{OC} for small size SRAP specimens	63
Figure 30: Large SRAP specimens in a large bin.....	64
Figure 31: PCAP and SRAP specimens in solution S and S^+ after ~700 days of exposure	66
Figure 32: Pits and corrosion product at ribbed regions of an in-situ SRAP specimen in S^+ solution after ~300 days of exposure.	66
Figure 33: Metallographic cross-section of SRAP at rib regions after two years of exposure to solution S.....	67
Figure 34: Average E_{OC} of SRAP and PCAP in S and S^+ solution.....	68
Figure 35: Apparent corrosion current density of SRAP and PCAP in solution S and S^+	69
Figure 36: E_{OC} of quadruplicate SRAP specimens in solution S.....	70

Figure 37: Apparent corrosion current density of quadruplicate SRAP specimens in solution S	70
Figure 38: Average E_{OC} of SRAP in solution S -flowing vs. non-flowing condition.....	72
Figure 39: Apparent corrosion current density of SRAP in solution S -flowing vs. non-flowing condition.....	72
Figure 40: Exposed cut edge experiment set up to simulate severe manufacturing damage.	75
Figure 41: E_{OC} of open cut edge experiments	76
Figure 42: Macrocell current compared to apparent corrosion current density obtained from EIS tests.....	77
Figure 43: Exposed cut edge experiment	79
Figure 44: Metallographic cross section of the edges of aluminized steel specimens in solution S and S+	80
Figure 45: Speculative scenario of conditions at cut edge or localized aluminized coating break	81
Figure 46: Conditions applied to an aluminized specimen with cut edges immersed in an electrolyte under steady state condition.....	87
Figure 47: Computer model for potential distribution	88
Figure 48: Computer model results: streamline: total current density, arrow: direction of current, and contour: potential	88
Figure 49: Aluminum anodic current densities as the function of X-axis for aluminum boundary.....	89
Figure 50: Potential vs. saturated calomel ref. electrode as the function of X-axis for aluminum boundary..	89
Figure 51: Sand experiment set up.....	93
Figure 52: pH measured for triplicate specimens in saturated sand experiment.	93
Figure 53: Conductivity measured for triplicate specimens in saturated sand experiment.	94
Figure 54: Average E_{OC} in saturated sand and moist sand experiments.....	94

Figure 55: Apparent current densities in saturated sand and moist sand experiment.	95
Figure 56: Bright appearance of specimen after 250 days of exposure to saturated-sand-water condition.	95
Figure 57: Limestone-cell configuration sketch.....	101
Figure 58: pH evolution of control specimens over time	104
Figure 59: Surface discoloration over time	105
Figure 60: Coating condition after ~75 days exposure to flowing water	105
Figure 61: E_{OC} evolution for limestone specimens.....	107
Figure 62: Typical EIS behavior of specimens exposed to limestone in cells with flowing water.....	108
Figure 63: Stage I impedance behavior.....	109
Figure 64: Stage II impedance behavior.....	109
Figure 65: General concepts in developing an analog equivalent circuit for Stage I behavior.....	113
Figure 66: Simplification of preliminary circuit	114
Figure 67: Equivalent analog model for impedance response of a two step reaction system.....	117
Figure 68: Final analog equivalent circuit to interpret the EIS data for Stage I.....	118
Figure 69: The evolution of the CPE_1 parameters Y_0 and n during Stage I.....	119
Figure 70: Evolution of R_1 during Stage I for all specimens tested.....	120
Figure 71: Nominal film thickness during Stage I.....	121
Figure 72: Analog equivalent circuit to interpret the EIS data for Stage I	122
Figure 73: Typical evolution of the CPE_3 and n during Stage II.....	123
Figure 74: Typical evolution of R_{p3} during Stage II.....	123
Figure 75: Typical evolution of i_{corr} during Stage II.....	125

Figure 76: Estimated corrosion current density as a function of time for both stages.	126
Figure 77: Accumulated thickness loss as a function of time starting at Stage II.....	130
Figure 78: Total coating loss as a function of time measured by EIS data and by direction observation	133
Figure 79: Scenario of corrosion progression under flowing water condition....	134
Figure A-1: Polarization diagrams for aluminized steel with sealed edges and steel in S solution.	154
Figure A-2: Nyquist diagrams, bode, and phase angle for Stage I.	156
Figure A-3: Nyquist diagrams, bode, and phase angle for Stage II.	158
Figure A-4: Nyquist diagrams for control specimens over 137 days of exposure.....	159
Figure A-5: Typical fit for late exposure days of control specimens.....	160
Figure A-6: Typical fit for early exposure days of control specimens.....	161
Figure A-7: Representative metallographic cross section used for direct coating loss measurements	170
Figure A-8: Potential evolution for six coupon specimens	173
Figure A-9: Specimens with exposed edges and their counterpart specimen. .	174
Figure A-10: Metallographic cross section of the edges of aluminized steel specimens in solution S and S+	175
Figure A-11: Metallographic cross section after etching with 1% Nital solution.....	176
Figure A-12: Representative nyquist plot of the EIS response of exposed edge specimens in S and S+ solutions.	176
Figure A-13: Snap shot of a video from inside a pipe that shows plain corrugated galvanized pipe is joining the segments of SRAP.	178
Figure A-14: Snap shots of a video from inside a pipe with severe corrosion of plain corrugated galvanized pipes.....	178

ABSTRACT

Aluminized steel pipes are expected to have a long service life, e.g. 75 years. Spiral ribbed aluminized pipes (SRAP) have been widely specified and used by the Florida Department of Transportation (FDOT) for drainage of runoff water. Confidence in the long term durability of SRAP has been challenged by recent unexpected early corrosion failures in various Florida locations. SRAP premature corrosion incidents have occurred in two modalities. Mode A has taken place in near-neutral soil environments and has often been associated with either gross manufacturing defects (i.e. helical cuts) or corrosion concentration at or near the ribs. Mode B took place in pipes in contact with limestone backfill and corrosion damage was in the form of perforations, not preferentially located at the ribs, and not necessarily associated with other deficiencies. These failures motivated this research. The objectives of this work are to establish to what extent the Mode A corrosion incidents can be ascribed to manufacturing defects, that can be rectified by appropriate quality control, as opposed to an intrinsic vulnerability to corrosion of regularly produced SRAP due to ordinary forming strains and to determine the mechanism responsible for Mode B corrosion including the role that limestone backfill played in that deterioration. To achieve those objectives, laboratory experiments were conducted to replicate the conditions for Mode A and Mode B. Overall, the findings of this and previous

work suggest that much of the corrosion damage observed in the Mode A incidents were promoted more by manufacturing deficiencies and less by any possible inherent susceptibility of corrosion at the ribs of SRAP that was produced following appropriate quality control. Experiments to explore the causes of Mode B corrosion showed that high pH values, sufficient to cause dissolution of the passive film on aluminum, can develop under exposure of limestone to flowing natural water. The findings substantiate, for the first time, an important vulnerability of aluminized steel in limestone soils and provide an explanation for the rapid onset deterioration observed at the field under Mode B. The findings also provide strong evidence in support of service guidelines to disallow the use of limestone bedding for aluminized steel pipe, including SRAP.

1. BACKGROUND

In recent years, from 2006 to 2011, the Florida Department of Transportation has spent over 9.5 million dollars on repair and rehabilitation of pipes including metal drainage pipes (Najafi et al., 2011). Structural performance of metal drainage pipes is affected by abrasion, backfill operations, improper choice of backfill material, presence of groundwater, level of compaction and compaction equipment used, and corrosion (Najafi et al., 2008). Premature replacement of buried metallic components is costly, not only because of the price of the new unit, but also because of the associated road demolition and service outage. Of the factors mentioned above, corrosion is a key source of long term deterioration. It is important to have in place reliable means of anticipating the extent of corrosion damage so that materials selection commensurate with the desired service life. This work is focused on better evaluating the corrosion performance of aluminized steel pipes, for which some unexpected corrosion damage incidents have occurred in recent years. This research work is a continuation of initial investigation aimed at identifying the causes of that deterioration, funded by Florida Department of Transportation (FDOT Project BD497). The findings of that work are detailed in its Final Report (Sagüés, 2009), to which reference is made throughout this document.

1.1 Aluminized Steel Pipe

Aluminized steel Type 2 is produced as a steel sheet hot-dip coated on both sides with commercially pure aluminum (ASTM A929 and AASHTO M274). The steel to be hot-dipped is degreased by alkali cleaning, or by heating it to 450-600 °C, followed by water rinsing, pickling, and water rinsing again (pretreatment process). Afterwards, the pretreated steel is cleaned by exposure to an H₂ gas atmosphere at high temperature (activating process). Cleaning the metal strip in a non-oxidizing/reducing atmosphere assures a pristine surface for coating adherence. At the end of the activating process, aluminum coating is continuously applied to the pretreated steel by hot-dipping in a closed environment at ~700 °C. The steel is annealed in the production line, and the coating thickness is controlled by the line speed, hot-dipping temperature, and air finishing. The reaction rate between molten aluminum and steel is relatively fast, forming a duplex coating on top of the steel substrate. According to the ASTM A929 and AASHTO M274 standard procedures, the final product must comply with a minimum coating weight of 1 oz/ft², which corresponds to a minimum coating thickness of ~40 μm, and minimum tensile and yield strengths of about 310 MPa and 228 MPa, respectively (Sagüés, 2009¹).

The process results in a dual coating, with an inner intermetallic brittle layer, ~15 μm thick, composed of Fe₂Al₅ (Kobayashi and Yakou, 2002) formed

¹ The author of the dissertation is a coauthor of this cited report. Material from reports prepared by the author of the dissertation is included as part of the text of this dissertation, as done in this paragraph, whenever appropriate.

next to the low carbon steel substrate , and a nearly pure outer soft aluminum-matrix layer ~30 μm thick (Figure 1). The outer layer contains intermetallic precipitates with 6-11 wt% Fe content (Caseres and Sagüés, 2005). Those precipitates constitute ~5% of the volume of the outer layer.

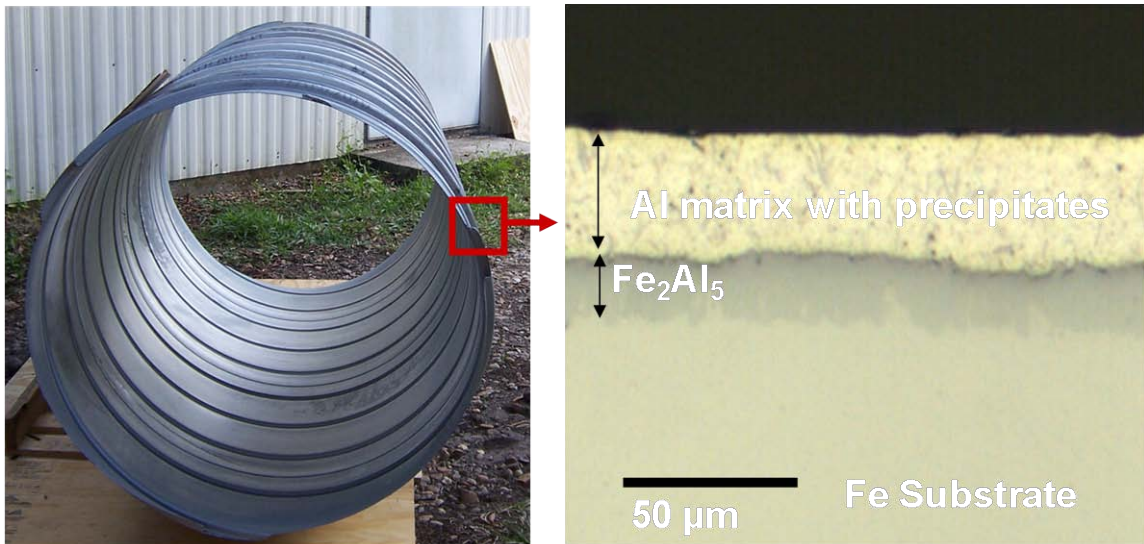


Figure 1: Aluminized steel type 2 pipe (Left). Metallographic cross section of aluminized steel (right).

The aluminum coating provides corrosion protection through the low corrosion rate of aluminum in mild environments where aluminum is passive, and also may provide galvanic protection to underlying steel in more aggressive environments where aluminum is active (Kimoto, 1999). For that reason, aluminized steel Type 2 is increasingly used for metallic drainage components in contact with natural waters.

Aluminized pipes are commonly ribbed or corrugated for structural strength. Ribbed pipes have better hydraulic efficiency and are often preferred. In the general process (ASTM 760) used to form spiral ribbed aluminized pipes

(SRAP) the stock aluminized sheet is rolled over a series of press dies while being lubricated with a soapy solution to decrease friction (Figure 2A). Such construction creates open type ribs as shown in Figure 2B. Interlocking folds are formed on the opposite side of the sheet. As the pipe is rolled into the spiral (Figure 2C), the interlocking fold connects with a corresponding fold on the rib. These formed, not-welded, interlocks are called lock-seams and join the segments of spiral pipes.

Typically, aluminized steel pipes have shown good durability and are expected to have long service life, e.g. 75 years. Previous work by Cerlanek and Powers (Cerlanek and Powers, 1993) estimated that aluminized steel exceeded the service of galvanized steel pipes by two to six times. The advantage of aluminized steel over galvanized steel, in part, reflects that; in galvanized steel the zinc coating is subject to continuous corrosion to provide protection, and in aluminized steel corrosion resistance is provided mainly by a thermodynamically stable thin passive film of aluminum oxide. If this film is damaged or removed by abrasion, another layer of oxide is expected to form rapidly and prevent further corrosion. A detailed review of earlier evidence for aluminized durability has been presented in the literature review section. Based on those expectations, and on the prior evidence of good performance, SRAP have been widely specified and used by the Florida Department of Transportation (FDOT) for drainage of runoff water.

However, in recent years, unexpected early failures of SRAP, due to corrosion, occurred in various Florida locations. These failures are fully

discussed in later chapters. The next section, reviews the relevant corrosion principals and definitions that will be used throughout this document. This section was meant to provide a quick review for readers with a basic knowledge of corrosion. Full glossary of terms used throughout this document can be find at NACE International website (NACE Corrosion Glossary, 2012).

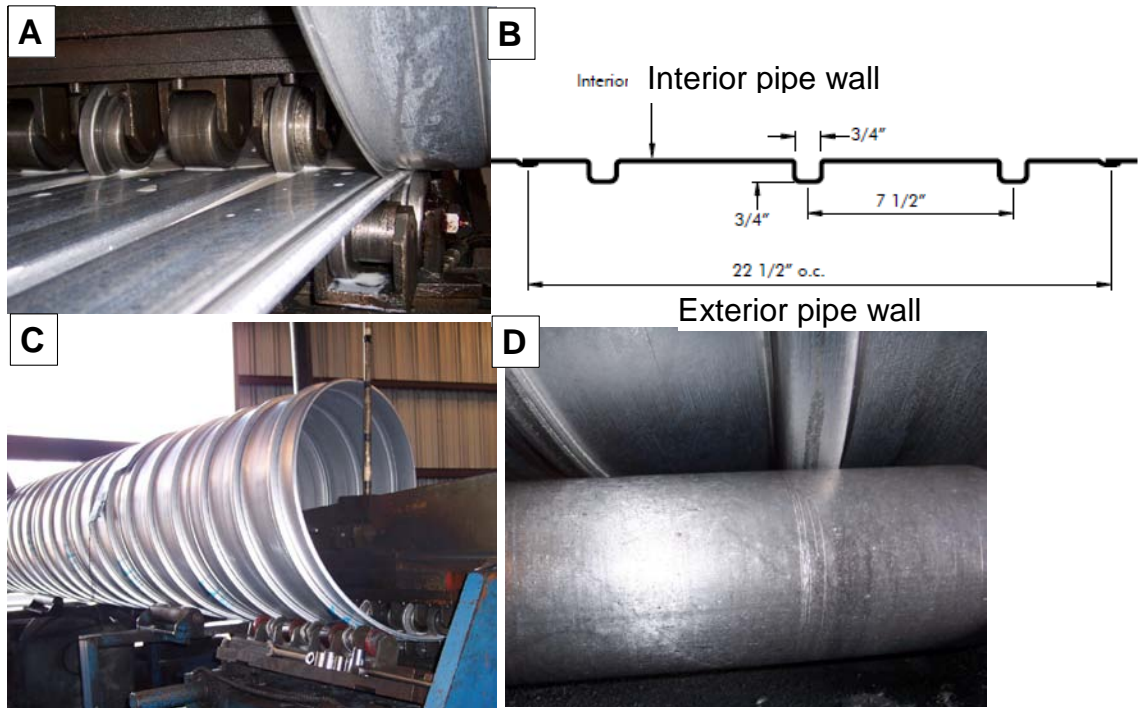


Figure 2: SRAP manufacturing process (A-C). Minor scratches during fabrication of SRAP (D). [Photographs by the Author].

1.2 Relevant Corrosion Principles

1.2.1 Definitions

Corrosion is an electrochemical process which can lead to the deterioration of metals, due to reactions with their environments (Roberge, 2006).

The cost of all forms of corrosion in the United States is approximately 3% of the

national gross domestic product with similar estimates in other developed countries (Materials Performance, 2002). The energy needed to extract metals from their ores is released during the process of corrosion, returning the metals back to their natural form. Corrosion processes require four simultaneous components: electrolyte, electronic path, cathodic reaction, and anodic reaction. No corrosion would take place in the absence of any of the above components. In almost all metallic corrosion process, the ionic charge is transferred in aqueous solutions. A simplified scheme of the corrosion process of a metal (e.g. aluminum) in water is illustrated in Figure 3.

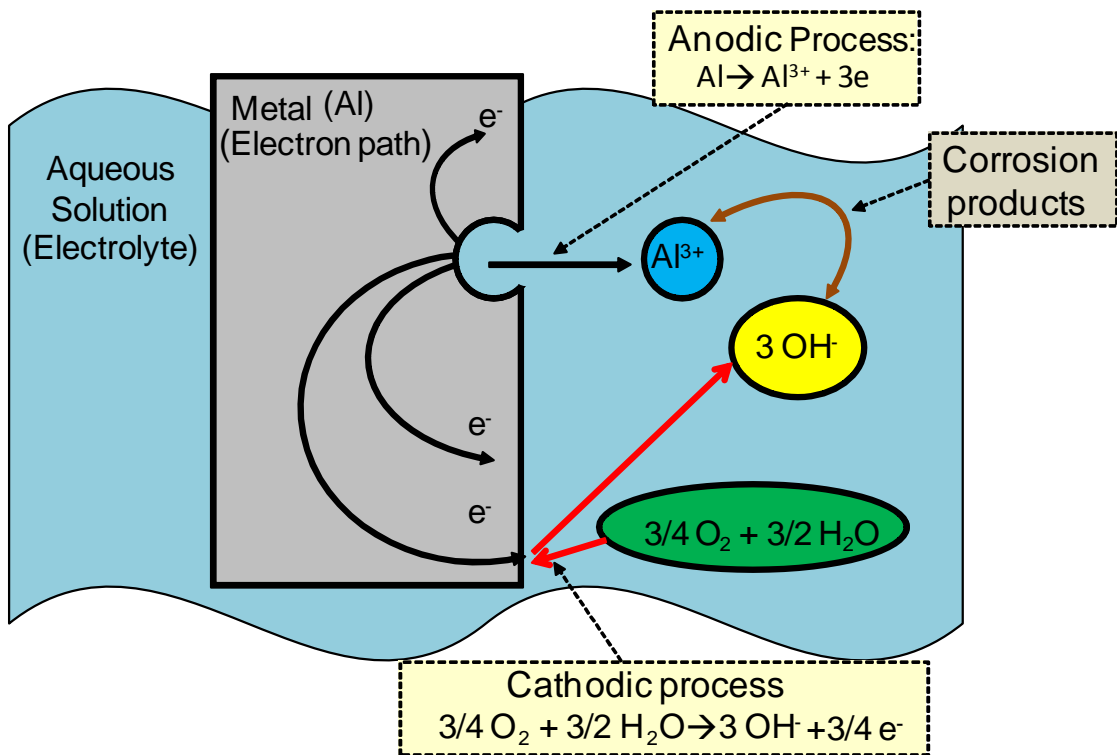
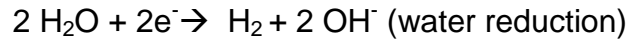
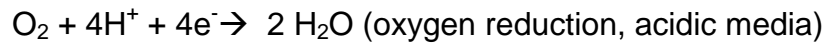
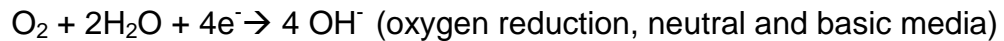


Figure 3: Simple schematic of corrosion process in water.

In the anodic reaction (oxidation reaction), $\text{Al} \rightarrow \text{Al}^{3+} + 3\text{e}^-$, aluminum atoms are released as aluminum ions in the solution which leaves electrons behind that will be consumed by the cathodic reaction. The rate of the anodic reaction (oxidation reaction) is equal to the cathodic reaction (reduction reaction) during any metallic corrosion process unless an external current is applied (e.g. for cathodic protection purposes). Common cathodic reactions include:



1.2.2 Polarization Behavior of Electrochemical Systems

The current generated by the anodic reaction, as a result of charge transfer, can be converted to an equivalent mass loss or corrosion penetration rate using a relation discovered by the nineteenth century scientist, Michael Faraday (Roberge, 2006). Faraday's Equation :

$$I = n F W / (M. t) \quad \text{Eq (1)}$$

where:

W = mass lost or gained (g)

n = valence of the metal

F = Faraday's constant (96,500 coulomb/mole of electrons)

M = atomic mass of the metal (g/mol)

t = time (s)

The potential difference developed between a corroding metal and solution, as the net result of the charge transfer processes, can be measured using a voltmeter and a reference electrode. The potential at a steady-state condition and in absence of external current flow is referred to as the Open Circuit Potential (E_{OC}) or corrosion potential (E_{Corr}) (Jones, 1996). E_{OC} can be either an equilibrium potential in the case of a simple redox system, or a mixed potential in a corroding system due primarily to the interaction of a metal oxidation reaction and a separate reduction reaction. Deviation of the system's potential from E_{OC} to another potential (E), by means of external current, is here referred to as polarization and shown by $\eta = E - E_{OC}$. The polarization is anodic when $\eta > 0$ and cathodic when $\eta < 0$. A simple polarization diagram for a corroding system is illustrated in Figure 4. Polarization that involves limitation by surface reaction kinetics is referred to as activation polarization, and the polarization process that is controlled by diffusion of reacting species is called concentration polarization.

Anodic and cathodic currents are commonly expressed per unit area of electrode surface (e.g. $\mu A/cm^2$) as current densities (i_a and i_c respectively). In a corroding system with a mixed potential far removed from the equilibrium potential of either individual reactant, the value of i_a and i_c at E_{Corr} are equal to each other and to a value called the corrosion current density, i_{Corr} .

An electrochemical process is controlled by a combination of surface kinetics and mass-transport of the reacting species. The regions controlled predominantly by surface kinetics are characterized by current densities that are exponential functions of potentials. Slopes of the anodic and cathodic reaction rate curves in an E-logi polarization diagram for simple activation polarized conditions are referred to as Tafel slopes (β_a and β_c respectively).

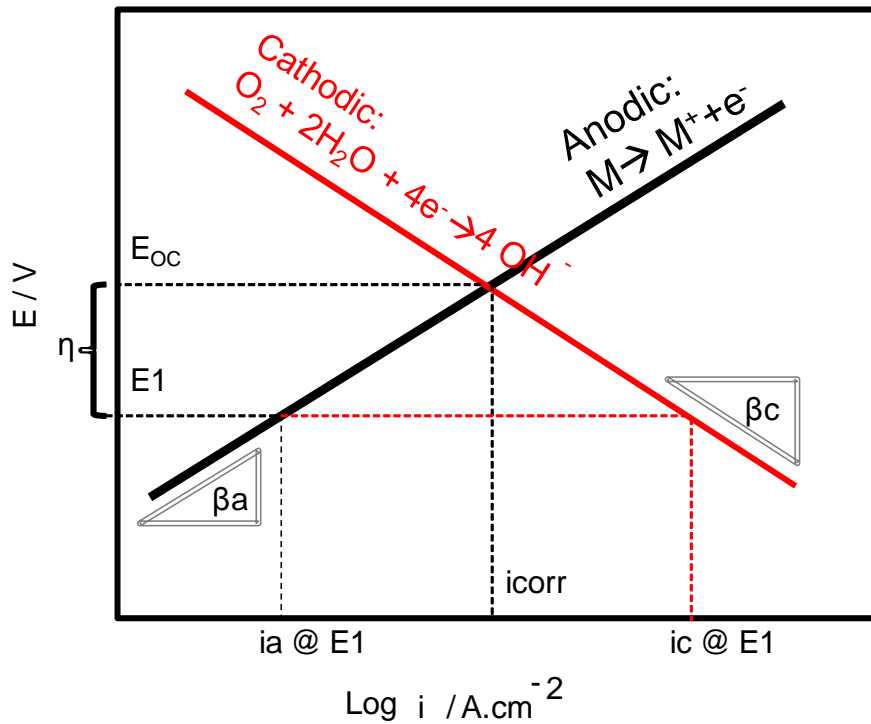


Figure 4: Simple polarization diagram showing anodic polarization functions and corrosion potential.

Under simple activation polarization conditions, when a source of external current is applied to polarize away from E_{Corr} , the anodic (i_a) and cathodic current (i_c) are (Orazem, 2008):

$$i_a = i_{corr} \cdot \exp \left[\frac{\eta}{\beta_a'} \right] \quad \text{Eq (2)}$$

$$i_c = i_{\text{corr}} \cdot \exp [-\eta/\beta_c'] \quad \text{Eq (3)}$$

where:

β_a' and β_c' are related to the Tafel slopes ($\beta_a = 2.303 \beta_a'$ and $\beta_c = 2.303 \beta_c'$) respectively.

The total net current at any potential can be calculated:

$$i = i_a - i_c \quad \text{Eq (4)}$$

If the rate of the electrochemical reaction is also limited by the finite rate of transport of reacting species to the surface of the electrode, additional terms are needed to relate the reaction rates to polarization. The cathodic process is prone to this type of limitation. The corresponding current density is a function of concentration gradient of the reacting species, and can be obtained by Eq (5):

$$i = nFD \cdot dC/ds \quad \text{Eq (5)}$$

where:

D is the diffusion coefficient of the species involved in the cathodic reaction (e.g. O_2). dC/ds is the concentration gradient for the reacting species close to the cathode surface.

1.2.3 Electrochemical Measurement Methods

The corrosion rates can be measured by non-destructive methods such as potentiodynamic polarization and electrochemical impedance spectroscopy (EIS). In potentiodynamic polarization tests, the potential of the electrode is varied over a voltage domain at some selected rate, using a computerized

instrument, and the amount of current needed to make such potential change is recorded. The polarization resistance of a corroding system, R_p , is defined as the ratio of that change in potential to the amount of required current, at the limit of very small changes and very slow variations.

The corrosion current (i_{corr}) can be found by:

$$i_{corr} = B / R_p \quad \text{Eq (6)}$$

where B is a function of β_a and β_c (slopes in polarization diagram as shown in Figure 4. In many systems, a practical estimate of the corrosion rate from R_p measurements can be made by using the value $B \sim 0.026$ V (for metal in active conditions), or $B \sim 0.052$ V (for metal in passive condition) (Jones, 1996, p.84).

EIS is one of the most commonly used methods proven to be fairly accurate in determining the corrosion rates. In this method, the polarization resistance of a metal is measured by a series of ac tests at predetermined frequencies. ASTM G 106 includes an appendix explaining the details of this method.

The EIS measurements require a 3-electrode cell configuration that consists of a working electrode (Metal), a reference electrode, and a counter electrode. The counter electrode is placed so that the excitation current is distributed uniformly to the working electrode. Analog equivalent electrical circuit models are used to interpret the EIS result. In such electrical circuit models, a resistive element, R_s represents the resistance of solution; the solution interface with metal includes a Faradaic element (in the simplest cases a Polarization

Resistance R_p , as well as an interfacial charge storage term approximating the double layer capacitance C_{dl} . The impedance of the double layer capacitor is given by:

$$Z_{Cdl} = 1 / C j \omega \quad \text{Eq (7)}$$

This charge storage at the metal-electrolyte interface, sometimes deviates from ideal capacitive behavior; the element representing such non-ideal behavior is called a Constant Phase Angle Element (CPE).

The impedance of non-ideal capacitance is shown as Z_{CPE} and given by:

$$Z_{CPE} = 1 / Y_o (j \omega)^n \quad \text{Eq (8)}$$

where n is a real number between 0 and 1, and Y_o is a constant.

When $n=1 \rightarrow Y_o = C$.

1.2.4 Passivity

A stable oxide film (passive film) formed naturally on the surface of metals such as chromium, nickel, and aluminum provides a barrier that greatly decreases the rate of the anodic reaction in these metals. Figure 5 shows the general polarization diagram for passive metals (Roberge, 2006, p.74).

In the case of aluminum, the oxide film Al_2O_3 is typically a few nm thick and consists of a porous and a compact layer. If damaged, for example, by scratching the surface, it would immediately re-form in many environments. Figure 6 shows the schematic of an oxide layer formed on the aluminum surface

in the atmosphere (Davis, 2000, p.26). The thickness of the compact barrier layer is temperature dependent.

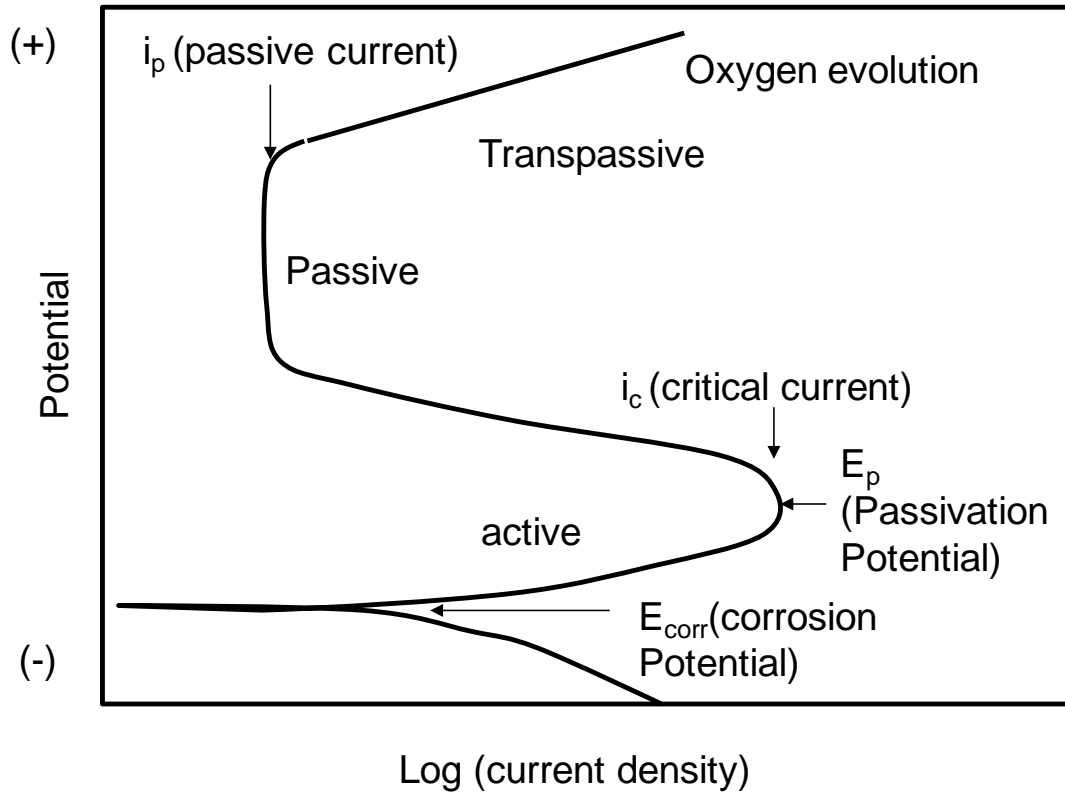


Figure 5: Polarization diagram of passive metals

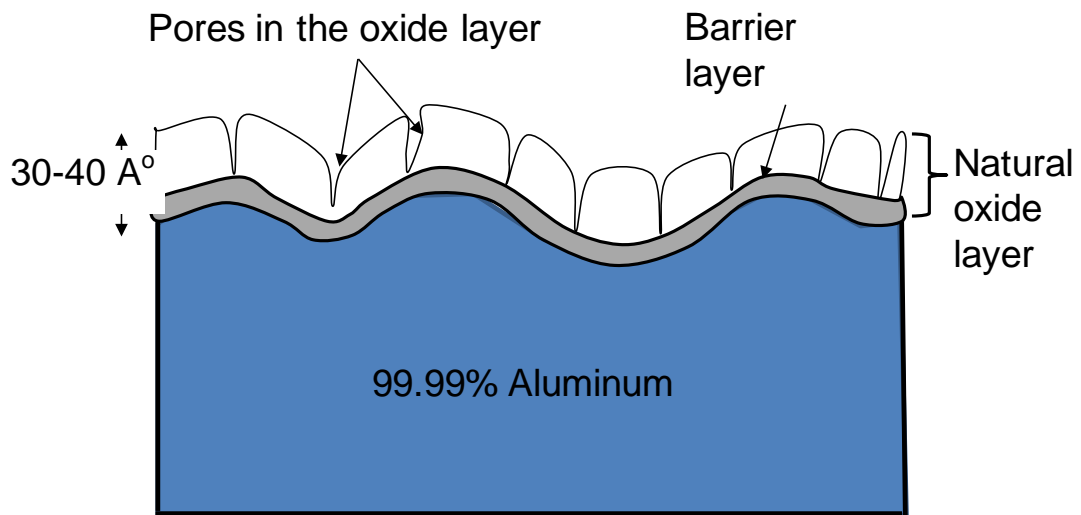


Figure 6: Schematic of the passive film on aluminum

To evaluate the stability of the oxide film in a given environment, thermodynamic models, such as Pourbaix (E-pH) diagrams, are created. The following Pourbaix diagram (Figure 7) illustrates the passive and active regions of aluminum at 25°C.

According to Figure 7, aluminum is passive (not corroding) in the pH range of about 4 to 8.5 (precise values depend on the concentration of the ionic species in the solution). Beyond this range aluminum corrodes and dissolves as Al^{3+} in acid and AlO_2^- , aluminate, in a basic environment (Davis, 2000). Pourbaix diagrams, however, do not consider the presence of aggressive ions, such as chloride, which attack and break the passive film and cause pitting corrosion.

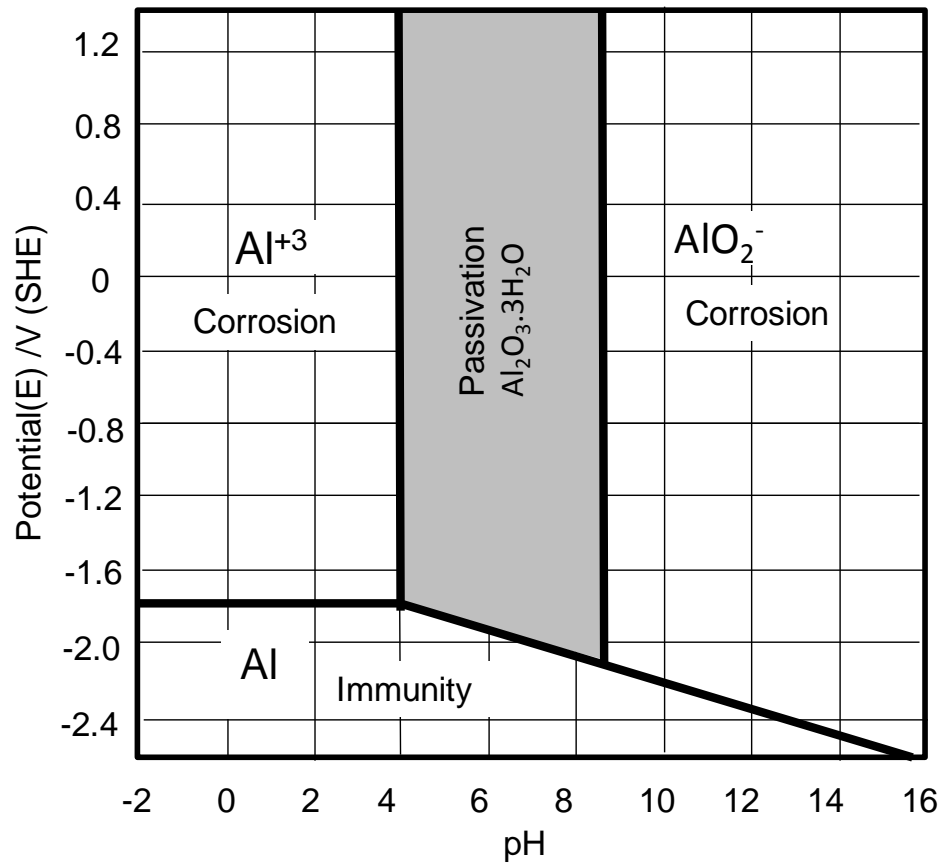


Figure 7: Pourbaix diagram for aluminum at 25°C

1.2.5 Pitting Corrosion

The ions aggressive to the passive film cause pitting corrosion. Pitting corrosion is localized and is manifested by random formation of pits (Davis, 2000). Pitting usually occurs in the presence of chloride and sulfate ions (Davis, 2000). Figure 8 shows a pit in NaCl solution (Lucas and Clarke, 1993, p.31). The pit serves as a local anode surrounded by cathodic regions. Although insoluble corrosion products may begin to build up inside the pit, creating a barrier for oxygen diffusion, the rest of metal surface would provide the site for the oxygen cathodic reaction.

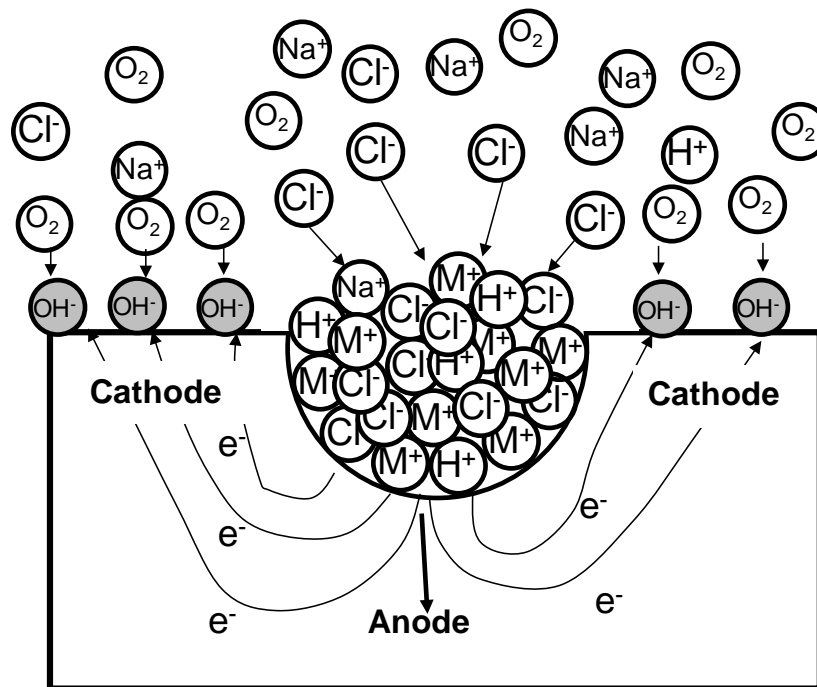


Figure 8: Pitting corrosion process in NaCl solution

It is suggested (Caseres, 2007) that the iron-rich precipitates (Figure 1) found in aluminum coating are the main cause of pitting corrosion on an

aluminized steel surface. These precipitates are preferential sites for the cathodic reaction, accelerating the corrosion of the surrounding aluminum.

As aluminum corrodes, the local pH increases which further dissolves the aluminum matrix. The corrosion of the surrounding aluminum causes the precipitate to detach from the aluminum matrix leaving a cavity on the surface. This cavity increases in size as the dissolution of aluminum continues and local pH increases.

1.3 Corrosion Studies of Aluminum and Aluminized Steel

As mentioned in section 1.1, the aluminized coating consists of an intermetallic layer (aluminum-iron alloy) and an outer layer (nearly pure aluminum) with iron-rich precipitates (Caseres and Sagüés, 2005). This section provides a brief literature review on corrosion performance of pure aluminum and aluminum-iron alloys; a review of the available literature on corrosion performance of aluminized steel pipes follows.

1.3.1 Corrosion of Aluminum

An air-formed oxide film (Al_2O_3) is typically present on an aluminum surface and is about 30-40 Å thick (Figure 6). The outermost portion of this oxide film reacts with water vapor present in the atmosphere to form a hydroxylated region that swells and enlarges with time. Using simple weight techniques, it was shown that the thickness of the oxide film increased to 200 Å and 1700 Å after five years of exposure to 52% and 100 % humidity, respectively (McCafferty, 2009).

Godard also suggests that the initial corrosion product of a freshly exposed aluminum surface to water is aluminum hydroxide which eventually ages and forms hydrated oxide or a mixture of oxides (Godard, 1967). The growth and aging process of an Al_2O_3 film in water occurs in two stages (McCafferty, 2009): First a pseudoboehmite film (which is a poorly crystalline modification of boehmite, $\gamma\text{-Al}_2\text{O}_3\cdot\text{H}_2\text{O}$) is produced. As time progresses a layer of bayerite crystals ($\beta\text{-Al}_2\text{O}_3\cdot 3\text{H}_2\text{O}$) covers the pseudoboehmite film. Based on weight gain measurements, it was shown that the film continues growing for 12 days in 20°C distilled water until it reaches a limiting film thickness ($50,000\text{ \AA}$).

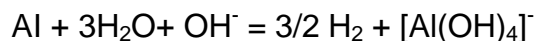
Roberge lists the possible reactions in an aluminum-water system as shown in Table 2 (Roberge, 2006, p.56). Reaction (2) in Table 2 shows the reaction between fresh aluminum and pure water that was discussed above. Such reactions produce a hydrated oxide layer on the surface of aluminum in the absence of aggressive ions.

Aluminum oxide film tends to be compact and adheres to the surface. Therefore, it appears to be an ideal protective scale in the pH range of about 5 to 8.5 pH, where this oxide is thermodynamically stable (Lucas and Clarke, 1993). Beyond this range the oxide layer dissolves as Al^{3+} in acid and AlO_2^- , aluminate, in a basic environment (Davis, 2000).

Aluminate ions, shown as $[\text{Al}(\text{OH})_4]^-$ or, equivalently as, AlO_2^- , are the main stable forms of aluminum in alkaline solutions. Aluminum dissolution rate depend on the concentration of hydroxyl and aluminate ions at the liquid/film interface

and the rate at which the ions are transported in the solution to and from the interface (Zhang et al., 2009).

Once the film is completely dissolved in an alkaline environment, and the aluminum is exposed (as in a fresh aluminum surface with no prior exposure), the electrochemical reaction below takes place (Zhang et al., 2009; Moon and Pyun, 1996). As shown this formula, the reaction is accompanied by hydrogen production which forms bubbles on the metal surface.



Aluminum hydroxide, generated on the surface of aluminum, may not be protective to aluminum and is also prone to chemical dissolution by further OH^- attack at the film/solution interface. The dissolution of the aluminum metal is much faster than the dissolution of the oxide film (Zhang et al., 2009).

Corrosion of aluminum in alkaline solutions is a major concern in nuclear water reactors during a loss of coolant accident or in metal-air batteries where aluminum is used as an anode. In such cases, the corrosion products result in precipitates which cause a system failure (Zhang et al., 2009).

In the study by Moon and Pyun (Moon and Pyun, 1996) the corrosion rate of pure aluminum (99.99% purity) was measured in acidic and alkaline environments, using electrochemical and weight loss methods at room temperature. The highest corrosion rate ($\sim 90 \mu\text{m}/\text{yr}$) was measured in an alkaline environment (0.5 M NaOH, pH = 13.22) and was about 25 times greater than the corrosion rate in an acidic environment (0.5 M H_2SO_4 , pH = 0.62).

Table 1: Possible reactions in the Al-H₂O system

Reactions Involving Aluminum Metal	
$Al = Al^{3+} + 3 e^{-}$	(1)
$2 Al + 4 H_2O = Al_2O_3 \cdot H_2O + 6 H^{+} + 6 e^{-}$	(2)
$Al + 2 H_2O = AlO_2^{-} + 4 H^{+} + 3 e^{-}$	(3)
$Al + 3 H_2O = Al(OH)_3 + 3 H^{+} + 3 e^{-}$	(4)
$Al + H_2O = Al(OH)^{2+} + H^{+} + 3 e^{-}$	(5)
$Al + 2 H_2O = Al(OH)_2^{+} + 2 H^{+} + 3 e^{-}$	(6)
Reactions Involving Solid Forms of Oxidized Aluminum	
$Al(OH)_3 + H^{+} = Al(OH)_2^{+} + H_2O$	(7)
$Al_2O_3 \cdot H_2O + 2 H^{+} = 2 Al(OH)_2^{+}$	(8)
$Al(OH)_3 + 2 H^{+} = Al(OH)^{2+} + 2 H_2O$	(9)
$Al_2O_3 \cdot H_2O + 4 H^{+} = 2 Al(OH)^{2+} + 2 H_2O$	(10)
$Al_2O_3 \cdot H_2O + 6 H^{+} = 2 Al^{3+} + 4 H_2O$	(11)
$Al(OH)_3 + 3 H^{+} = Al^{3+} + 3 H_2O$	(12)
$Al(OH)_3 = AlO_2^{-} + H^{+} + H_2O$	(13)
$Al_2O_3 \cdot H_2O = 2 AlO_2^{-} + 2 H^{+}$	(14)
Reactions Involving Only Soluble Forms of Oxidized Aluminum	
$AlO_2^{-} + 4 H^{+} = Al^{3+} + 2 H_2O$	(15)

1.3.2 Corrosion of Aluminum-Iron Alloys

Five possible compounds, including Fe₃Al, FeAl, FeAl₂, Fe₂Al₅, and FeAl₃, can be generated as the result of the interaction between pure aluminum and iron. The Fe-Al phase diagram shows these binary alloys and their constitutions (ASM Metals Handbook, 1973, p. 260). FeAl₂, Fe₂Al₅, and FeAl₃ are phases with greater aluminum compositions and are expected to be more brittle. Fe₃Al and

FeAl have a high iron composition and are expected to be less brittle (Kobayashi and Yakou, 2002).

Bouayad et al. (2003) studied the interaction between molten, pure aluminum and solid, pure iron by immersion tests. This study indicated that two main types of intermetallic structure generated are Fe_2Al_5 and FeAl_3 . However, Fe_2Al_5 with an orthorhombic structure tends to be the dominant phase. In this study, the tongue-like growth of the intermetallic layer into the steel substrate is explained as the result aluminum atoms' tendency to diffuse along the c-axis direction of the Fe_2Al_5 orthorhombic structure through structural vacancies.

A more detailed study of the growth of Fe-Al intermetallic layers was conducted by Kobayashi and Yakou (2002). In this study, the structure, morphology, and mechanical properties of Fe-Al intermetallic layers formed on the surface of steel with 0.45% carbon content after hot-dip aluminizing. An X-ray diffractometer (XRD) was used to determine the phase structure of the intermetallic layer. In this case, Fe_2Al_5 was also found to be the main intermetallic phase. The thickness of the intermetallic layer grew significantly larger with longer immersion times. Hardness tests illustrated greater hardness (HV1000) for Fe_2Al_5 compared to FeAl (HV600) and Fe_3Al (HV320) layers; however, Fe_2Al_5 had lower fracture resistance than FeAl or Fe_3Al .

Birbillis and Buchheit conducted a detailed study on corrosion performance of aluminum-iron alloys (Birbillis and Buchheit, 2005) and noted that these alloys are more noble than pure aluminum. The relative nobility of

aluminum-iron alloys and pure aluminum was examined by comparing their corrosion potentials and pitting potentials. More negative values of corrosion potentials indicate that the compound, when active, can undergo anodic dissolution at a higher rate. More positive pitting potentials indicate that the compound is more capable of maintaining its passive film. In this case, the corrosion potentials of -0.539 V and -0.823 V were measured for aluminum-iron alloys and pure aluminum, respectively. The pitting potentials were 0.106 V and -0.610 V for aluminum-iron alloys and pure aluminum, respectively (Birbillis and Buchheit, 2005); clearly, indicating that the aluminum-iron alloys are more corrosion resistant than pure aluminum.

The galvanic connection between the two compounds above may result in the corrosion of a less noble metal (aluminum). Indeed, in aluminized coating, where the coating consists of a pure aluminum matrix with aluminum-iron alloy particles, the difference in electrochemical behavior of the two compounds may result in localized corrosion of the hosting matrix (Caseres, 2007). In the study by Liao and Wei, (Liao and Wei, 1999), it was also noted that the galvanic coupling between constituent particles and the alloy matrix is responsible not only for the nucleation but also the growth of pits in aluminum matrix.

1.3.3 Corrosion Performance of Aluminized Steel

Aside from various manufacturers' reports on corrosion performance of aluminized steel type 2, very limited research studies are available regarding the

corrosion performance of aluminized pipes in service (Molinas and Mommandi, 2009). Many of these studies refer to an older study by Morris and Bednar.

Morris and Bednar investigated the performance of aluminized steel pipes and compared it to galvanized steel pipes at 54 test sites. According to the results of their investigation, aluminized steel was found to show significantly better performance compared galvanized steel in terms of corrosion and perforation (Morris and Bednar, 1998). Other recent studies on aluminized steel pipes also indicate similar findings.

In 1993, the Florida Department of Transportation (FDOT) performed a five year field study (Cerlanek and Powers, 1993) on the service life of three types of culvert pipes (aluminized steel, galvanized steel, aluminum clad and reinforced concrete). Pipes were installed in four different sites with different pH (ranging from 4.8 to 7.0) and resistivity (ranging from 77 Ω -cm to 40.2 k Ω -cm).

After two years of exposure, half of the specimens were extracted and analyzed. The rest were extracted at the end of five years. The report concluded that aluminized steel pipes lasted 2.9 times longer than galvanized steel pipes. Figure 9 shows the service life of four different drainage pipes at 2.5 k Ω -cm resistivity and varying pH. The result was similar to the study performed by the Federal Highway Administration which is detailed next.

In a study by the Federal Highway Administration (FHWA), completed in 1995 and published in 2000, the conditions of 32 culverts at 26 installations in 3 different states (Alabama, Oregon, and Maine) were evaluated. Out of these 32

culverts, 24 pipes were made of corrugated aluminized steel. The condition of the pipes was reported as the percent pipe perforation/pitting. The field data included: environmental parameters (such as pH and conductivity of the soil and waters), slope of the pipes, bedload, and flowing water velocity. The study estimated perforation of less than 14% for a majority of the pipes aging from 10 to 16 years, excluding the three cases below.

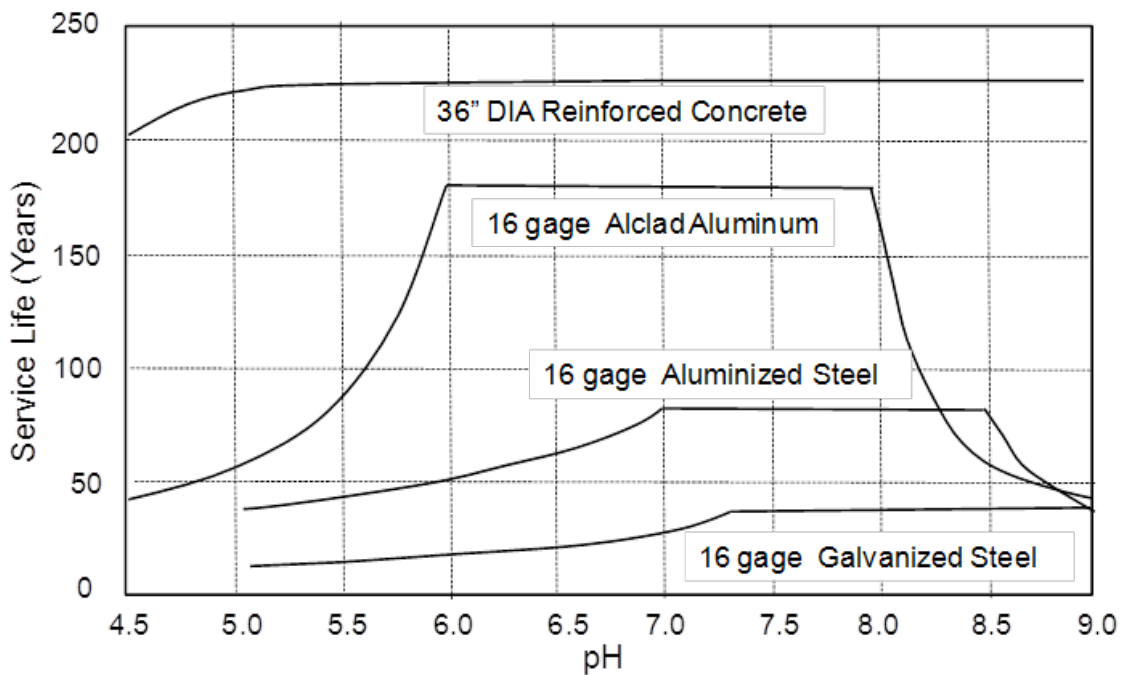


Figure 9: Estimated service life vs. pH at resistivity of 2.5 kΩ-cm.

The three worst cases of perforations (80-100%) occurred with heavy to moderate bed load, sharper installation slopes and relatively fast water flow (3-8 fps). The pH measured for these three sites ranged from 5.8 to 6.7 for the soil and ~7 for the water. However, the FHWA report (p.11) indicated that, in an earlier field inspection, significantly lower pH values were measured at the same sites. This was possibly due to the presence of aggressive effluents. The

discrepancy between the measured pH values was ascribed to gradual changes in the properties of the local soil over time (FHWA, 2000).

FHWA combined the data from this and other studies conducted on galvanized steel and concluded that, based on all of the data and observations, Aluminized Type 2 performed as well as galvanized pipe (including the three worst cases) or better than galvanized pipes (excluding the three worst cases). Also, it was noted that the pipe perforation had a strong correlation with bed load and soil chemical properties, a weak correlation with velocity of flowing water and no clear correlation with the pipe slope. Some uncertainties remain since the pipes were not tested in identical conditions (FHWA, 2000).

Additional studies, including the study previously conducted by University of South Florida, review the corrosion performance of undeformed aluminized steel sheets or wires, as opposed to aluminized pipes. In some other studies, the specimens were exposed to in highly aggressive solutions (In practice, however, the aluminized steel culvert pipes are intended to drain runoff waters with nearly neutral pH and moderate resistivity). These studies are explained next.

Steel Legault and Pearson (1978) conducted a five-year investigation on atmospheric corrosion of aluminized steel Type 2. In the investigation, aluminized steel test panels with uncoated cut edges (exposing the base steel) were exposed to industrial and marine environments. Small (~ 0.2 um/yr) and moderate (~ 0.45 um/yr) corrosion rates were observed in industrial and marine environments, respectively. The cut edges were free of corrosion in marine

environments and showed rust formation in industrial environments due to insufficient galvanic protection of the exposed steel (Legault and Pearson, 1978).

Similar specimens were tested by Townsend and Borzillo (1987) in severe marine, moderate marine, rural, and industrial environments for 13 years. The authors concluded that, in aggressive environments, the aluminized coating is anodic to the exposed steel when chloride ions impair the passivity of aluminum. However, in industrial and rural atmospheres, the aluminized coating became passive. So, little to no galvanic protection of the underlying steel was noted (Townsend and Borzillo, 1987).

Johnsson and Nordhag (1984) also performed a four-year investigation to compare the sacrificial corrosion performance of several metallic coatings on steel exposed to atmospheric environments and seawater. Weight loss measurements were taken to determine the corrosion rates of uncoated, cut edge aluminized steel specimens with, and without, scribe marks, which exposed the underlying steel. The corrosion of aluminized steel, even after one year, was mostly in the form of pitting, especially in a marine atmosphere. The investigation showed that, except in marine environments, the aluminized steel without scribe marks outperformed the galvanized steel. The scribed specimens demonstrated poor galvanic protection of the aluminized coating to the exposed steel in all environments, in the form of heavy red rust formation along the cut edges and at the scribe marks (Johnsson and Nordhag, 1984).

In the previous study at the University of South Florida, completed by Caseres (Caseres, 2007), undeformed aluminized steel specimens, with and without coating breaks, were immersed in solutions of fresh water of varying scaling tendencies and moderate chloride contents. Coating breaks were made by milling the aluminized steel sheet with bits from 2mm to 2 cm in diameter. The corrosion behavior of blemished specimens was compared with that of an unblemished aluminized steel surface. The main findings are summarized in the following:

- An extremely low corrosion rate was detected for aluminized steel stock, with no coating breaks, exposed to solutions with moderate Cl content, high alkalinity/high hardness with consequently high scaling tendency. In solutions with moderate Cl content and low alkalinity, early pitting of the outer aluminized layer, and strong surface discoloration, was observed. However, discoloration resulted from a momentary pH increase of the solution early on. In conditions where the pH remained near neutral, discoloration was delayed.
- In solutions with high scaling tendencies and moderate chloride contents, intense, early steel corrosion, at both small and large coating breaks, was observed. The solution was benign and did not promote passivity loss of aluminum. So, no cathodic protection of the exposed steel took place. However, in several instances, activation of the aluminum was delayed for long exposure times (e.g. 2,000 hrs) after which, cathodic protection of the

exposed steel took place. Little or no steel corrosion was observed in solutions aggressive enough to cause an early passivity breakdown of aluminum.

- No clear pattern was established between the corrosion rate and the size of the coating break.

The major objective of the above study was to predict the corrosion behavior of undeformed stock aluminized sheet as a function of the scaling tendency in simulated natural waters. It demonstrated that a high scaling tendency is beneficial. However, the effect of deformation as a possible promoting factor for corrosion of aluminized steel pipes was not considered. Also, the solutions chosen for testing represented limited regimes. Work with compositions more representative of actual Florida water conditions, under current FDOT design guidelines, remained to be done. These issues are the focus of this study.

2. INTRODUCTION

2.1 Recent Corrosion Failures

Confidence in the long term durability of SRAP has been challenged by recent, unexpected early corrosion failures of SRAP installed in various Florida locations. These failures, listed in Table 1, involved severe corrosion and motivated initial investigation (Sagüés, 2009) as well as the continuation research reported here. Failures were categorized into two modes as explained next.

Table 2: Field failures

Name	Location	Date Reported	Date Installed	Full Penetration	Mode
City of St. Cloud	Indiana Ave.	2005	~2003	Yes	A
City of Largo	West Bay/6th St	2005	~2003	Yes	A
Pasco County	SR-54 & US-19	2006	2001	No	A
Curlew Road, Clearwater	SR 586	2007	1997	Yes	A
Jacksonville	SR 212	2009	2006	Yes	B

In the first mode (Mode A), much of the corrosion occurred along formed ribs and often extended into the intervening smooth regions (Figure 10 A and Figure 11). This mode was first reported in 2005 for the drainage system owned

by the city of St. Cloud, FL. Severe corrosion was accompanied by roadway depressions. The affected pipes had been installed only 2 years earlier in 2003. A similar failure was reported, also in 2005, for drainage pipes owned by the city of Largo, FL (Figure 10). These pipes were also installed in 2003. At some locations, in both sites, the failure was clearly due to mechanical damage caused by either the manufacturing or installation of the pipes (Figure 10B).

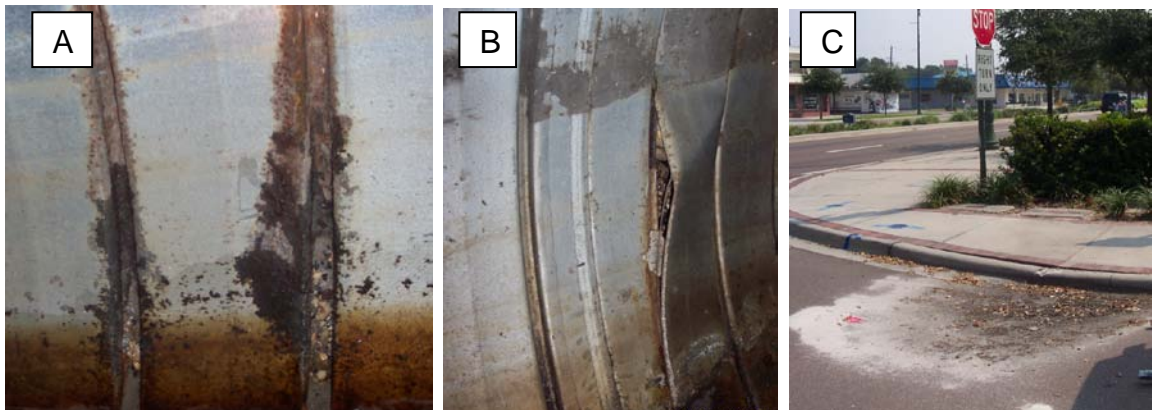


Figure 10: Premature failure of installed SRAP after 2 years of service at City of Largo, FL. (A: Corrosion initiation at ribs; B: Failure due to mechanical damage; C: Road depression due to the pipe failure). Photographs by Leonardo L. Caseres.

In 2006, pipe inspections at an FDOT project site at SR-54 & US-19 in Pasco County revealed severe corrosion (but not full penetration) of aluminized pipes installed five years earlier in 2001. Failures, comparable to those seen in St. Cloud, were reported in 2007 for a 10 years old installation at SR 586 (Curlew Road) in Clearwater, FL (Figure 11).

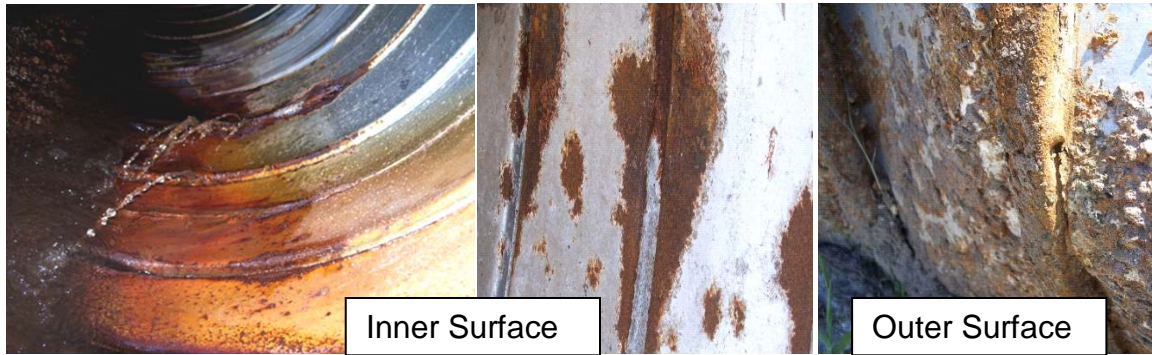


Figure 11: Premature failure of installed SRAP after 10 years in service (From Curlew installation at SR 586, Clearwater, FL)

The second mode (Mode B) of severe SRAP corrosion failure has been documented, so far, in one location (SR 212 in Jacksonville, Florida) and was revealed in 2009 by video inspection of the installed pipes. The pipes had been in service for only three years. The corrosion was in the form of multiple localized pipe wall penetrations, starting from the soil side, over a > 10 m long section of pipe that was placed on a limestone backfill. The penetrations started from the soil side and did not preferentially affect the ribs.

2.2 Understanding Corrosion Causes and Open Issues

Mode A corrosion was investigated extensively in the field by both the pipe manufacturer and FDOT, and by follow-up FDOT-sponsored laboratory studies (Sagüés, 2009). It was concluded that much of the corrosion originated from unusual fabrication damage and equipment problems such as stuck rollers. The fabrication damage caused helical cuts along some of the ribs with consequent corrosion loss in those regions. However, not all of the corrosion observed in the field could be explained as being related to severe distress from manufacturing

deficiencies. The large, localized plastic strain exerted during mechanical deformation, essential for forming the ribs in SRAP, was considered to have also played a role in promoting or aggravating corrosion.

Initial experiments conducted in an early investigation and discussed in section 6.1, showed that even moderate amounts of plastic strain cause cracking of the inner layer of the aluminized coating on the steel (Akhoondan et al., 2009). That layer, as explained in section 1.1 is made up of a brittle Al-Fe intermetallic alloy which cracks readily under tensile stresses such as those encountered during forming. The outer layer, which is more ductile, can stretch plastically to cover the gaps left by the inner layer cracks. However, if the deformation is large enough the outer layer fails too and leaves the underlying steel directly exposed to water and subject to corrosion.

The evidence from the previous laboratory tests and field observations suggests that regular production SRAP in mild service environments has some propensity for localized corrosion at the ribs because of the presence of occasional coating breaks inherent to the manufacturing process. If those are the only coating breaks and are small in size or numbers the mild galvanic protection from the surrounding aluminized steel may be sufficient to prevent the onset, or arrest the development, of corrosion of any exposed steel. However, that protection may not be enough under the conditions which are exemplified by, but are not limited to, the following:

1. Large coating breaks, e.g. due to manufacturing defects that introduced cuts, such as those observed in the field sites experiencing severe corrosion.
2. Small but numerous coating breaks, e.g. produced under still normal but borderline mechanical forming distress.
3. Insufficient galvanic coupling between the exposed steel and the unblemished aluminized surface, e.g. in cases where the environmental resistivity is high, and the galvanic macrocell extends only a short distance away from the exposed steel zones.
4. Excessive anodic polarizability of the unblemished aluminized surface, e.g. when the environment is not aggressive enough to induce appreciable localized passivity breakdown, or passive film dissolution, of the aluminum film, so galvanic action is negligible.

Under conditions such as these, the corrosion of steel exposed at the breaks may proceed unimpeded with possible penetration of the culvert wall by Mode A corrosion after a period of only a few years. The process could be aggravated by the development of rust crests at the corroding spots, which may provide sites for additional local cell cathodic reaction (likely O₂ reduction), with

an elevation of the mixed potential and a consequent increase in the steel corrosion rate. Further aggravation could result from the sacrificial consumption of the aluminum near the edge of the corroding steel, perhaps enhanced by the production of hydroxide ions from oxygen reduction, as indicated in (Sagüés, 2009). The aluminum consumption near the edge could in turn, expose additional steel resulting in propagation of a corrosion front starting from the initial blemish. Such mechanism could explain the observation of corrosion propagating away from the initial distressed ribs in the early corrosion field incidents (Sagüés, 2009). Elucidation of the factors noted above was necessary and was addressed by the investigation reported here.

Mode B corrosion was not uncovered until after the completion of the previous study, Project BD497. Because the deterioration took place with SRAP on limestone backfill, it was speculated that the corrosion was due to rapid wastage of the aluminized layer in a high pH medium caused by the interaction of groundwater with limestone. That hypothesis and its consequences on the selection of backfill materials for SRAP, as well as possible synergism between both modes of corrosion, are also examined in this investigation.

2.3 Objectives and Research Scope

The issues introduced in the previous section defined the objectives of the work reported here. They are stated as follows:

- Establish to what extent the Mode A corrosion incidents can be ascribed to manufacturing defects that can be rectified by appropriate quality control as opposed to an intrinsic vulnerability to corrosion of regularly produced SRAP due to ordinary forming strains.
- Determine the mechanism responsible for Mode B corrosion and the role that limestone backfill played in that deterioration.

To address those objectives, the following research tasks were conducted:

1. Assess field evidence by detailed analysis of Mode A and B failure site cases.
2. Assess mechanical distress in SRAP ribs in coupons from the Mode A corrosion field locations, regular production pipe, and intentionally formed aluminized steel. Identify possible correlations between mechanical distress and corrosion in the field.
3. Formulate test solutions for simulating natural waters in corrosion tests.

4. Determine the effect of mechanical distress on corrosion performance of aluminized steel in simulated natural waters. In this portion of the investigation, experiments addressed the comparative performance of flat and severely deformed aluminized steel stock; the comparative performance of SRAP and ordinary corrugated aluminized pipe samples (in both stagnant and moving waters), and the effect of simulated severe manufacturing distress (exposed cut edges).
5. Determine the mechanism of corrosion in water contacting limestone. This portion of the investigation involves comparative corrosion experiments in clean sand and in limestone and includes the effect of water flow in the latter.
6. Conduct a general discussion of the findings. The findings from the previous thrusts are discussed in the context of mechanisms responsible for SRAP deterioration.

3. EXAMINATION OF FIELD EVIDENCE

As noted in section 2.1, extensive corrosion of ribbed aluminized steel type 2 culvert pipe, installed along Curlew Road in Clearwater, Florida (Mode A), was discovered in late 2006, when the installation was about 10 years old. A subsequent investigation, and full report, was made for FDOT by Concorr Florida, Inc. (CONCORR Florida, 2007). The pipes showed widespread circumferential and horizontal cracks as well as extensive corrosion. The latter was often clearly associated with mechanical distress similar to those noted at the St. Cloud site (Sagüés, 2009). A metal coupon from the Curlew failure site was made available for further examination. The metal coupon exhibited heavy red-like corrosion products which accumulated, mainly at the spiral ribs and lock seams, from the Interior (water-side) and exterior (soil-side) (Figure 11). Eight specimens along the rib and seam regions were cut out, and carefully cleaned with ethanol to remove grease and loose pieces. They were then cast in epoxy and finely polished to 1 μm . Figure 12 illustrates the typical features observed at the metallographic cross section of a ribbed specimen. Breaks at the outer coating (as seen in Figure 12 left side, at two different magnifications) are typical of bent regions. It appears that corrosion regions (semicircular region in steel substrate) occurred directly underneath the breaks at bent areas. No breaks, and therefore no significant corrosion spots, were seen in the straight portion of the

rib cross section (Figure 12 right side at two different magnifications). These observations are similar to those noted for the St. Cloud site (Sagüés, 2009).

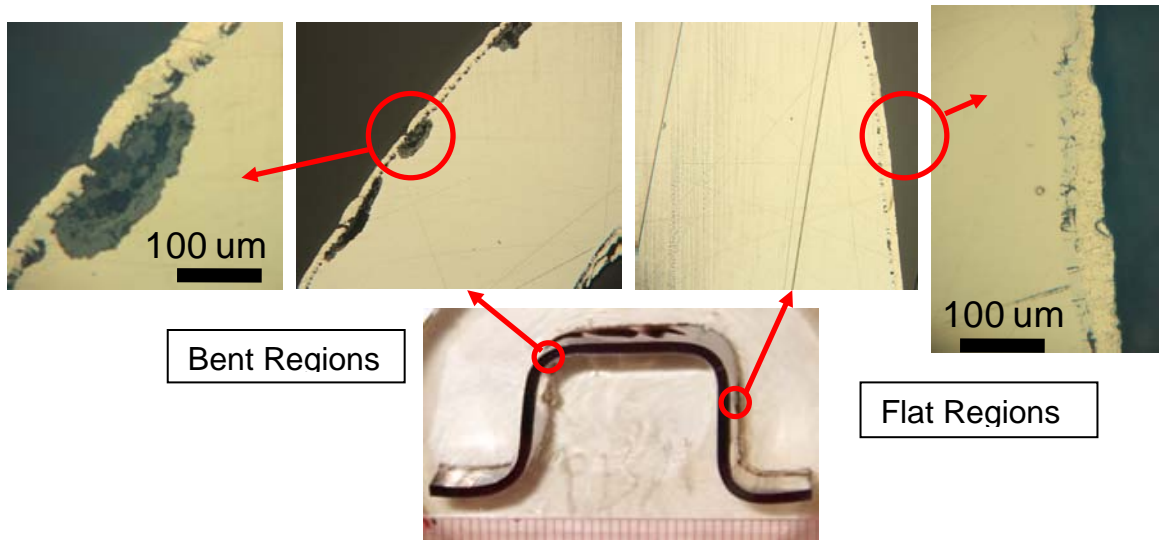


Figure 12: Metallographic cross section of bent region (Top-left) and flat region (Top-right) of a ribbed specimen (Bottom) cut out from metal coupon.

The Jacksonville SR212 failure (Mode B) was investigated by Rodney G. Powers & Associates for Contech Construction Products, Inc, and the results were reported to FDOT in November 2010. According to this report (CONCORR Florida, 2007) the pipe line was located ~8 to 12 ft below pavement. Water inside the pipe had a depth of approximately 10" and was pumped down to approximately 4" for testing. A significant ingress of water through holes in the pipe invert occurred due to the existing head pressure. Approximately 1 to 2 in of sand was observed in the invert. The presence of crushed limestone in the pipe surroundings was discovered. Four coupons were extracted from the site of which, one was made available to USF for further examination.

It appeared that severe localized corrosion took place starting from the soil side, on the smooth inter-rib regions of the culvert pipe, in contrast to the type of damage observed in the Mode A incidents. The corrosion took place on a > 10 m long section of the pipe and involved multiple perforations which were typically < 1.5 cm in diameter.

Metallographic examination, Scanning Electron Microscopy (SEM), and Energy Dispersive Spectroscopy (EDS) methods were utilized to better observe the coating damage/consumption and identify corrosion products present on the sample. The cross-section metallography (Figure 13) of the soil side revealed that, although the outer aluminum coating was almost deteriorated completely, the intermetallic layer seemed to stay nearly intact. Moderate coating loss was also observed on the water side.

While stray currents or microbiological activity cannot be completely ruled out as the possible causes of this incident, special attention was given to the chemical effect of backfill material due to the potentially high pH of the surrounding water and soil caused by the use of limestone. Figure 13 illustrates the location of the bore (top left), the extracted coupon (top right), and the metallographic cross-section of the coupon (bottom).

Another field trip on, March 3rd, 2011, was coordinated between USF and State Materials Office (SMO) for inspection of SRAP at a site that was near the Mode B failure just described and that may have had a similar soil environment. Due to hazardous conditions, entering the pipe was not possible. However,

several potential measurements were made with the help of a diver inside the pipe. The potential measurements were typically around -0.580 vs. SCE which agreed with previous measurements reported for the aluminized pipes in service (FHWA) and not indicative of unusual circumstances. Those potentials are also in the order of values measured experimentally as discussed later in section 7.1 and section 7.2.3.3 and not related to Mode B corrosion.

Additionally, water samples were collected and tested for conductivity and pH. Neutral pH values of 7-8 were observed for the water samples. Due to flooding, no soil samples suitable for identification of materials in the backfill could be collected.

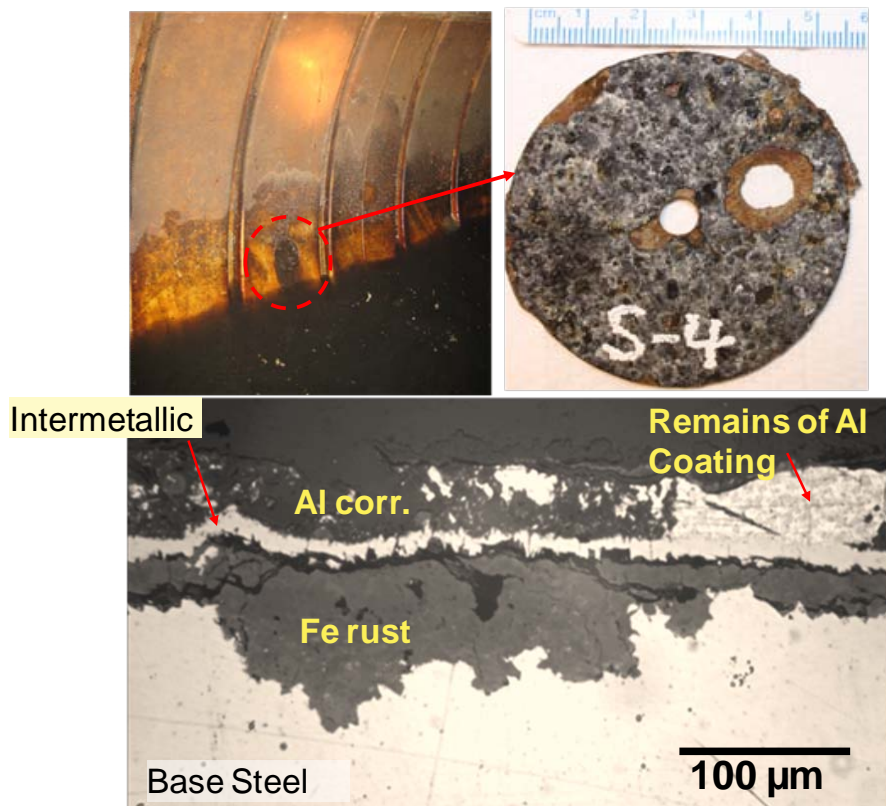


Figure 13: Location of the bore (Top-left), extracted coupon (Top-right), and metallographic cross section of the coupon (Bottom).

A pipe coupon obtained at a 10 o'clock orientation did not show signs of corrosion at either side either visually (Figure 14) or upon metallographic examination. Hence, despite the proximity to the other failure site, corrosion damage was not detected at this location. In summary, the insignificant corrosion in the extracted coupon and moderate potential values for this site where limestone most likely was used as the backfill (although that could not be verified since due to flooding the soil sample could not be collected) suggest that limestone in contact with water may be aggressive to aluminized steel only in certain conditions. As will be discussed in section 7.2, those conditions may involve flowing water and associated high pH, while in other conditions, for example in non-flowing water with resulting more moderate pH the contact with limestone by itself may not be sufficient to promote high corrosion rates.

Yet another field inspection of an SRAP site in the general proximity of the site of the Mode B failure described earlier took place on February 23th, 2012, near the Highland Glen and Beach Blvd intersection in Jacksonville, following reports of a pipe failure there. Significant mechanical deformation and ripped sections indicative of partial collapse were observed at the entrance of the pipe (Figure 15). Some corrosion products were observed around these stressed regions. Also, corrosion was observed in plain corrugated galvanized pipe segments that were used to join sections of SRAP (see Appendix 5 for photos).

However, excluding the mechanical damage, it appeared that the rest of the SRAP section inspected was generally in a good condition and was not significantly corroded. The water sample's pH and conductivity were about 6.3

and 2 kΩ-cm, respectively. The soil sample's (mud taken from underneath the extracted field coupon) pH and conductivity were about 7 and 7k Ω-cm, respectively. These values are within the range of accepted design environments for SRAP and did not appear to have been initiators of the observed deterioration. Some limestone rock was revealed beneath of core sample hole. Unfortunately the pipe specimen could not be retrieved due to adverse site conditions.

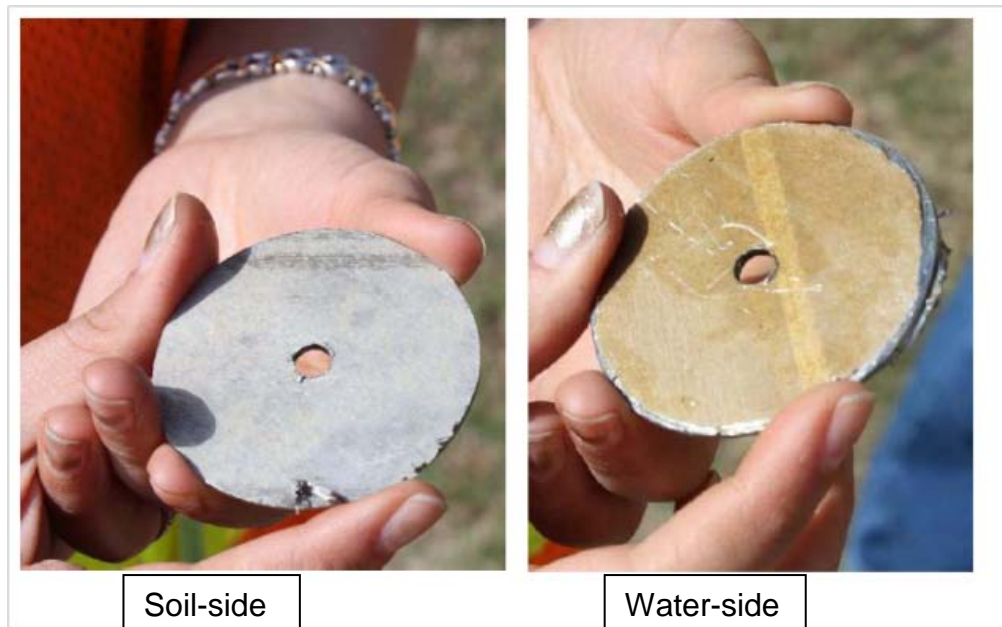


Figure 14: The pipe coupon from a site that was near SR 212 failure (at Wolf Creek/Beach Bly). Coupon did not show signs of corrosion on either side.

Based on the overall observations, this failure appears to have been of structural/mechanical origin, and the associated corrosion reflected only the widespread exposure of base steel at cuts and rips. Therefore, this failure too does not appear to be related to the presence of limestone and the same

comments as in the previous paragraph apply here. The failure does underscore the importance of manufacturing deficiencies and/or improper handling of pipes as a source of corrosion damage in the field. This issue is addressed in section 6.3 and detailed in further conclusions.



Figure 15: Photograph of in situ pipe located in Jacksonville, near Highland Glen and Beach Blvd. Mechanical damage (Top-left and bottom). Limestone rocks present beneath the bore location (Top-right).

4. MECHANICAL DISTRESS IN SRAP RIBS

As indicated in the introduction, it was important to compare mechanical strain in newly produced pipe to the strain present in coupons extracted from pipes affected by Mode A corrosion. In particular, it was important to determine if the radius of curvature at the rib bends in the older pipe was significantly smaller (indicating greater plastic strain) than that in newly produced pipe. If greater forming severity was observed, it could be interpreted as having been a contributing factor to the observed corrosion. The newly produced pipe was made following the discovery of the previous corrosion incidents and is assumed to reflect adherence to high quality manufacturing practice.

An initial assessment of this issue was conducted as part of the previous investigation (Sagüés, 2009), using a portion of an extracted pipe which failed prematurely by corrosion at the Curlew Road site (Table 2). The pipe portion contained corroded regions, but for these tests the ribs were sectioned at spots that had not shown significant corrosion. So, accurate dimensional measurements could be made. The outer (tension side) and inner (compression side) radii of curvature of the bends was measured in four different cross sections. Each cross section yielded eight radius measurements (Figure 16 shows a schematic with the circle fit for each) for a total of 32 values. A similar sampling took place for five cross sections from a newly produced pipe from the

("1st") manufacturer of the pipe used in the Curlew site produced under strict quality control. For this project, newly produced pipe from another ("2nd") manufacturer was similarly analyzed. The results of the three samplings are plotted in Figure 16 as cumulative distributions. The solid lines show cumulative normal distribution fit lines for the data in each case.

The results in Figure 16 show differences between the average radius of the various cases that are in the order of, or less than, the corresponding standard deviations. Moreover, the average radius for the Mode A corrosion case fell in between those of the samples from the two manufacturers. Overall, the results do not support the hypothesis that the Mode A corrosion was associated with earlier pipe production having experienced unusually severe fabrication forming, at least as measured by the value of the radius of curvature at the bends.

To further correlate the coating damage to the extent of metal forming, tensile tests were performed on specimens made of 16-gage flat aluminized steel sheet with a 0.5 inch wide and 4 inch long central section (Figure 17). Except for a short necked region which experienced ~50% strain, the rest of the central section experienced ~20% strain with minimal outer coating break. This strain value was comparable to the value calculated for SRAP at the ribbed regions using the change in metal sheet thickness at the formed region. However, breaks in outer aluminum coating at the ribbed regions were common. Figure 18, illustrates the surface cracks observed by SEM at the tension side of the bend as well as the typical metallographic cross-section of bend areas. Therefore, it was

speculated that the generation of breaks in the outer aluminum coating in SRAP is mostly due to bending as opposed to stretching the sheet metal by the rollers during the rib forming process.

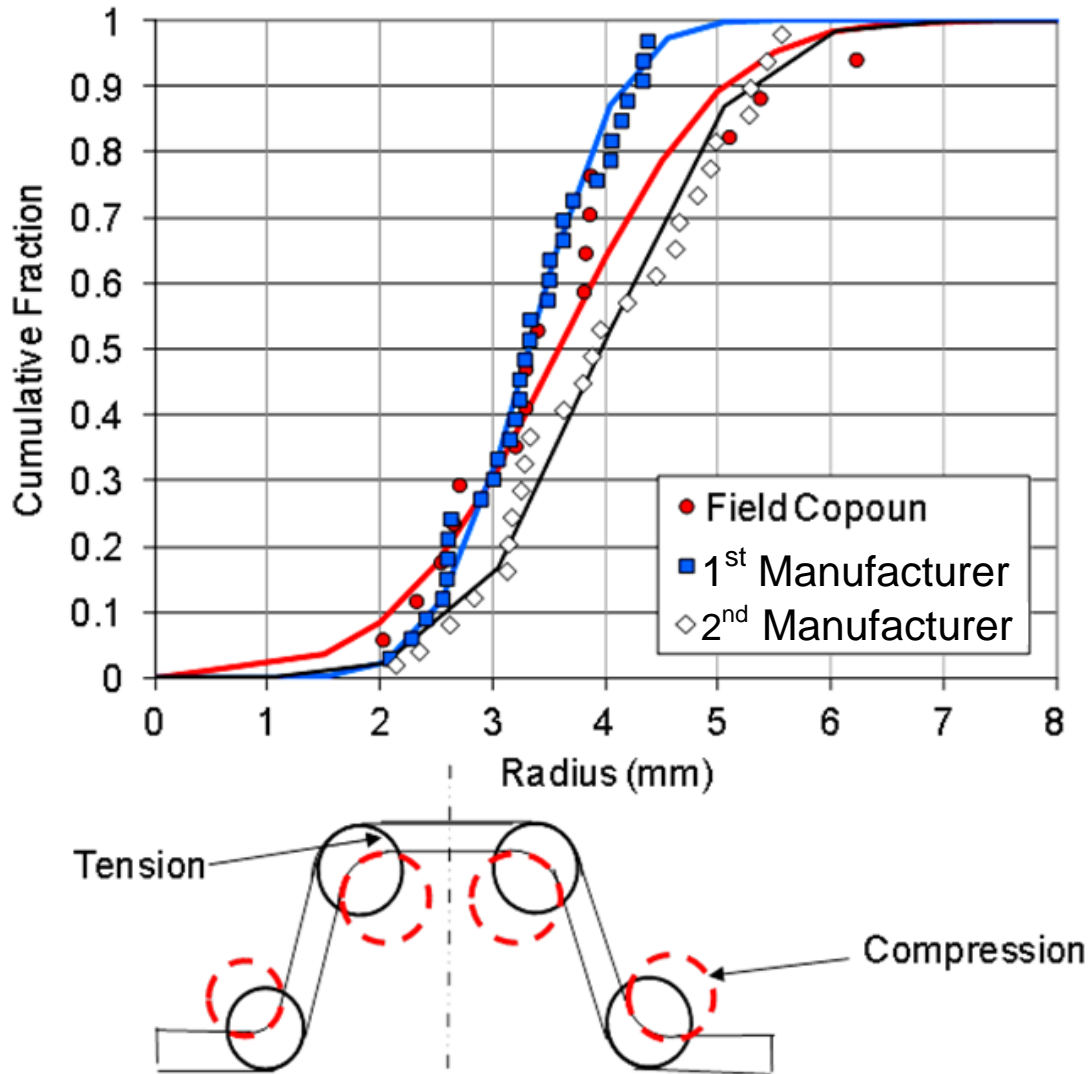


Figure 16: Comparison of cumulative distributions of rib radius of curvature (mm) between samples from newly produced aluminized steel type 2 pipes made by two different manufacturers and from a pipe in service for 10 years at the Curlew Rd. site. The schematic shows the position of the circles fit to each bend for each cross section.

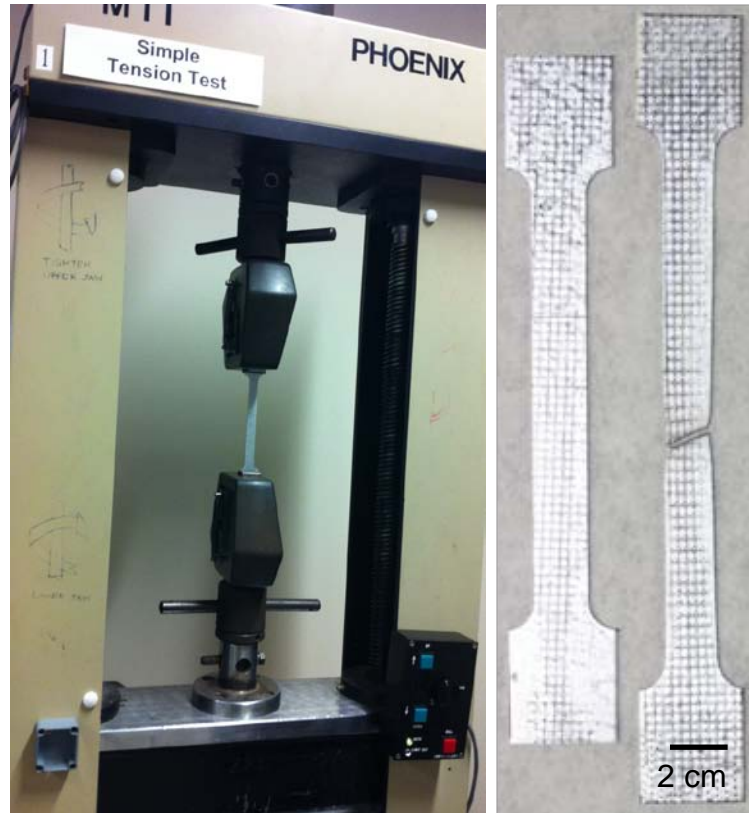


Figure 17: Specimens before and after tensile test.

Figure 19 shows the tensile specimens and their metallographic cross-section near the necking zone. While a significant amount of breaks occurred in the intermetallic layer, very few outer coating breaks were present. To see the direct occurrence of corrosion at regions with coating breaks produced this way, parts of the tensile specimens after the edges were covered with epoxy were immersed in solution S for period of two weeks. As shown in Figure 20, corrosion products (seen as a yellow shade) were present only within a small distance from the necking zone. The control specimen, with no plastic strain, showed no sign of corrosion after a similar length of exposure to the solution.

This preliminary experiment suggests that simple tensile deformation, while playing some role in creating coating damage the leads to corrosion, may be a secondary factor compared with the bending distress generated while creating ribs. The latter appears to be the main source of small but numerous coating breaks, observed in the aluminized coating in Figure 18, and a contributing issue in the development of Mode A failures. Further laboratory tests conducted to investigate the corrosion of formed aluminized steel are discussed in chapter 6.

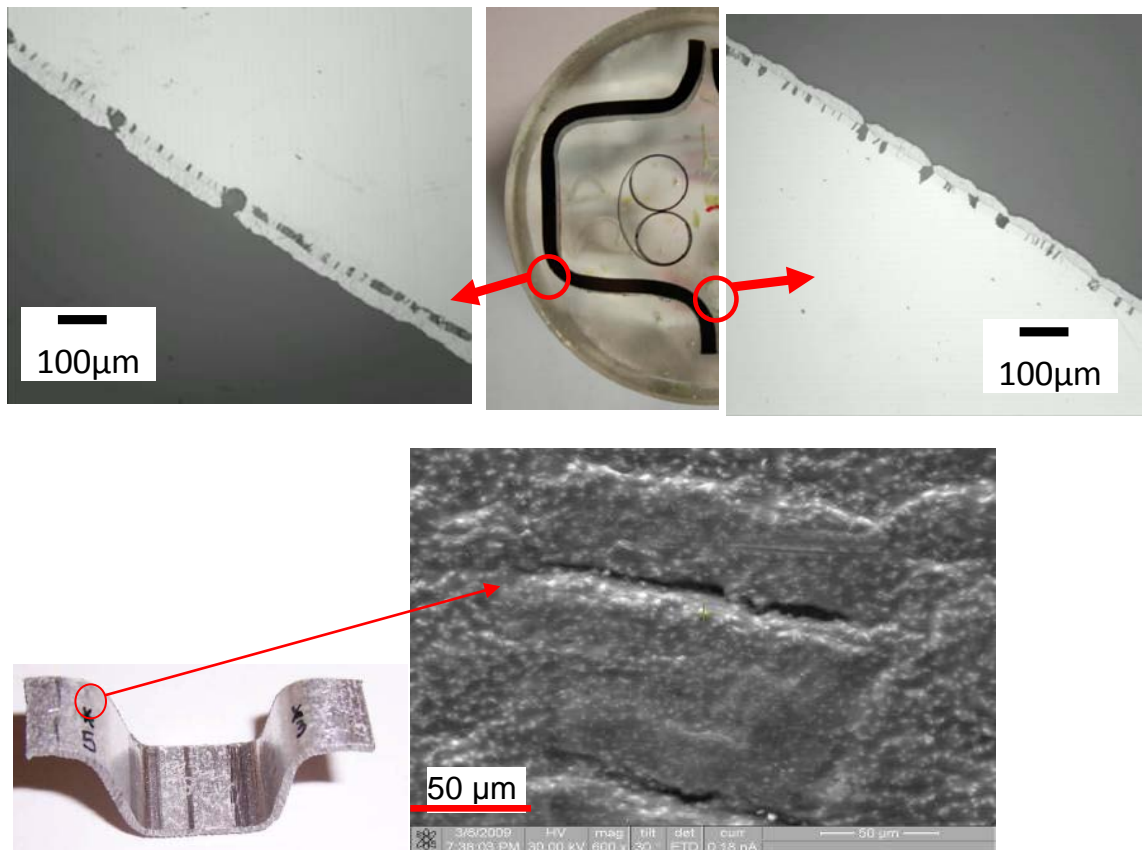


Figure 18: Metallographic cross-section of bend region (Top). SEM image of the bend at rib regions of newly produced SRAP (Bottom).

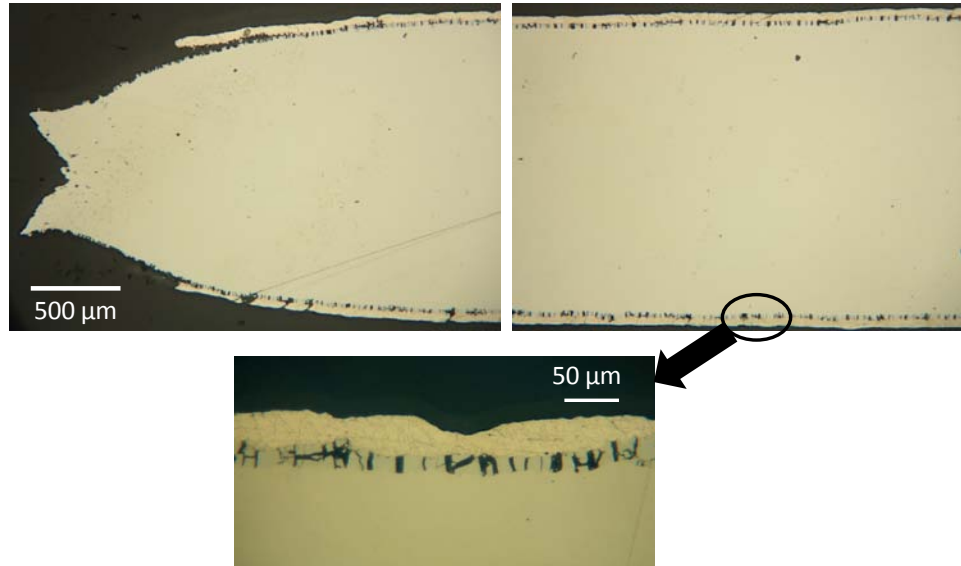


Figure 19: Metallographic cross-section of tensile test at the necking zone (Top-left). Also shown for ~2 cm away from the necking zone (Top-right).

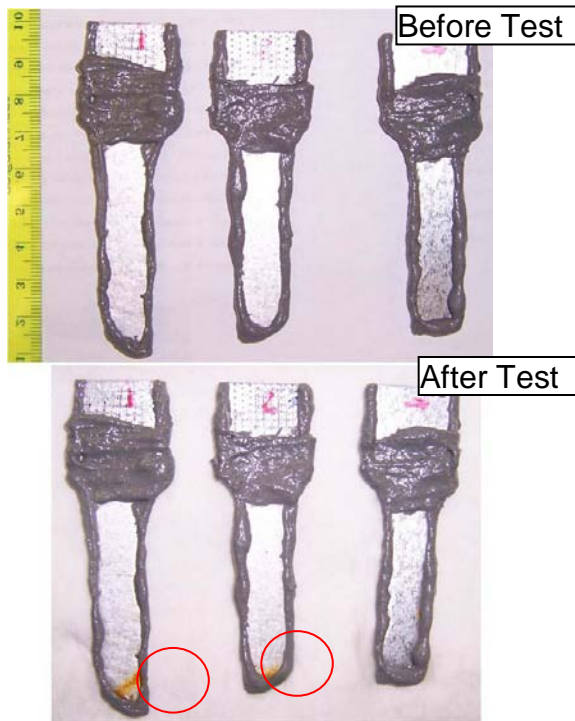


Figure 20: Tensile specimens before (Top) and after few days immersed in simulated natural waters (Bottom). Minor corrosion signs appeared at a short distance from the necking zone. The control specimen (far right) doesn't show signs of corrosion.

5. FORMULATION OF TEST SOLUTIONS

5.1 Specifications of Environmental Limits

Understanding the current FDOT selection and installation guidelines, as well as assessing the water and soil/backfill sample from field, is vital to replicate typical field conditions in the laboratory. Below is a brief summary of these general guidelines in addition to more specifications regarding the backfill material's properties.

FDOT recognizes four governing environmental parameters that have a direct effect on service life durability of pipes. These parameters include pH, resistivity, chloride ion concentration and sulfate ion concentration. Therefore, before selecting any type of pipe, environmental tests should be conducted to measure these elements. FDOT developed a computerized culvert service life estimator to help with material selection and determination of minimum wall thickness for a given design service lifetime (Cerlanek and Powers, 1993). For metal culvert piping, the time of first perforation (complete penetration) is considered to be the service life end point. An FDOT chart for estimated years to perforation of 16-gage aluminized steel Type 2 culvert pipes is reproduced in Figure 21.

Typically, once the pipe is selected and excavation conducted, the original soil excavated from the site is used as backfill material. However, if the pipe is below the water table and the dirt excavated is unworkable (e.g. extremely wet or has high organic content) then, according to FDOT specification 12-8.1.3, the engineer may decide to use backfill materials obtained from a different source. In this case, construction aggregates complying with ASTM C568-96 may be used for bedding and backfill of pipes to provide good structural support. As of the beginning of this investigation, limestone was allowable for that purpose.

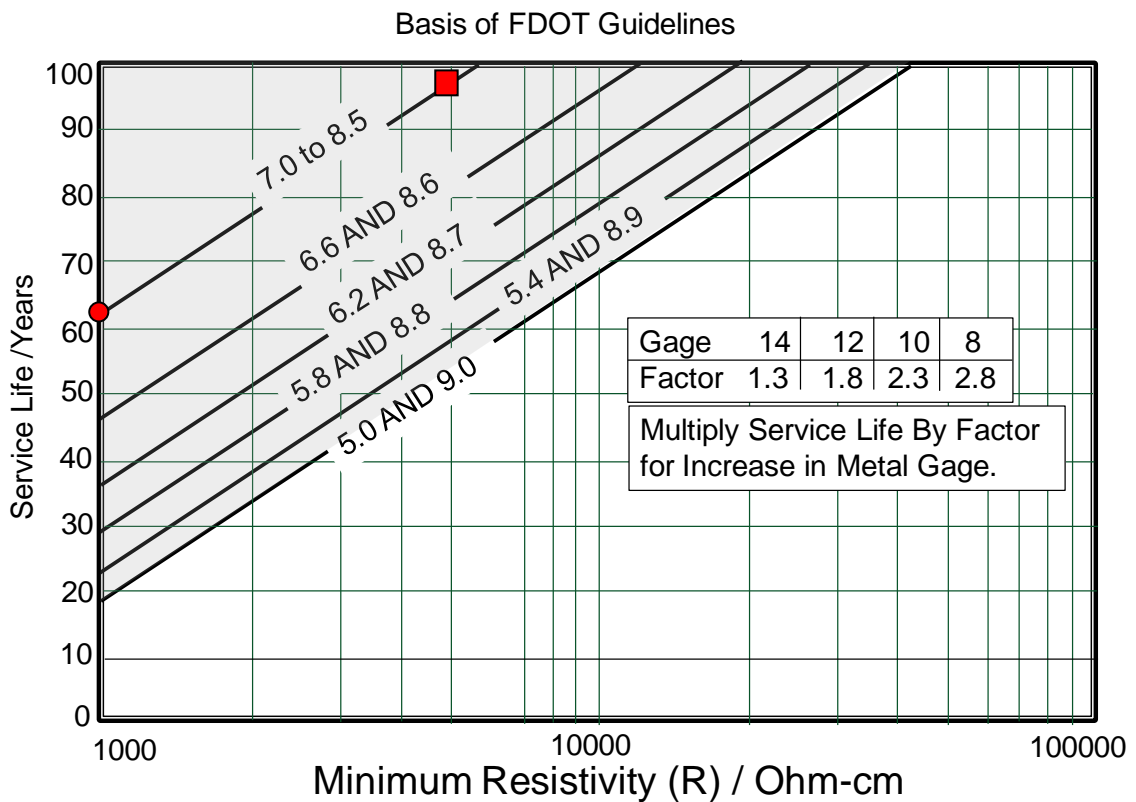


Figure 21: The FDOT chart for estimation of years to perforation of 16-gage aluminized steel Type 2 culvert pipes (solid lines). Light shaded triangle illustrates the service life functionality envelope. The circle and the square indicate the conditions for solution S+ and S respectively.

Pipe bedding and backfilling materials may have a significant effect on the corrosion performance of a pipe by changing the pH of the pipe's surroundings. The FDOT design drainage handbook (FDOT, 2008) states that the environmental tests should also be performed on structural backfill material or any subsurface materials along drainage alignment.

In fact, the issue of testing backfill material is also pointed out in the FDOT Soil and Foundation Handbook section 4.10. However, many times FDOT uses the general term "environment condition" to describe the properties of soil and water in immediate contact of the pipe; this may lead to misinterpretation of this term which describes only the properties of the original soil before pipe installation and not those of backfill imported from a different site.

Therefore, the possibility of applying aggressive backfill materials based on availability exists. Materials such as crushed concrete, typically used as backfill material for other constructions, is extremely aggressive to aluminum coating as they cause the elevation of pH to acceptable ranges

Other physical requirements for culvert pipe backfill are described in Florida Specification 125-8.3. In this case, the trenches for the pipes are split into 4 separate zones shown in Figure 22.

5.2 Replication of Field Conditions

To simulate field conditions within the range specified by FDOT, typical Florida water/soil properties were considered. In a previous study (Caseres, 2007), water and soil samples from several Florida locations were analyzed to

obtain the typical concentrations of chloride and sulfate ions present near currently installed aluminized pipes. Typical water hardness, alkalinity, and resistivity were also obtained. This data was evaluated and considered in generating a solution to replicate actual field conditions for this investigation. As a result, two simulated waters of S and S+, with the following properties, were chosen for laboratory testing.

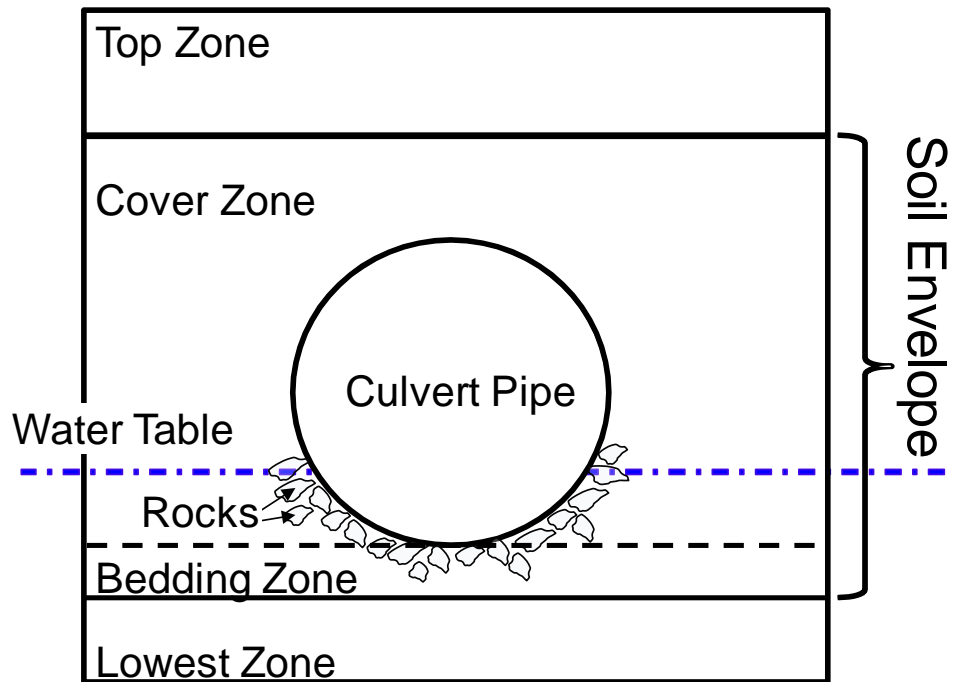


Figure 22: Typical pipe layout.

Solution S has pH ~ 7 and chloride and sulfate concentrations of 34 and 30 ppm, respectively. While it doesn't have a high precipitating tendency, this solution is considered as relatively benign due to small content of aggressive ions (chloride and sulfate) and high resistivity ~ 5000 Ω -cm. Under current FDOT

design guidelines for highway drainage culverts, a service life of ~100 years could be expected (Cerlanek and Powers, 1993) for this condition.

Solution S+ has similar pH and a similar sulfate concentration to solution S but a significantly larger amount of chloride (230ppm) with consequently lower resistivity (~ 1000 Ω -cm). This solution is therefore more aggressive. A service life of less than 65 years could be expected (Cerlanek and Powers, 1993).

Although the above solutions may well represent the typical soil/water conditions in Florida locations, they may not represent the properties of backfill materials commonly used in the installation of culvert pipes. In order to replicate typical backfill conditions, and based on the recent failures prescribed to the use of limestone backfill, a series of experiments fully discussed in chapter 7 were performed.

6. MODE A: EFFECT OF MECHANICAL DISTRESS ON CORROSION PERFORMANCE OF ALUMINIZED STEEL

This major focus of the research is the laboratory evaluation of corrosion performance of aluminized steel with various extents of coating breaks and mechanical distress exposed to relevant simulated natural waters.

6.1 Comparative Corrosion Evaluation of Severely Deformed and Flat Aluminized Steel

Preliminary experiments were conducted to determine if the deformation of already produced aluminized steel sheet would facilitate the corrosion process of this material. To test such hypothesis aluminized steel flat specimens were severely deformed and were exposed to solutions. Previous experiments, similar to the one explained next, were conducted with solutions not necessarily representing the field conditions, and initial findings were published (Akhoondan, 2007). These experiments were repeated with solution S; the summary of the experiment set-up and findings is as follows:

For these experiments, specially prepared specimens were made of octagonal portions of 1.52-mm (16-gage) aluminized steel sheet with minimal as-received surface distress. These specimens were indented at the center to produce a roughly hemispherical dimple shape using steel ball-bearings with diameters of 2.54 cm (1 in) , 1.90 cm (3/4 in), and 1.43 cm (9/16 in). The

indentation was made by pressing the bearing ball, socketed in a steel plate, into the initially flat specimen. Guide rods in the press assembly assisted in centering the indentation.

An indented Teflon plate was used to protect the convex face of the sample until nominally full hemispheric penetration was achieved. The convex face was the one later exposed to the test solution. After forming, the specimens were cleaned with ethanol and acetone and stored in a desiccator prior to immersion exposure to the test solution with a circular exposed area of 82 cm^2 (12.6 in^2) centered on the dimple (Figure 23).



Figure 23: Dimple specimens (Exposed Surface Area: 82 cm^2).

Metallographic cross section examination of a 1-in dimple illustrated frequent breaks in intermetallic layer and thinning of the nearly pure outer

aluminum coating at highly deformed zones. Intermetallic fissures at some regions extended to the outer aluminum coating, exposing the steel substrate (Figure 24).

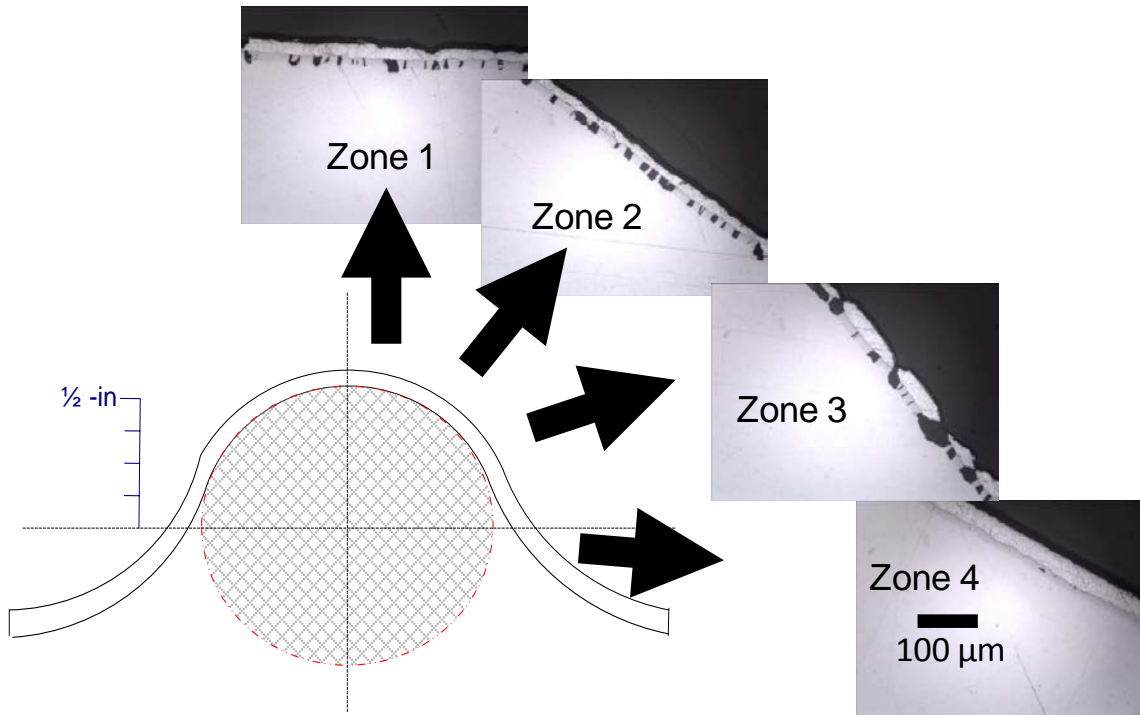


Figure 24: Coating damage due to deformation of aluminized steel type 2 (it was determined metallographically in the cross-section of a 2.54-cm (1-in) dimple).

The dimple configuration, with flat surroundings, permitted placement in the test cell with a flat gasketed joint that avoided leaking and minimized the risk of crevice corrosion at an unevenly sealed joint. Control flat specimens without surface indentations, with similar exposed surface areas, were used for comparison. Specimens were tested in duplicate.

A three-electrode test cell (Figure 25) was designed for exposing, horizontally, the convex side of the specimen, where distress is expected to be

worst because of the tensile stresses. A metal-metal oxide activated titanium mesh placed parallel to, and ~6 cm from, the specimen surface was used as a counter electrode. A low impedance activated titanium pseudo reference electrode 0.3 cm diameter and 5 cm long was placed ~1.5 cm above the specimens' indentation and periodically calibrated against a saturated calomel reference electrode (SCE). Each test cell was filled with 500 mL of a solution, which was not replenished during the test as explained below.

The test solutions in the test cells were quiescent and naturally aerated through a small opening. The relatively small electrolyte volume/total specimen area ratio was intended to be representative of worst-case culvert pipe conditions with stagnant water on the pipe invert, or of occluded conditions for pore water on the soil side of a pipe.

Immediately after exposure, corrosion was observed at high strain areas around the indentations (yellow shade). As time progressed the shaded region of corrosion product grew wider and became darker and various tuberculation occurred at the formed zones. SEM and EDS results confirmed that the corrosion product was iron oxide (Figure 26).

The results showed that aluminized steel that was strongly formed by spherical indentation was susceptible to early corrosion development. In contrast, undeformed aluminized surfaces showed much less deterioration during the same test interval.

It was concluded that solution S was not aggressive enough to induce strong manifestations of localized passivity breakdown or passive film dissolution of the aluminized coating at least in the short term. Consequently, the aluminized coating would not have provided substantial galvanic protection to the steel substrate under those conditions resulting in early corrosion of exposed steel in formed regions. These findings may explain in part why early Mode A corrosion was experienced at the field locations under nominally mild environmental conditions.

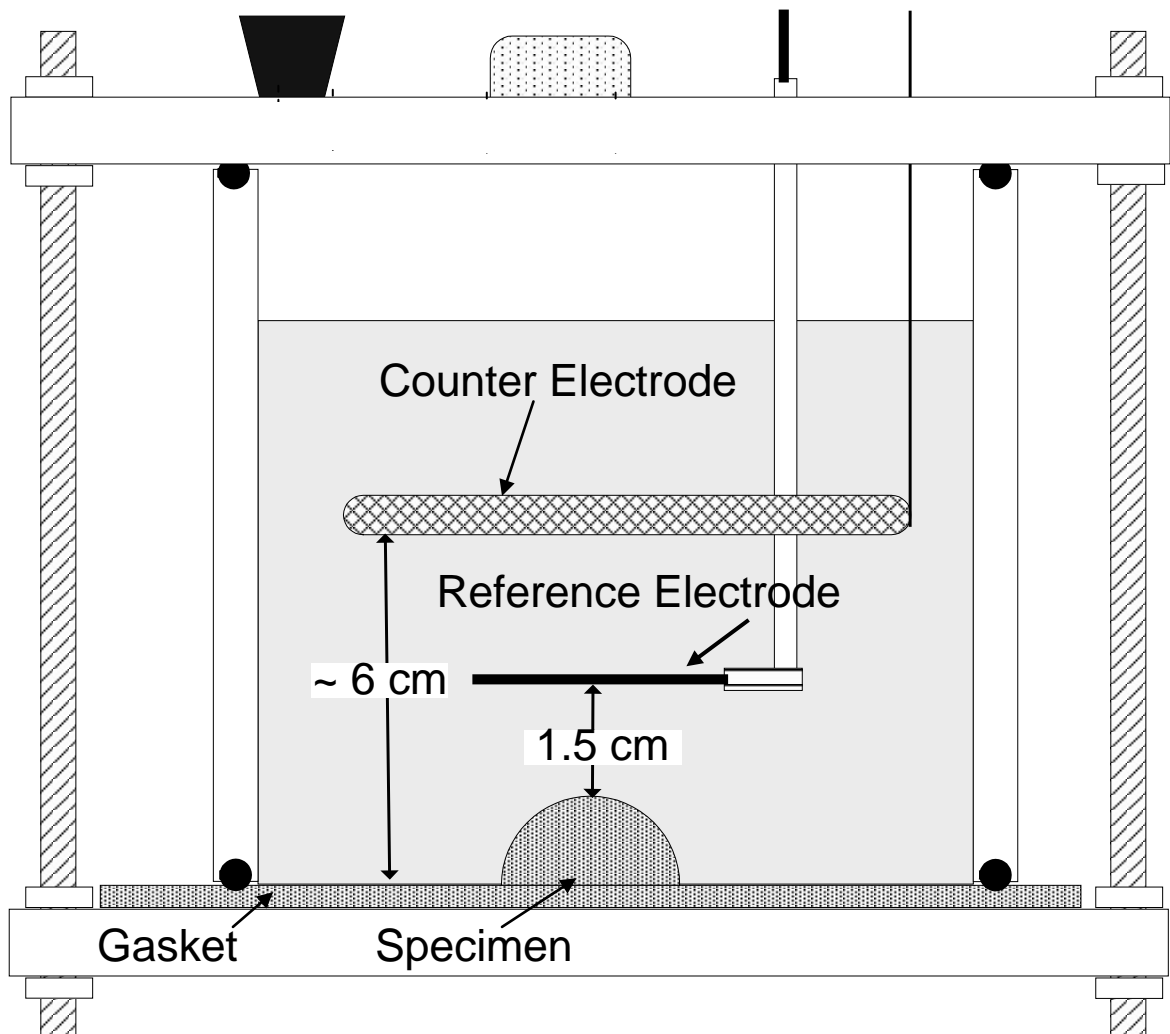


Figure 25: Three-electrode cell configuration for dimple specimens.

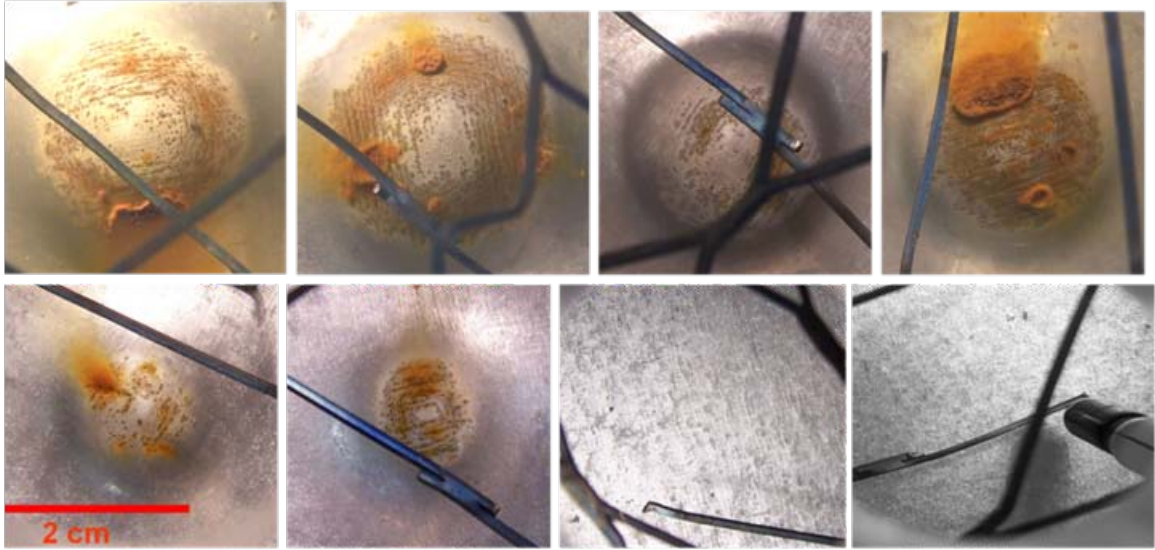


Figure 26: Visual comparison of corrosion development in formed and flat specimens immersed in solution S at 26 days of exposure. Top row: from left to right, duplicate specimens with 2.54 (1-in) and 1.90 cm (3/4 in) dimples respectively. Bottom row: duplicate specimens with 1.43 cm (9/16 in) dimple and flat condition respectively.

Next, the experiments were expanded to additionally examine:

- The comparative corrosion of regular production SRAP and less strongly deformed plain corrugated aluminized pipe (PCAP).
- The corrosion of aluminized steel with exposed cut edges replicating severe manufacturing distress.

Routine electrochemical measurements such as open circuit potential (E_{oc}), Electrochemical Impedance Spectroscopy (EIS), and cyclic cathodic and anodic potentiodynamic polarization were performed to assess the corrosion behavior of specimens during the time of testing. EIS tests typically were

performed using a Gamry™ Ref. 600 potentiostat in the frequency range from 100 kHz to 10 mHz using sinusoidal signals of 10 mV rms amplitude. To interpret the EIS data, a nominal polarization resistance R_{pn} , serving as a rough inverse indicator of corrosion rate, was obtained by subtracting the solution resistance from the real part of impedance at 10 mHz. This R_{pn} value was entered in Eq (6) (B value of 0.026V was assumed) to calculate the apparent corrosion current densities. All tests were performed at room temperature.

6.2 Comparative Corrosion Evaluation of Spiral Ribbed and Plain Corrugated Pipes

6.2.1 Preliminary Tests

Following the observations from the previous investigation, further exploratory tests were conducted in which small (e.g. 3x 3 in (7.6 x 7.6 cm)) samples of regular production SRAP, including the rib deformation, were cutout of a newly produced pipe. Control specimens (2 x 3 in (5 x 7.6 cm)) were also cutout from the smooth regions between the ribs. The cut edges were sealed with either beeswax or epoxy. Each specimen was placed in a three-electrode test cell similar to the one shown in Figure 27. Corrosion progression of small ribbed specimens (pipe water-side) in solution S is shown in Figure 28.

Figure 29 shows the average E_{OC} as function of time of each group of replicate specimens in this experiment. For graphic clarity, data spread bars are not included. An alternative indication of the variability of the results was obtained by calculating the standard deviation of the results of each group for each

reported test time. Those standard deviations were averaged for each group over the entire test period to serve as a group indicator of replicate test variability. An average variability indicator of all groups was calculated afterwards and is reported in the figure caption. A similar procedure was used to describe typical replicate variability in subsequent figures of this dissertation.

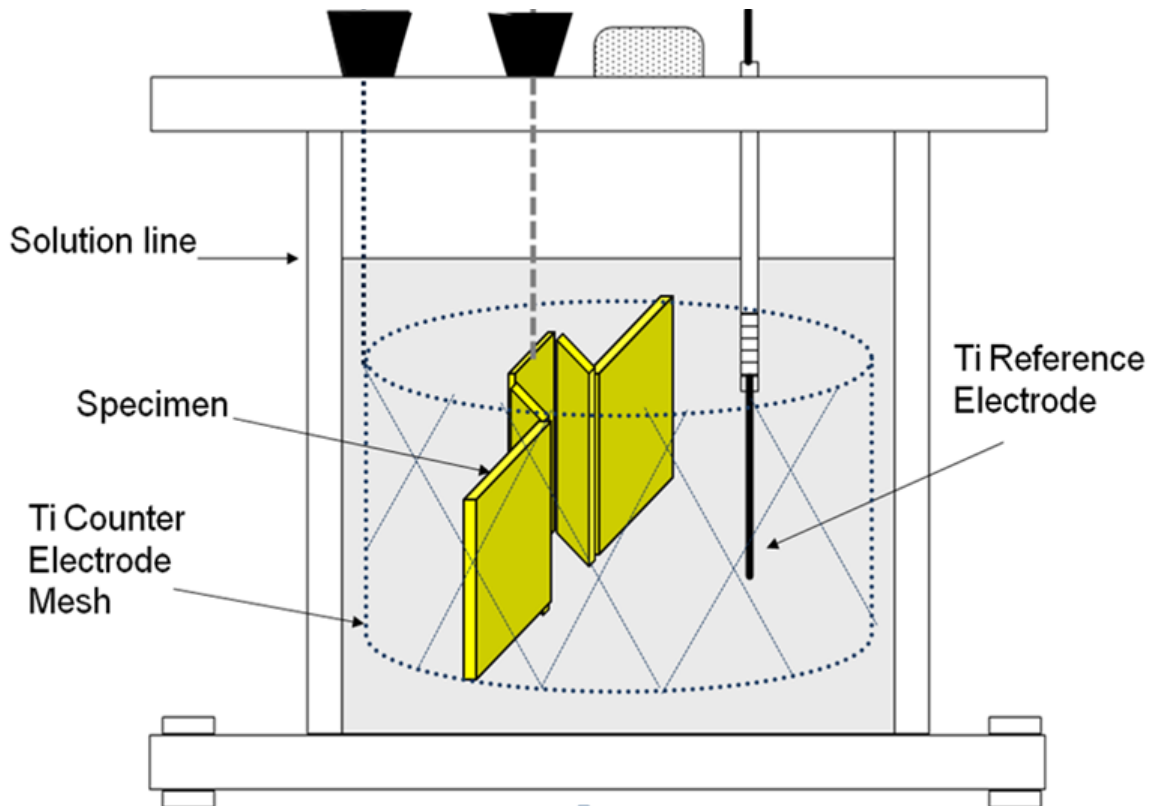


Figure 27: Three-electrode cell configuration for the SRAP experiment. Ti reference electrode (4 cm away from one face of specimen) was periodically calibrated against a saturated calomel reference electrode (SCE). Each test cell was filled with 500 mL of a solution, which was not replenished during the test.

Ribbed samples showed various instances of visible rust development along the rib bends with little indication of corrosion slowing down and with

potentials that confirmed little galvanic protection to the rest of the aluminized surface. The smooth specimens showed minor pitting, but did not indicate significant deterioration.

No significant difference was observed in potential measurements or the corrosion progression of the specimens in solution S compared to those of the specimens in the S+ solution. The findings support the hypothesis that formed regions are more susceptible to corrosion.

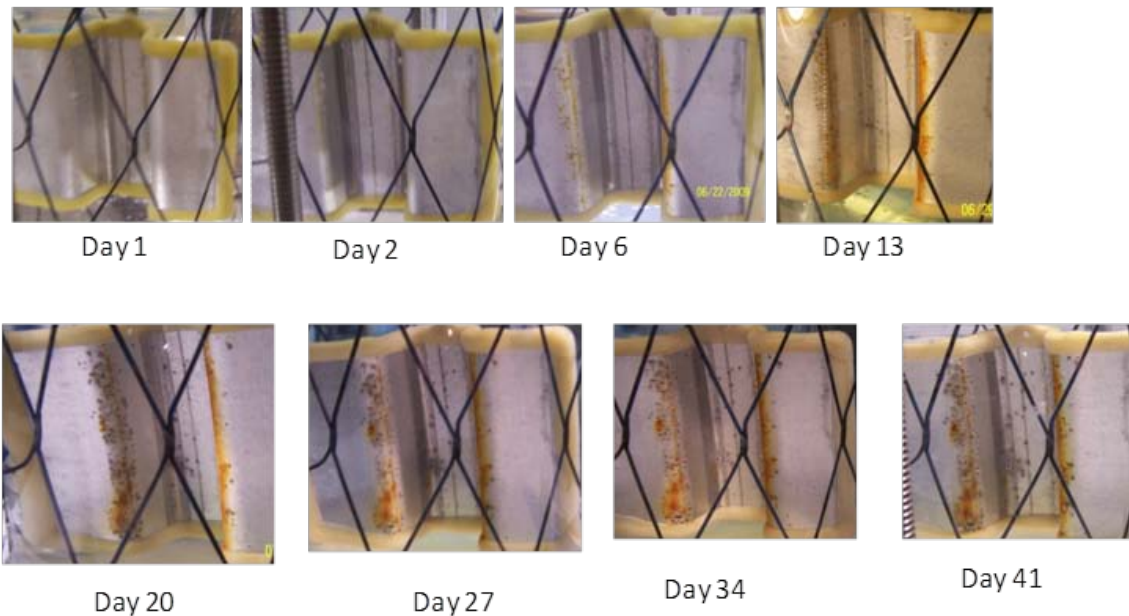


Figure 28: Corrosion progression of small ribbed specimens in solution S. the ribbed regions show significant pitting while the flat regions look bright.

6.2.2 SRAP vs PCAP in Non-flowing Waters

Since crevice corrosion (occurring underneath the epoxy), could have obscured the results of previous experiments, a new set of experiments were launched with much larger specimens. In that case, the ratio of specimen's edge

to the total surface area was less significant, reducing the effect of possible crevice corrosion on the corrosion performance of the entire system.

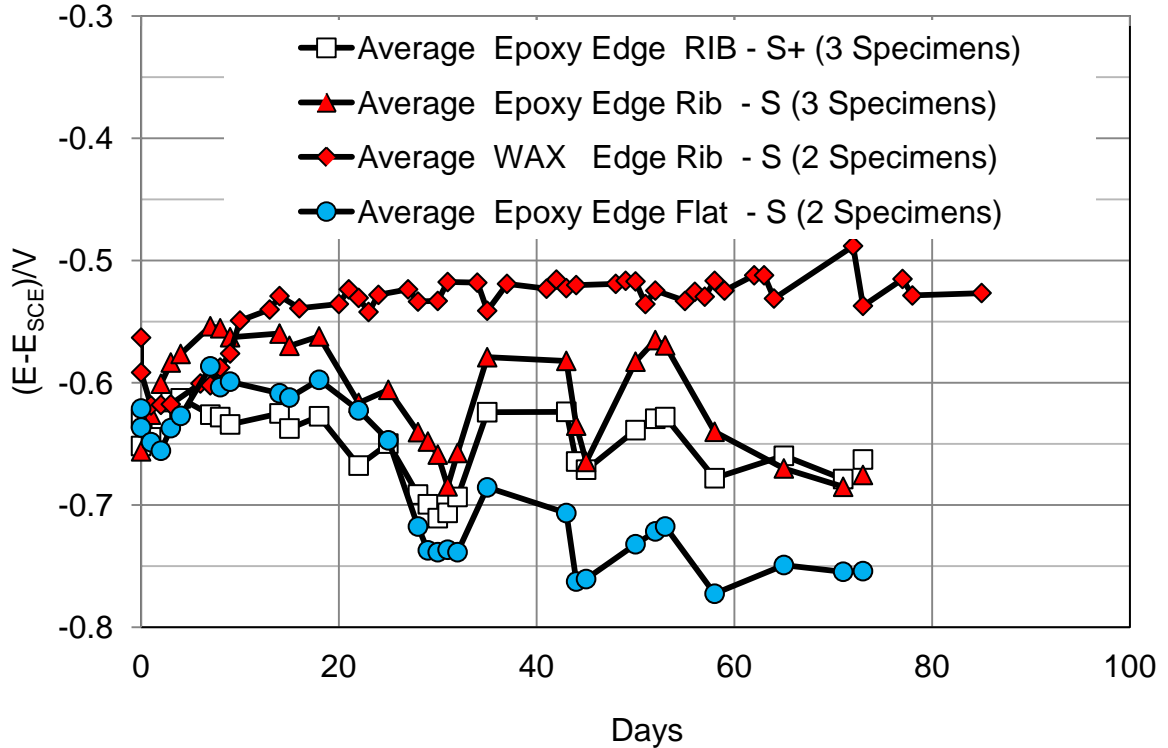


Figure 29: Average E_{OC} for small size SRAP specimens (Typical replicate variability: 41 mV).

These experiments involved comparative corrosion evaluation of regular production spiral rib aluminized pipe (SRAP) and plain corrugated aluminized pipe (PCAP) which were conducted with large pipe coupons (18 x 10 in (~46 x 25.5 cm)). A total of eight SRAP and eight PCAP specimens were cut out of newly produced pipes and were placed in eight large bins. Each bin contained two specimens of the same kind (~6 in apart) and was filled with 42 L solution S or S⁺, immersing specimens up to 2 in (5 cm) from the top as shown in the Figure 30 left. From each category (SRAP or PCAP), four specimens (in two separate

bins) were tested in solution S, and four specimens were tested in S⁺ solutions. Solutions in these experiments were not replenished and represented the stagnant water (non-flowing) conditions in the pipes. However, the solution level was kept constant by periodic additions to make up for evaporation.



Figure 30: Large SRAP specimens in a large bin (Left). Up to 5 cm of the top of the specimens were not immersed. Counter electrode inserted during EIS tests (Right).

Potential measurements were performed by inserting a Saturated Calomel Electrode (SCE) reference electrode at the center of the bin. The counter electrode used for this cell consisted of two pieces of activated Ti meshes stitched on the faces of two plastic panels with a spacer in-between Figure 30 right. The mesh pieces were electrically connected. This counter electrode would slide between the specimens, to provide a uniform convergence parallel to the

faces of the specimens, during EIS tests. All tests were conducted at room temperature. After exposure, the specimens were extracted and inspected for crevice corrosion. No crevice corrosion indications were observed in any of the cases.

Figure 31 illustrates the typical surface discoloration that occurred on both SRAP and PCAP specimens after about two years of exposure. The discoloration occurred below the water line, while the top of the specimens (above the water line) stayed bright. Minor pitting of aluminum occurred after a year of exposure in both solutions. Figure 32 shows the typical appearance of a pit at the rib region after a year of exposure. EDS confirmed the presence of aluminum corrosion products at the dark grey regions and iron corrosion products at the seams.

Apart from minor pitting, and the observed coating discoloration, corrosion was not pronounced. The metallographic cross-section of extracted specimens was compared to unexposed specimens. As show in the example in Figure 33, the coating loss observed after two and half years of exposure was found to be insignificant. EIS measurements also demonstrated extremely low corrosion rates ($< 1-2 \mu\text{m}/\text{yr}$) in both aggressive and nonaggressive solutions indicating reasonable corrosion resistance of aluminized pipes to simulated natural waters.



Figure 31: PCAP and SRAP specimens in solution S (Top) and S⁺ (Bottom) after ~700 days of exposure (specimens internal ID code: Bin 1 E2 (Top-right), Bin 6 R7 (Bottom-right), Bin 3 E1 (Top-left) and Bin 8 C7 (Bottom-left)).



Figure 32: Pits and corrosion product at ribbed regions of an in-situ SRAP specimen in S⁺ solution after ~300 days of exposure. 1 mm markers (specimen internal ID code: Bin 7 R8).

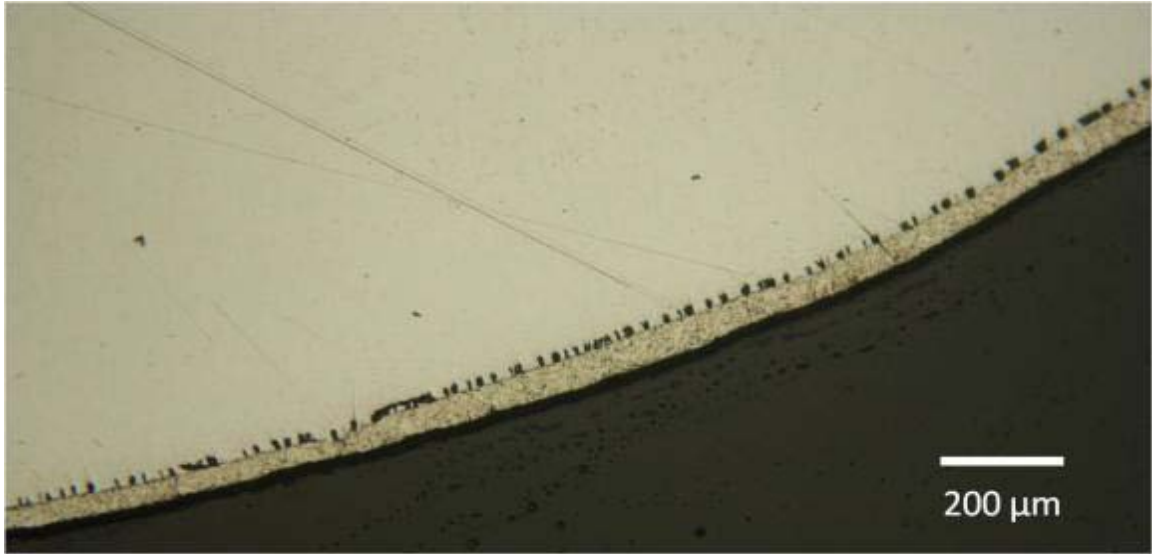


Figure 33: Metallographic cross-section of SRAP at rib regions after two years of exposure to solution S. No significant coating loss is observed (specimen internal ID code: Bin 1 E2).

The E_{OC} (Figure 34) is slightly more positive for SRAP in solution S where aluminum is mostly passive, and the system is polarized due to steel substrate exposure at the formed regions.

Figure 35 compares the apparent corrosion current density of two categories of pipes (SRAP and PCAP) in solutions S and S+ (see end of section 6.1 for calculation of corrosion current densities). While slightly higher corrosion rates took place for SRAP in aggressive solution, no dramatic difference was observed suggesting no inherent deficiency with the normal production of these pipes.

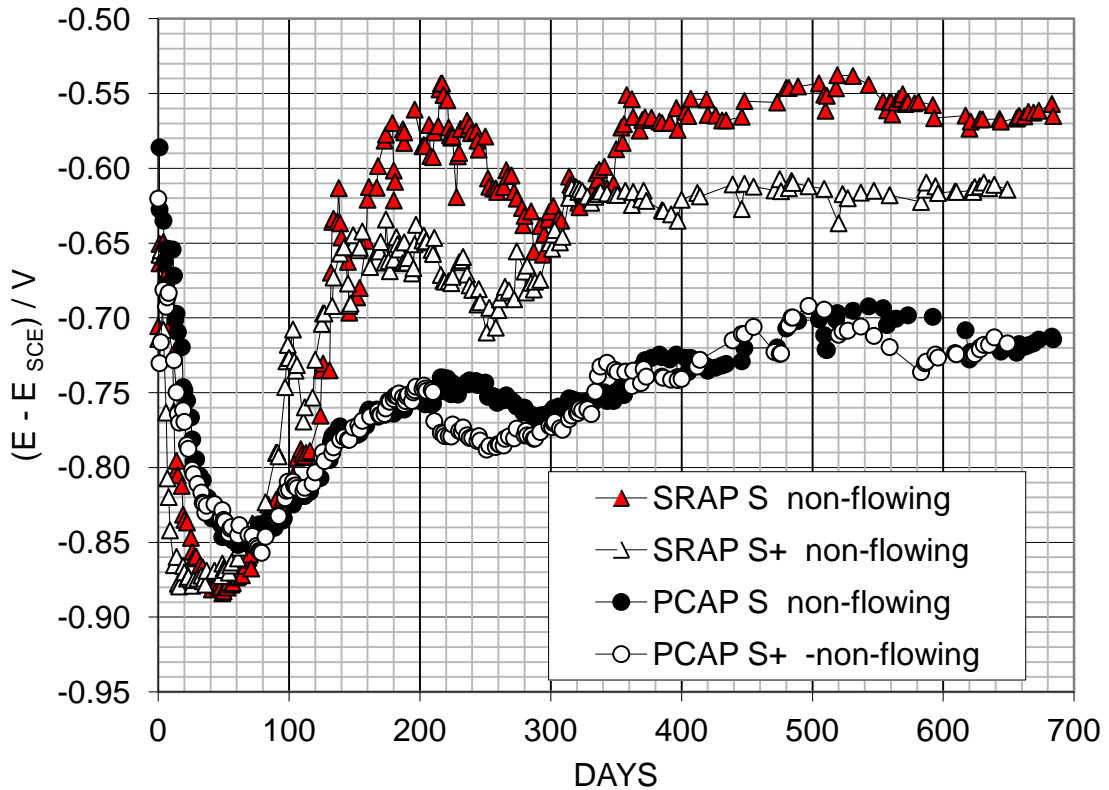


Figure 34: Average E_{OC} of SRAP and PCAP in S and S+ solution (Typical replicate variability: 26 mV (see explanation in Section 6.2.1).

It may be argued that the low corrosion rates observed for SRAP and PCAP in these experiments was due to a high concentration of ionic corrosion products in the stagnant waters which may arrest the progression of the corrosion processes. To test this hypothesis, solution S was renewed for two of the quadruplicate specimens at about ~560 days of exposure. Figure 36 and 37 demonstrate only insignificant change in E_{OC} and corrosion rates after solution renewal, suggesting that the low corrosion rates are not the result of compositional changes in the solutions.

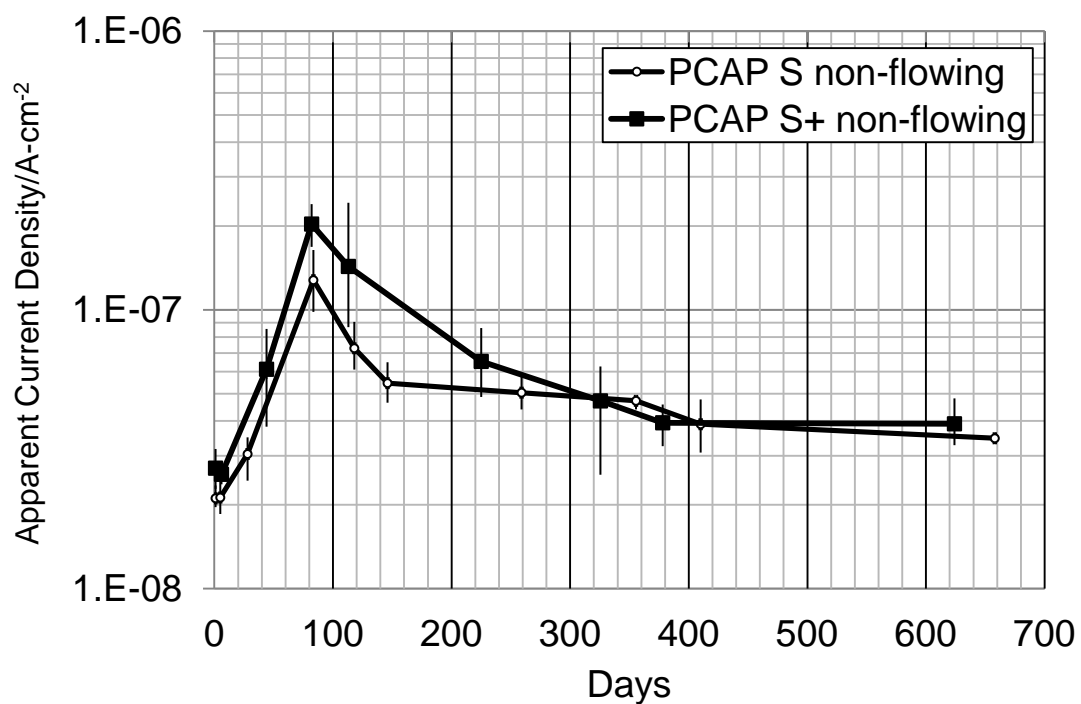
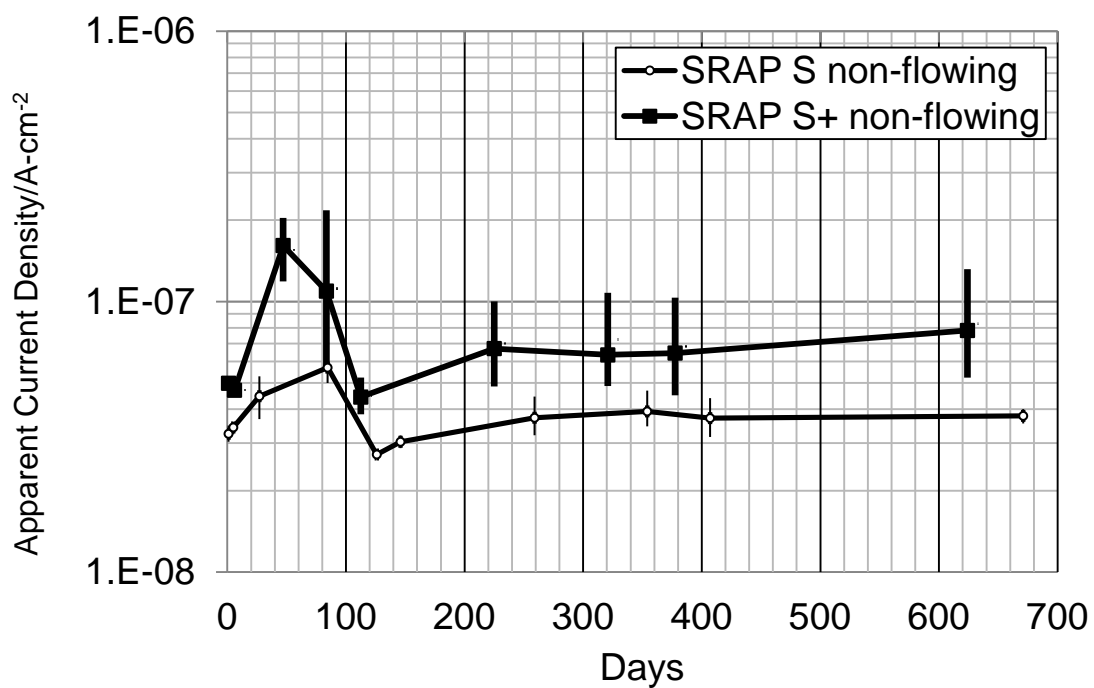


Figure 35: Apparent corrosion current density (average of quadruplicates) of SRAP (Top) and PCAP (Bottom) in solution S and S+. Bars indicate range of values.

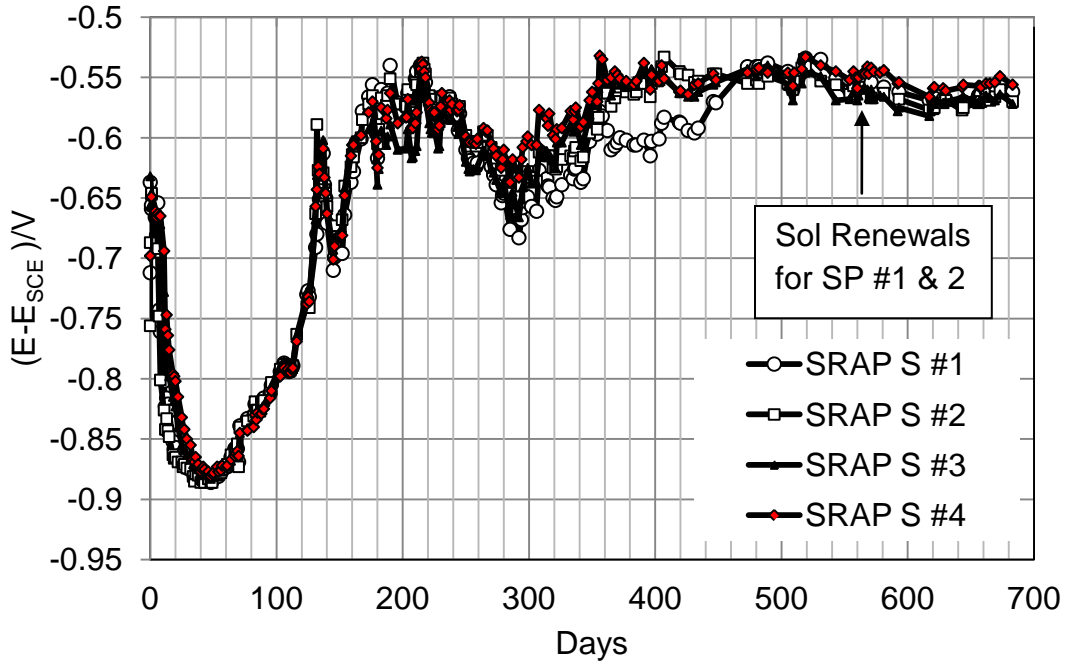


Figure 36: E_{OC} of quadruplicate SRAP specimens in solution S. Solution was renewed for SRAP S #1 and SRAP S #2 at ~560 days of exposure. No change observed.

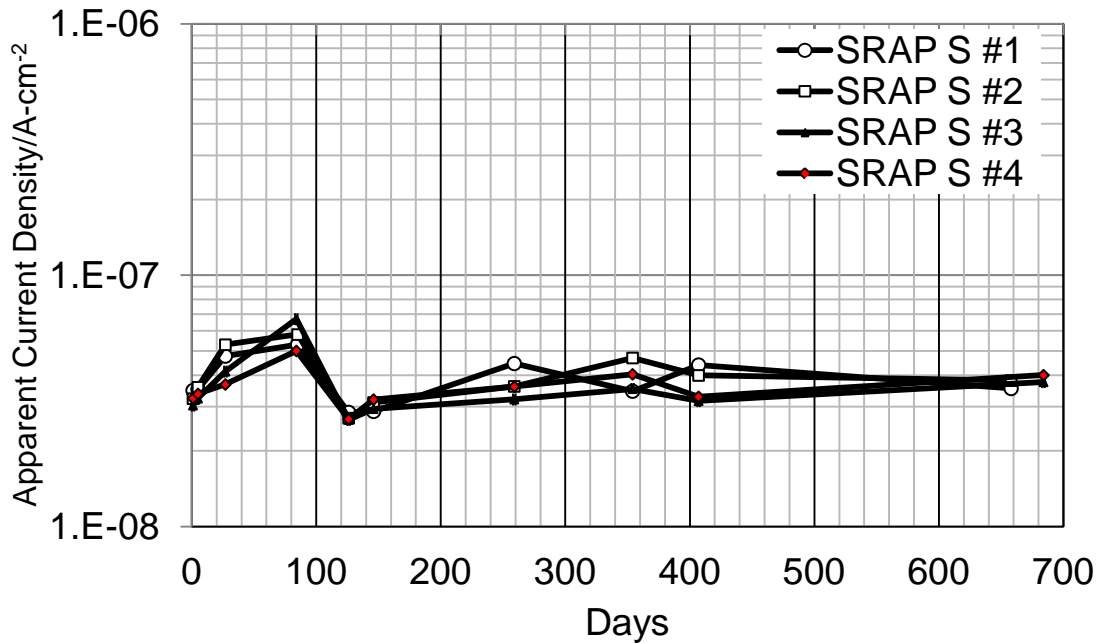


Figure 37: Apparent corrosion current density of quadruplicate SRAP specimens in solution S. Solution was renewed for SRAP S #1 and SRAP S #2 at ~560 days of exposure. No change observed.

6.2.3 SRAP in Flowing Waters

To simulate the condition of the pipe in the rainy season, where water constantly flows in the pipes, a new set of experiments, with simulated flowing waters, were conducted. It should be noted that abrasion due to flowing water for steep slope pipe installations is a major damaging factor. However, in most Florida pipe installations, due to flat landform, the pipe slopes are negligible. Therefore, abrasion is not a significant damaging factor in Florida, and that mechanism was not considered here

For this set of experiments, SRAP quadruplicate specimens similar to those described in section 6.2.2 were exposed to solution S. The solution was constantly replenished at a slow rate of two liters per day.

The results for the first 200 days of exposure indicate no significant difference between non-flowing and flowing conditions. As it is shown in Figure 38 and 39, the average E_{OC} and measured currents of the flowing and non-flowing regimes were closely matched indicating minimal corrosion in all cases.

Consequently, water replenishment does not appear to be an important variable in these phenomena which is in agreement with the observation in the previous section.

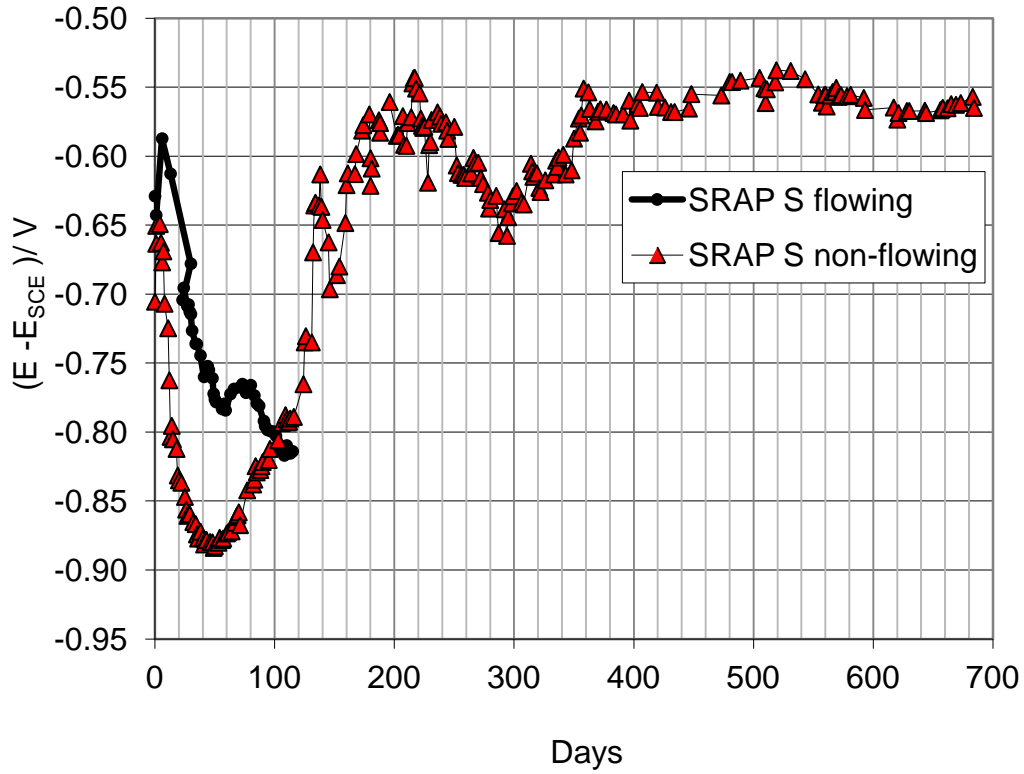


Figure 38: Average E_{OC} of SRAP in solution S -flowing vs. non-flowing condition. (Typical replicate variability: 13 mV (see explanation in Section 6.2.1)).

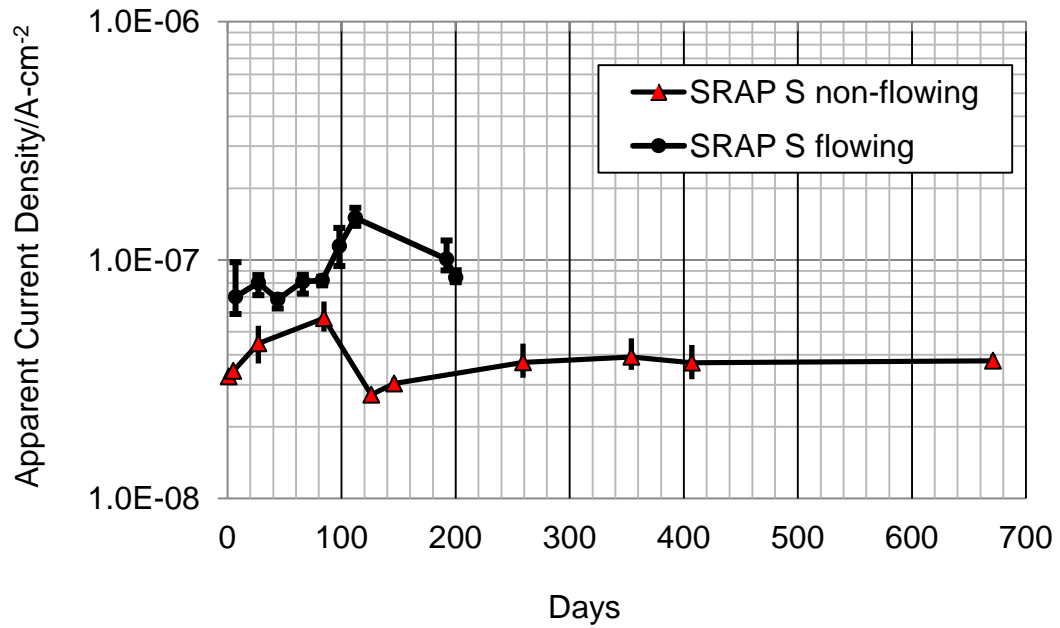


Figure 39: Apparent corrosion current density (average and range) of SRAP in solution S -flowing vs. non-flowing condition.

6.3 Corrosion and Simulated Severe Manufacturing Distress

Aluminized steel with exposed cut edges replicates the severe manufacturing distress cases. Corroded exposed steel regions at cut areas are expected to enhance the cathodic reaction accelerating the corrosion of aluminum next to rusted areas. As aluminum loss continues, more steel substrate would be exposed developing a stronger cathode. This mechanism could result in lateral propagation of corrosion. Such mechanism was investigated next.

6.3.1 Laboratory Experiments

To test the above hypothesis, eight 8.5 x 9 in (21.6 x 22.9 cm) square specimens were cut out of a 16-gage flat sheet of stock, as-received aluminized steel. Specimens were cleaned with ethanol; then, the edges of four specimens were covered with EP-308 industrial epoxy while the edges of other four specimens were left uncovered to expose the steel substrate. Each specimen with covered edges was matched and electrically connected to an exposed (cut) edge specimen. An electrical connection was made with a wire joined to the top of the specimens (Figure 40, top left). The connections between the wires and the specimens were covered with epoxy. The initial surface area of exposed steel was calculated to be less than 2% of the total surface area of aluminum. Each set of specimens were placed vertically in 5 gallon buckets ~10 cm apart (Figure 40, top right) and were fully immersed in solution S or S⁺. Potential measurements were performed by inserting a Saturated Calomel Electrode

(SCE) reference electrode in the center of the bucket. Galvanic current between the two specimens was measured by temporarily placing a Hewlett Packard (HP) 34401A multimeter along the connection between the two specimens. Two current values were obtained by connecting the negative terminal of multimeter to the specimen with covered edges and positive terminal to the cut edge specimen and then switching the connections without interrupting the current. Based on the sign of the current, it was determined that the cut edge specimen was a cathode and the specimen with covered edges was the anode. The absolute value of these two measured currents were averaged to obtain the magnitude of macrocell currents and to compare the corrosion behavior. A counter electrode was built by placing activated Ti mesh pieces on the faces of three plastic panels with spacers in-between and interconnecting the Ti mesh pieces (Figure 40, bottom). This counter electrode would slide between the specimens to provide uniform convergence, parallel to the faces of specimens, during EIS tests.

Figure 41 illustrates the E_{OC} evolution of the combined exposed edge-aluminized surface system while Figure 42 shows the value of apparent corrosion current density and macrocell current. From the beginning of the exposure, the galvanic current flowed between the connected specimens. As expected, galvanic current measurements confirmed that the corroding steel edge was the cathode. This current gradually increased with time for the first 200 days as the cathode area increased (more steel corroded). During this period,

the lateral discoloration and corrosion propagation of aluminum, initiating from the edges, continued.

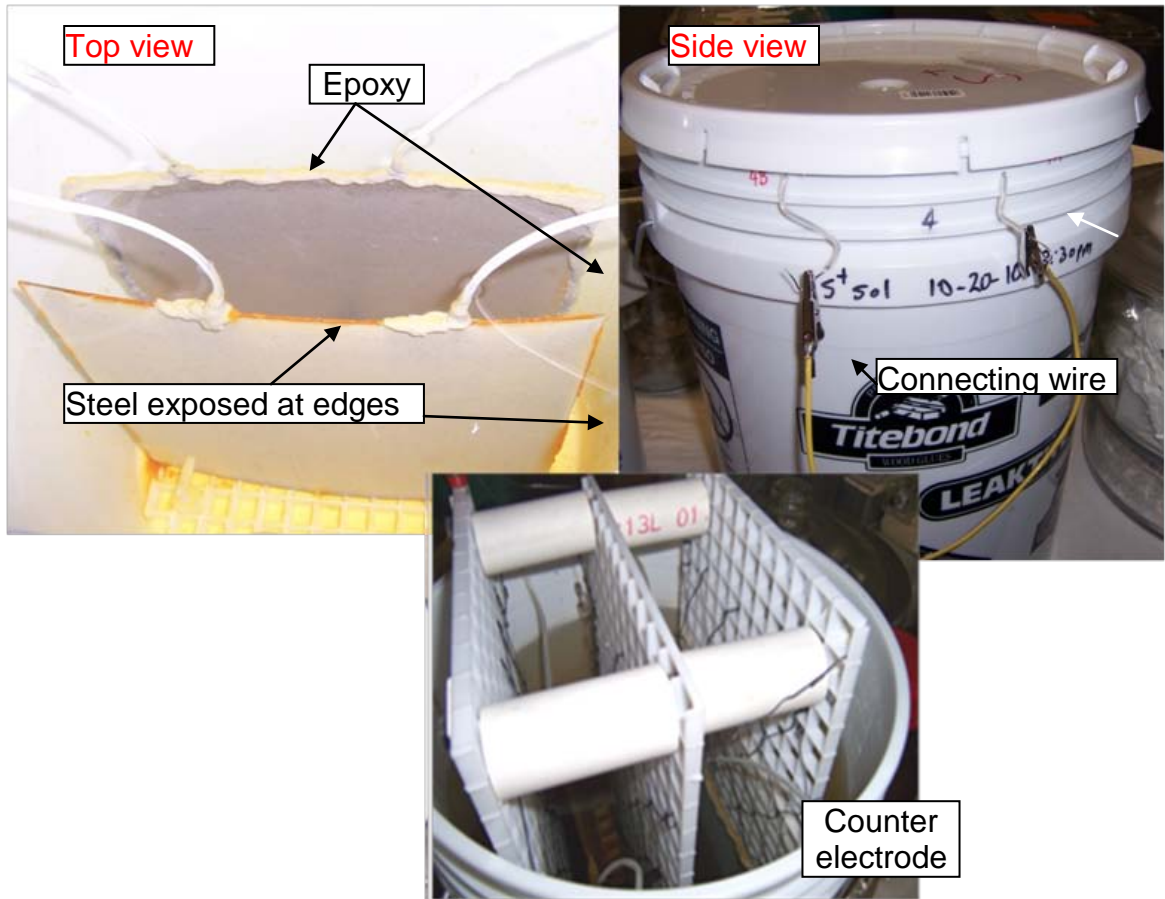


Figure 40: Exposed cut edge experiment set up to simulate severe manufacturing damage.

At ~175 days of exposure, the specimens were extracted for a few hours for surface inspections and were placed back into the cells in fresh solutions (Figure 43). Following the solution replenishment, the galvanic current between the sealed-edge and exposed-edge sections significantly increased for ~30 days; this increase was accompanied with an open circuit potential drop in all cells (Figure 41). It appears that the process of extraction and solution replenishment

may have removed some of the iron corrosion product on the edges of exposed-edge specimens. The rust may have previously hindered or slowed down the corrosion rate, and the removal of corrosion products provided fresh sites for corrosion progression. As the corrosion rate of exposed edges increased aluminum tends to provide higher galvanic protection by sending greater current. No strong correlation was observed between electrochemical trends and the limited temperature fluctuations during the tests (Figure 41).

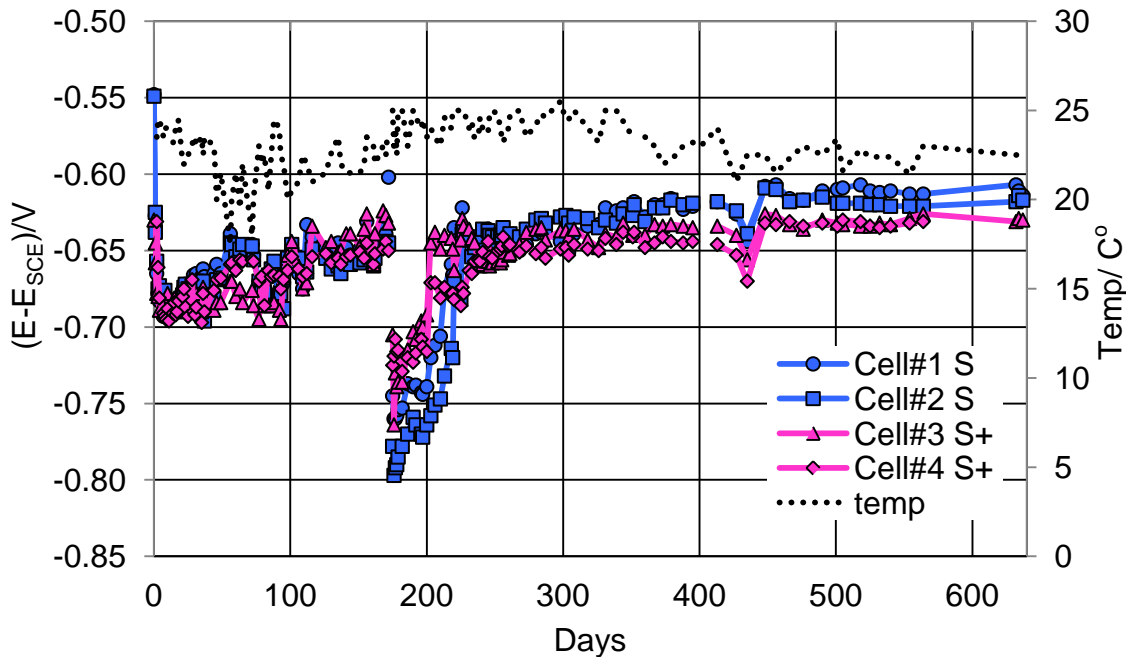


Figure 41: E_{OC} of open cut edge experiments (specimens taken out at 175 days).

After 200 days of exposure, when most of the aluminum was discolored, the galvanic current gradually decreased with time to low values. The reduction of the galvanic corrosion rate may indicate some surface alteration process that hinders the rate of the anodic reaction on the aluminum surface. In any event, the galvanic protection, although present from the beginning of the exposure, was

not sufficient to provide full protection to the steel at the open edges even for such small area fractions of cathode to anode. This occurrence is consistent with the presence of rust at the edges and the less negative mixed potential values that approach the typical potential of corroding steel in neutral water (McCafferty, 2010).

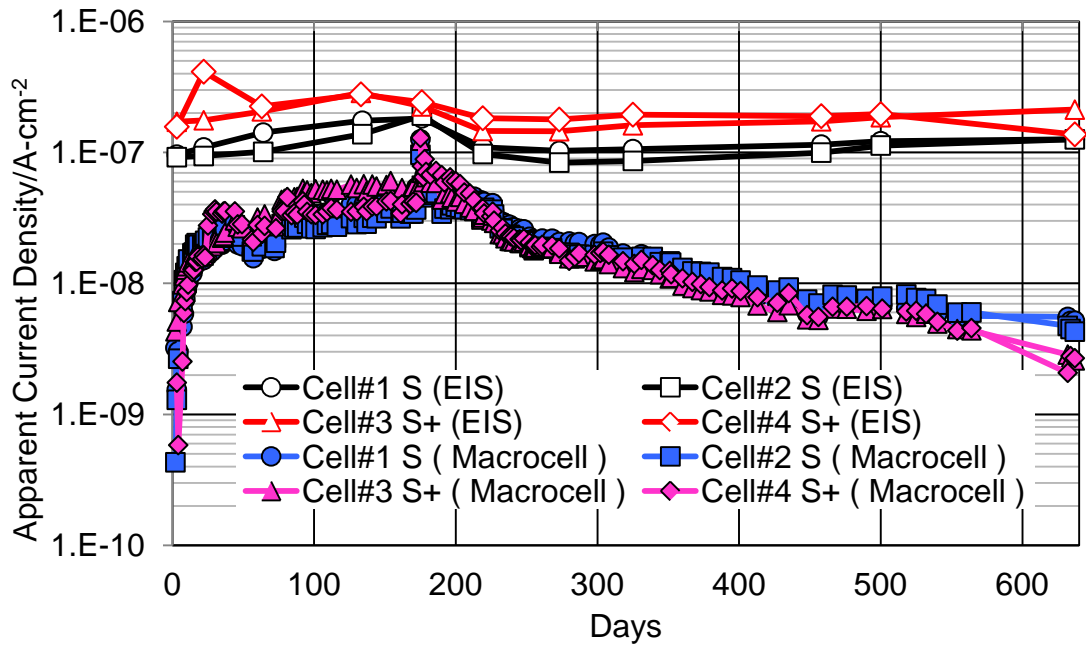


Figure 42: Macrocell current compared to apparent corrosion current density obtained from EIS tests.

The corrosion current density measured by EIS tests indicates a low, but relatively constant, corrosion rate. It should be indicated that, for the calculation of this current density, the entire area of the anode (aluminum) was considered. However, if one only considered the narrow discolored areas of aluminum, immediately adjacent to the corroding steel, the corrosion rate would be more than one order of magnitude greater. Determination of nominal corroding area to be used for corrosion current density is a difficult task as this area changes by

time. Another complication in interpreting the EIS data is the effect of corroding cathode (steel) that is not stationary and its area also changes with time. These factors need consideration in subsequent investigations.

After 600 days of exposure, the experiment was terminated and the cut edge specimens from solution S and S+ were extracted for metallographic examination. Metal strips along the edges were cut out from the extracted specimens, rinsed with ethanol, casted in epoxy, and polished to 1 μ m. Figure 44 shows metallographic cross sections of metal strips at the edges of the specimens in both solutions. In both solutions there was significant loss of steel at the edge, and the aluminum coating near the cut edges was severely corroded as well (Figure 44 right) which indicates that the aluminum tended to protect the steel substrate to some extent. More photos of specimens and their metallographic cross sections are shown in Appendix 3. It could be thought that the steel cross section shape near the edge reflected plastic deformation by shear while cutting and preparation of the specimens and not corrosion. However, etching of the cross sections, as illustrated for a specimen in S⁺ (Figure A-11), showed a progression of metal wastage into a generally equiaxed grain microstructure, instead of the kind of grain elongation that would be expected if the cross section shape were due to severe plastic deformation. Therefore, the channel-like corrosion of the steel substrate at the edges seems largely unrelated to any mechanical artifacts and due mainly to the corrosion progression pattern. The aluminum coating loss near the edge indicates the presence of some galvanic protection to the exposed steel in conditions comparable to those of

Mode A. Steel loss near the cut edge beneath the corroded aluminum is also observed (black region underneath the Al coating Figure 44 Left). It appears that the aluminum corrosion continues over a longer distance from the cut edge in solution S⁺ compared to solution S. The steel loss in solution S (high resistivity solution) appears to be more severe than the solution S⁺. This suggests that the protection was somewhat greater in the case of a lower resistivity environment. In summary, after about two years of exposure, the evidence shows that the cut edges corroded readily in both solutions S and S⁺ indicating inefficient aluminum galvanic protection even in the more aggressive environment.

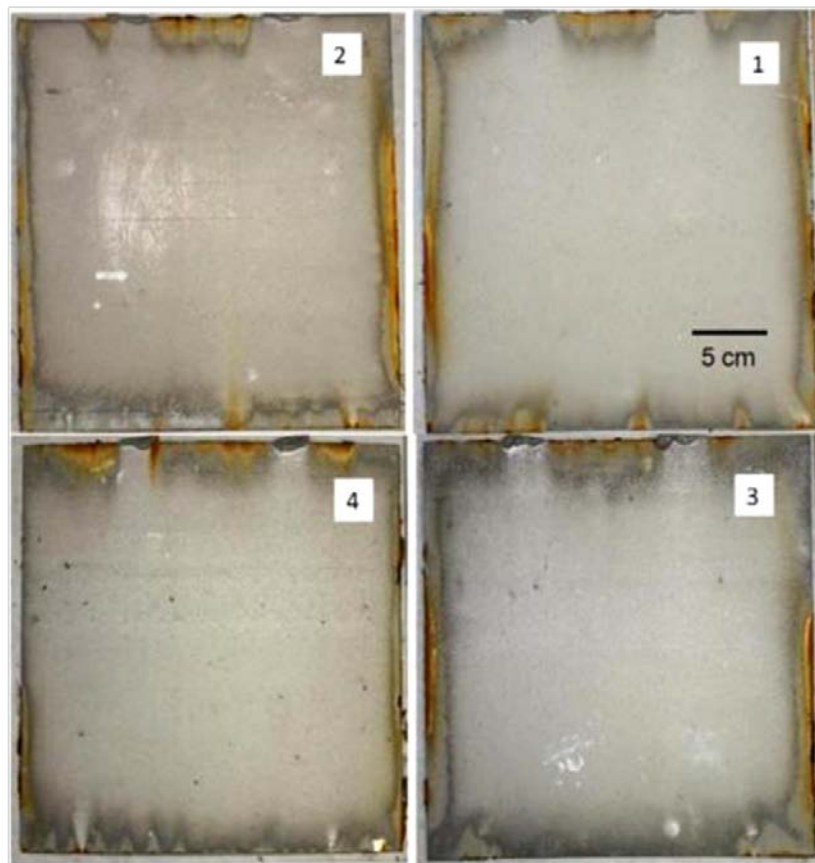


Figure 43: Exposed cut edge experiment. Specimens with exposed edges extracted from solution S (Top) and solution S⁺ (Bottom) after ~175 days of exposure. Lateral progression of corrosion is observed.

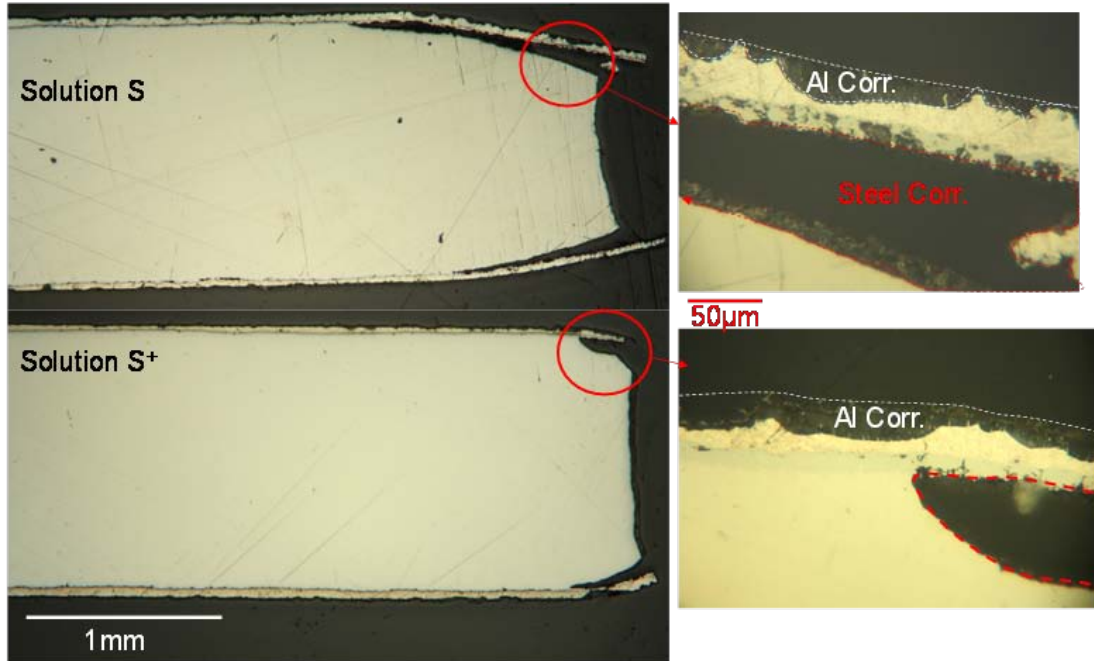


Figure 44: Metallographic cross section of the edges of aluminized steel specimens in solution S (Top) and S+ (Bottom). Significant corrosion of steel substrate and aluminum at the edges is observed in both cases.

In the next section, a simplified, computer aided model was used to simulate the conditions for the above experiment to better understand the mechanism of corrosion propagation at exposed edges.

6.3.2 Corrosion Propagation Mechanism Modeling

As discussed in section 2.2, the corrosion process at the aluminum surface with coating breaks or at exposed cut edges is expected to be aggravated by the development of rust crest at steel corroding spots. As these areas are enhanced sites for the cathodic reaction (most likely O_2 reduction).

The elevation of the potential of the system, due to corroding steel potential, further aggravates the sacrificial consumption of the surrounding

aluminum coating, that leads to additional exposure of steel substrate with subsequent intensified action and self propagation. This mechanism would cause the observation of lateral corrosion propagation, away from initially distressed ribs, in field incidents. Figure 45 demonstrate such mechanism in specimens with cut edge and blemished coating.

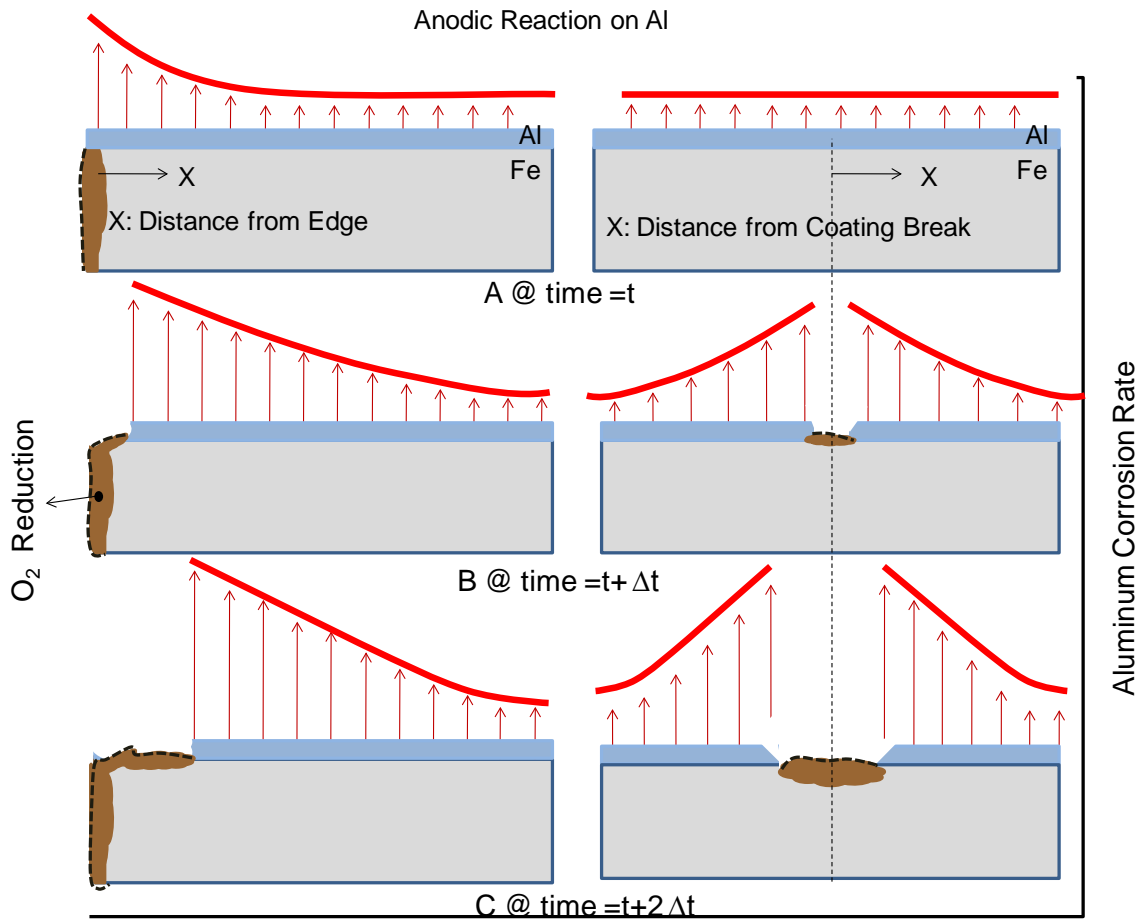


Figure 45: Speculative scenario of conditions at cut edge or localized aluminized coating break. Anodic corrosion rate of aluminum (red arrows) as a function of distance from edge (Left) and from coating break (Right). Cathodic reaction (O₂ reduction) forms the other component of the galvanic couple and takes place on steel or steel corrosion products.

In the above figure, the rate of steel corrosion is assumed to be negligible. The aluminum corrosion rate is at its peak near the junction of the galvanic couple and decreases along the distance away from the junction. As time progresses, aluminum near the junction is increasingly consumed resulting in a larger cathode.

To investigate the validity of the above hypothesis, a simplistic computer model was formulated. The model was constructed using a Finite Element Modeling (FEM) platform by Comsol Multiphysics™ to investigate the corrosion propagation pattern at cut edges of aluminized steel exposed to simulated natural waters. The geometry chosen for this simplified model, shown schematically in Figure 46, was a 2-dimensional idealization of the laboratory experiments discussed in section 6.3.1. A circular electrolyte space with a diameter (30 cm) approximating the diameter of the liquid body in the 5 gallon bucket contains a single specimen. The 2-dimensional simulation is assigned a depth of 22.9 cm to approach the height of the electrolyte in the bucket cell.

The electrolyte conductivity was made to match that of the solution S used in the tests. The specimen width in the simulation was 21.6 cm which combined with the space depth approximates the overall specimen dimensions in the bucket cell. Because of symmetry, only half of the specimen was considered. To simplify the model even more, only one edge of the specimen was treated as exposed, and the other edge was considered to be electrically insulated.

The electrochemical reactions assumed to occur at the relevant interfaces are shown next together with a designation keyed to the corresponding kinetic parameters tabulated further below:

At the surface of the aluminized layer:

- Anodic reaction:
 - Aluminum oxidation $\text{Al} \rightarrow \text{Al}^{+3} + 3 \text{e}^-$ (Reaction A)
- Cathodic reaction (treated as an equivalent uniform reaction but expected to be localized to the exposed intermetallic precipitates):
 - Oxygen reduction $\text{O}_2 + 2\text{H}_2\text{O} + 4\text{e}^- \rightarrow 4 \text{OH}^-$ (Reaction B)

At the surface of the exposed steel:

- Anodic reaction:
 - Treated as being negligible, see below.
- Cathodic reaction:
 - Oxygen reduction $\text{O}_2 + 2\text{H}_2\text{O} + 4\text{e}^- \rightarrow 4 \text{OH}^-$ (Reaction C)

Since the simulation was made mainly to examine the effect of the exposed steel on the consumption of the aluminized layer, the steel was treated as being predominantly cathodic, thus neglecting the anodic reaction there. Following other authors (e.g. Murer et al., 2010) the cathodic, oxygen reduction reaction rate on the exposed steel (Reaction C) was assigned a nominal fixed value, $4 \cdot 10^{-5} \text{ A/cm}^2$ in terms of current density. That value is typical of diffusion limited regimes and generally representative of the behavior observed in the polarization diagrams that are presented in Appendix 1.

The calculations for potentials and current density distributions were conducted for a total of 4 conditions in which the aluminum coating was considered to have been consumed (no loss, 0.4 mm, 1mm and 3.5 mm) from the edge.

The ruling equations for each of the reactions are given in Table 3. There, i_a and i_c designate the current densities for the anodic and the cathodic reactions respectively. The identification and the value of each parameter are given in Table 4. Some of these values are abstracted from typical results obtained from polarization tests conducted on aluminized steel and bare steel specimens in similar environments (Appendix 1); others, such as the oxygen diffusion coefficient and the oxygen concentration value in solution, are obtained from literature sources (Sagüés and Kranc, 1992).

Table 3: System of equations applied in the model

Anodic Reaction (A): $i_a = i_{oa} * 10^{[(E-E_{oa})/\beta_a]}$
Cathodic Reaction (B): $i_c = i_{oc} * (C/Co) * 10^{[(E_{oc}-E)/\beta_c]}$
Cathodic Reaction (C): $i_c = -0.4 \text{ A/cm}^2$
O ₂ Mass Transport Linked to Cathodic Process: $i_c = -/ + nFD \frac{dC}{ds} _{\text{surface}}$ (Orazem, 2008)
Electric Charge Transport Linked to Cathodic Process: $i_a + i_c = -/+ \sigma dE/ds _{\text{surface}}$ (Orazem, 2008)
Mass Conservation in Bulk: $\nabla^2 C = 0$
Charge Conservation in Bulk: $\nabla^2 E = 0$

The governing equations and conditions are further illustrated in Figure 46. Comsol's approach in solving FEM was not in the scope of this work. When modeling the current and potential distribution for a metal immersed in a medium, it is customary to model the potentials and currents in the space corresponding to the surrounding medium with appropriate boundary conditions at the interfaces where the medium meets the metal (Murer et al., 2010). Because of the high conductivity of the metal, it is treated as an equipotential entity. The sign convention used in this model is such that all potentials are with respect to the metal. Thus, the more positive E is, the faster the rate of the reaction tends to be (Sagüés and Kranc, 1992).

Examples of model output for the potential distribution and current density distribution for the case with 0.5 mm coating loss are shown in Figure 47 and 48. As it is illustrated in these figures, the potential of the solution with respect to the metal is about 70 mV more negative at the edge. Therefore, based on the sign convention and Tafel slopes used, the aluminum at the coating break is polarized in the anodic direction compared to the rest of the exposed aluminized coating. This is an indication that the aluminum next to the cut edge is corroding faster than elsewhere, in accordance with the initial assumptions. These conditions are further illustrated by the current density patterns in Figure 48, showing the current concentration at the edge (indicative of greater galvanic current action between aluminum and steel).

Figures 49 and 50 illustrate aluminum anodic current densities and potentials along the metal-solution boundary for three different cases with

different sizes of coating loss regions near the cut edge. As shown in these figures, the anodic current density for the case with greater size of coating break (3.5 mm, shown in pink-thick line) correspond to the largest corrosion rate and most positive potentials. Right near the edge the current density is about $10 \mu\text{A}/\text{cm}^2$ ($\sim 100 \mu\text{m}/\text{yr}$); with such corrosion rates, the aluminum coating will be fully consumed in less than a year.

Table 4: Input parameters for finite element modeling

Reaction	Parameters	Value	Unit	Description
A	β_a	0.1	[V]	Activation Tafel constant for Al anodic reaction.
A	i_{oa}	1.00E-08	[A/m ²]	Exchange current density for the Al anodic reaction
A	E_{oa}	1	[V]	Equilibrium potential for Al anodic reaction.
B	β_c	0.16	[V]	Activation Tafel constant for oxygen reduction on passive Al in solution.
B	i_{oc}	1.00E-05	[A/m ²]	Exchange current density for Al cathodic reaction
B	E_{oc}	0.6	[V]	Equilibrium potential for Al cathodic reaction.
C	i_c	-0.4	[A/m ²]	Cathodic current density for steel
	σ	2.00E-02	[S/m]	Solution resistivity
	D	1.00E-01	[m ² /sec]	Diffusion coefficient for oxygen in solution
	F	96500	[C/mol]	Faraday's constant
B	n_{O_2}	4		Valence of O ₂
A	n_{Al}	3		Valence of the Al
	C_o	0.25	[mol/m ³]	Effective oxygen concentration in solution

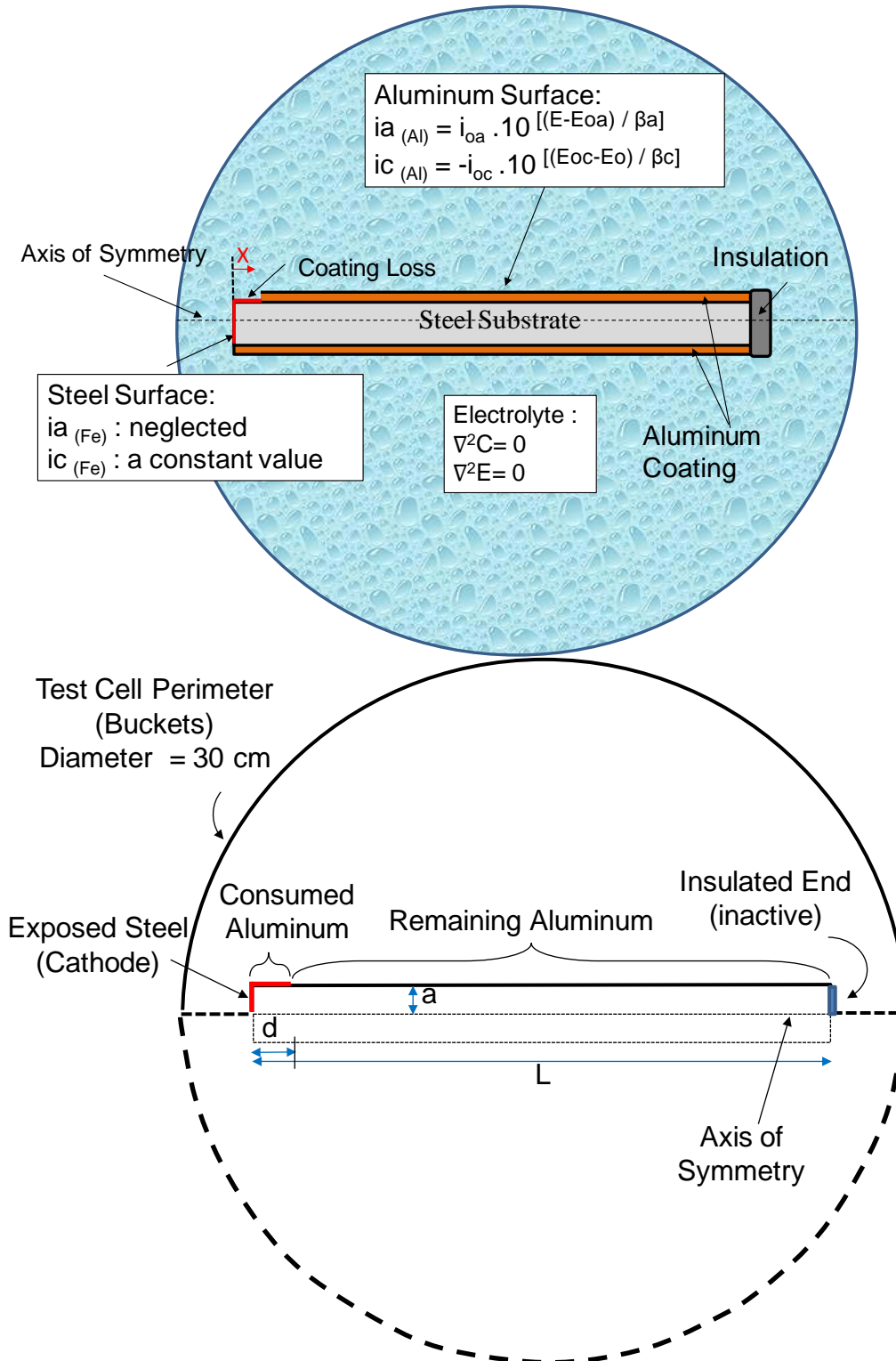


Figure 46: Conditions applied to an aluminized specimen with cut edges immersed in an electrolyte under steady state condition. Some dimensions are not to scale for clarity. $d = 0, 0.5, 3.5, 0.4$ mm; $L = \sim 21.6$ cm, $a = \sim 0.8$ mm.

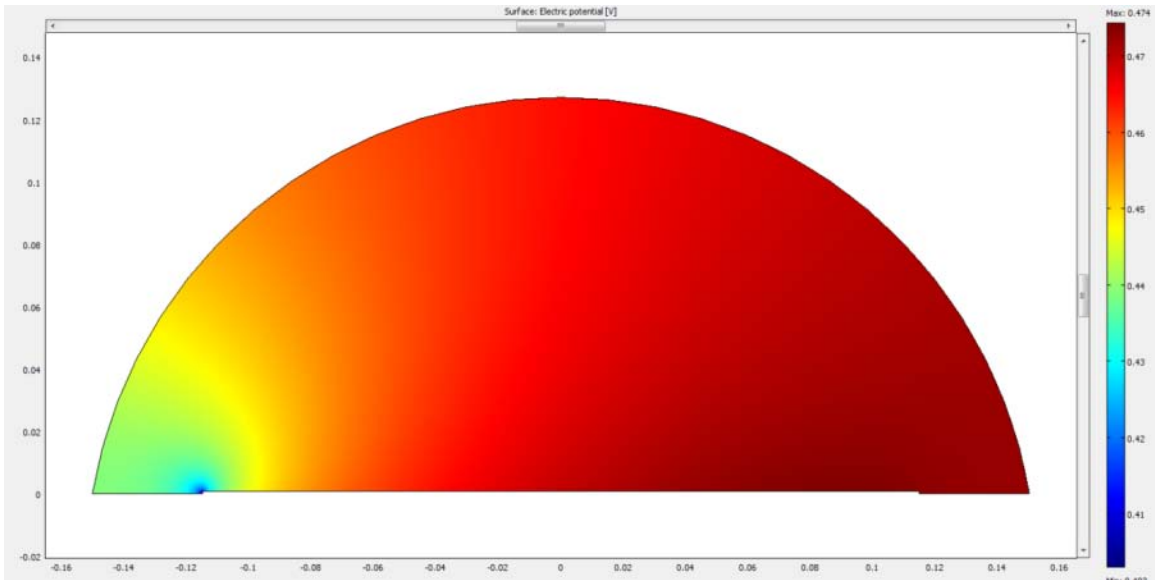


Figure 47: Computer model for potential distribution (Blue 0.40V, Red 0.47V) (0.5mm coating lost).

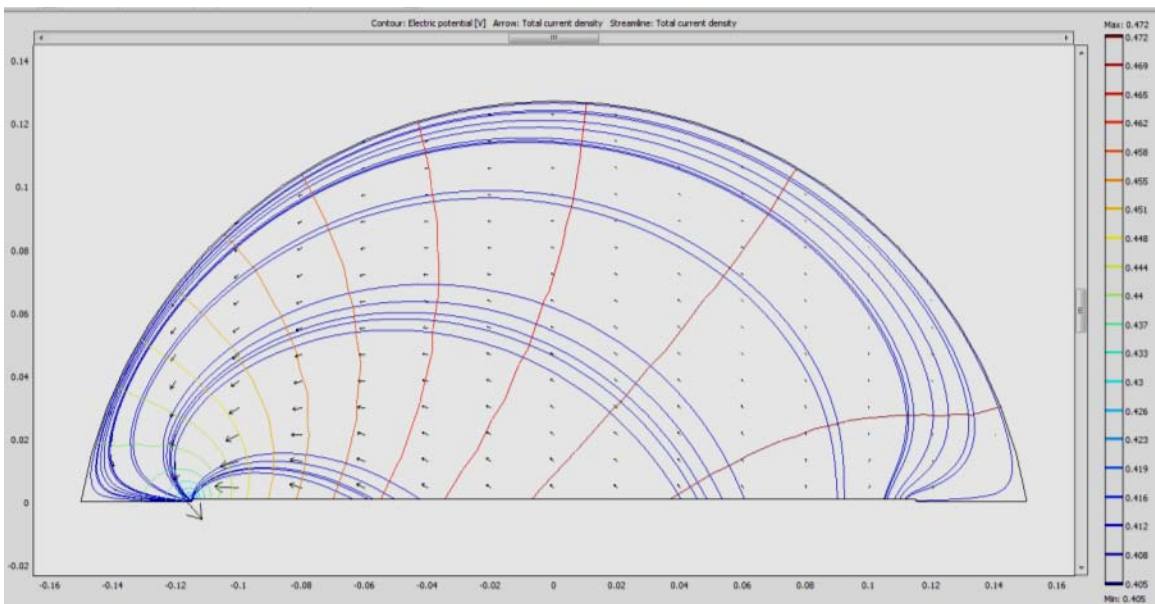


Figure 48: Computer model results: streamline: total current density, arrow: direction of current, and contour: potential (0.5mm coating lost)

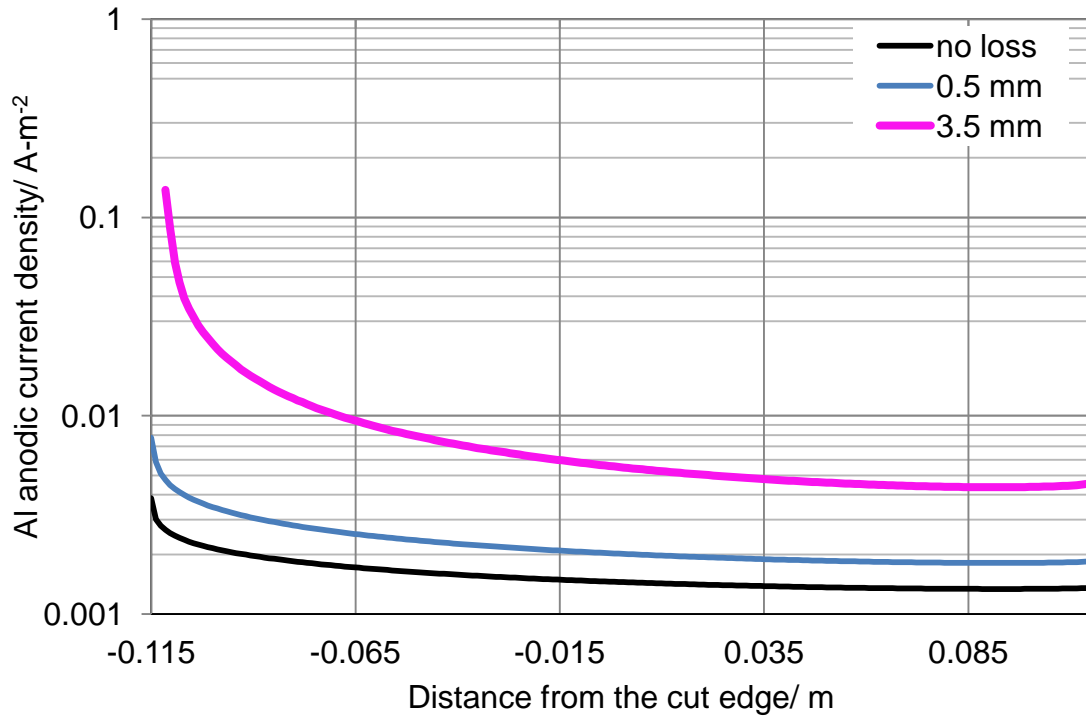


Figure 49: Aluminum anodic current densities as the function of X-axis for aluminum boundary. The cut edge is located at -.115 m on the X-axis.

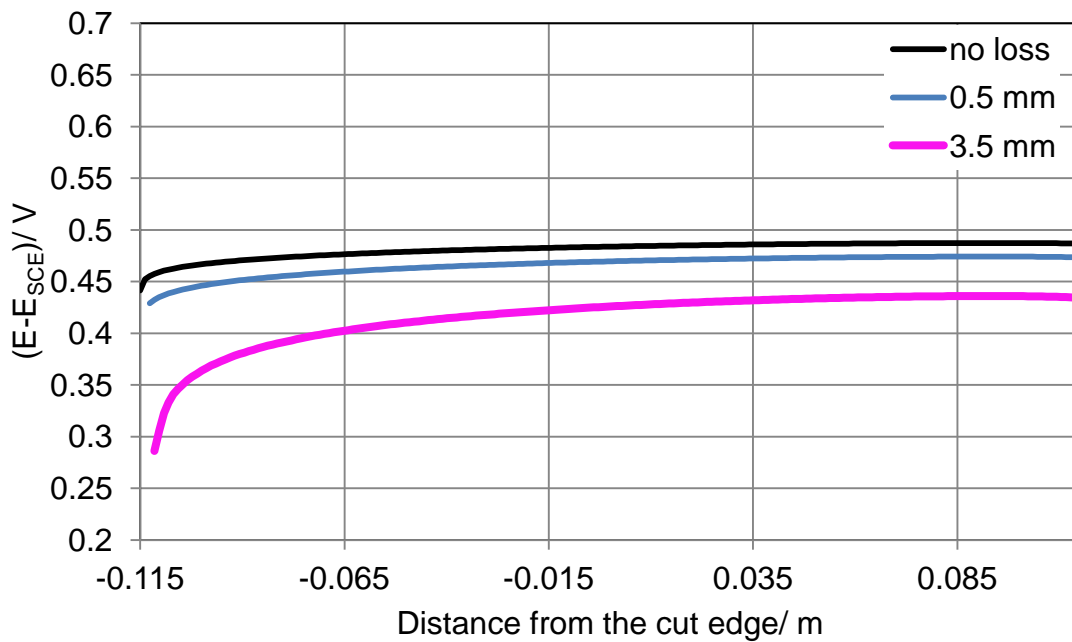


Figure 50: Potential vs. saturated calomel ref. electrode as the function of X-axis for aluminum boundary. The cut edge is located at -.115 m on the X-axis.

In summary, the findings from this model are in general agreement with finding in section 6.3. As shown in metallographic cross-section of exposed edges (Figure 44), aluminum is susceptible to more corrosion at the edges; however, the model is limited in the sense that it doesn't consider the corrosion of the steel substrate. As mention in section 6.3, steel corroded severely at the edges and the galvanic protection provided by aluminum was not sufficient.

Therefore, the model implementation used corrosion kinetic parameters that represented rough estimates of the actual values. Hence these calculations must be viewed as preliminary, semi-quantitative indications of the actual conditions. For example, the potential values in Figure 50 deviate greatly from the absolute values observed experimentally. Nevertheless, the model output shows relative trends that are consistent with the overall expectations and provide further insight into the prevalent mechanisms. To create a realistic model, additional parameters are needed to account for the anodic corrosion of steel; such parameters should be considered in future investigations.

7. MODE B: MECHANISM OF CORROSION PERFORMANCE IN WATER CONTACTING SAND AND LIMESTONE

In this major area of the work, experiments are conducted to elucidate the mechanism responsible for Mode B corrosion. Accordingly, the corrosion behavior of aluminized steel was evaluated in water in contact with clean sand as a relatively neutral medium, serving as a control, and in water contacting limestone.

7.1 Corrosion in Sandy Soil

According to The U.S. Department of Agriculture (USDA), Myakka fine sand was recognized as the official native soil of Florida in 1989. Myakka fine sand covers more than 1.5 million acres of Florida's land and does not occur in any other state. Myakka, an Indian word for Big Waters, has a grey fine sand surface, light gray fine sand subsurface layer, dark reddish brown fine sand with organic stains subsoil, and yellowish brown fine sand substratum layer (USDA, 2003). To simulate the basic soil condition in Florida, two sets of experiments with silica sand and distilled water were designed. In the first series, as-received specimens (2 x 3 in (5 x7.6 cm) were cut from flat aluminized sheet flat stock; the edges of specimens were covered with epoxy. These specimens were exposed to fully soaked sand in cells configured as shown in Figure 51A. In these cells, the distilled water was standing 2 in (5 cm) above the sand to insure full

saturation. Measurements of water pH and conductivity were taken by immersing the corresponding probes' sensing elements in the excess water above the sand. Results, as function of exposure time, are shown in Figures 52-53.

In the second series of experiments, similar specimens were placed in plastic cylinders that had tiny holes covered with filter paper at the bottom. The cells were filled with sand and were placed in a container filled with water up to half the height of cylinder Figure 51B. The specimens inside the cells were located above the water line to provide a moist sand condition in which the pores are not saturated. This condition was intended to increase the opportunity of corrosion by increasing oxygen access. In both series, E_{OC} and EIS measurements were conducted to determine the corrosion regime and apparent rate of corrosion of the aluminized steel specimens. Nominal polarization parameters and apparent corrosion current densities were obtained with the methodology detailed in Section 6.1. Average results of triplicate specimens in saturated sand and quadruplicate specimens in moist sand conditions are presented in Figures 54 and 55.

As indicated by pH and conductivity measurements, the near neutral environment in these tests resulted in extremely low corrosion rates of $< 1\mu\text{m}/\text{yr}$ for both saturated and moist sand experiments Figure 55. While infrequent pits were observed on the surface of some specimens, in general, the extracted specimens show no sign of severe corrosion. A typical metallographic cross section of the specimen, showing negligible wastage, is given in Figure 56.

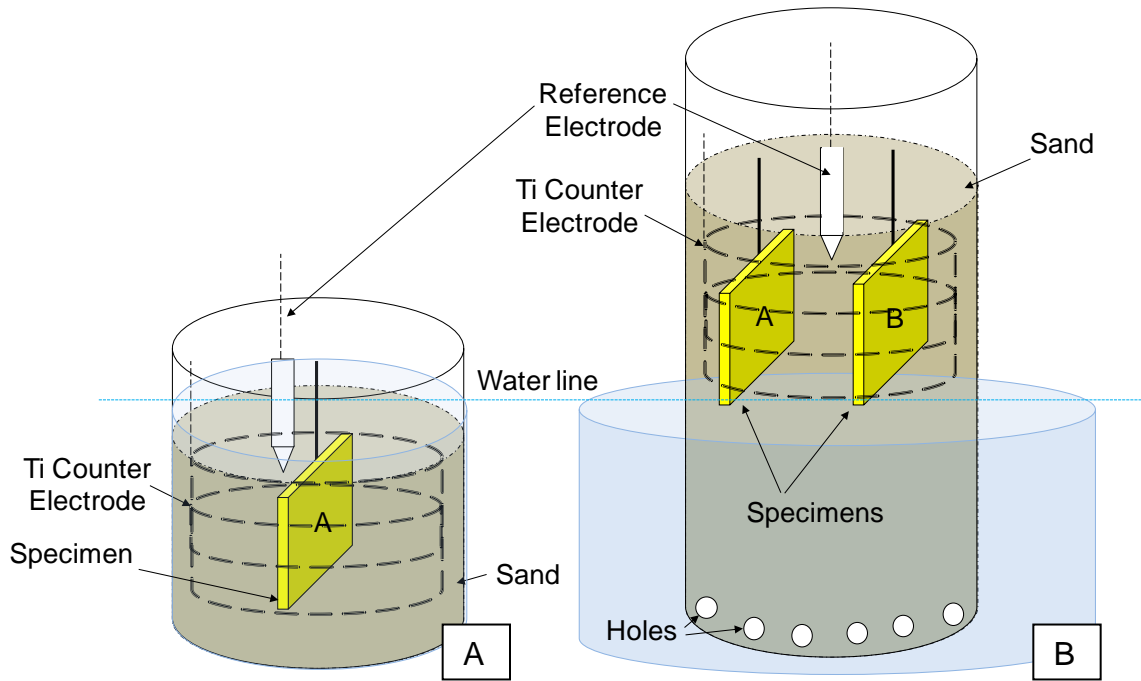


Figure 51: Sand experiment set up. A: Saturated sand experiment; B: moist sand experiment.

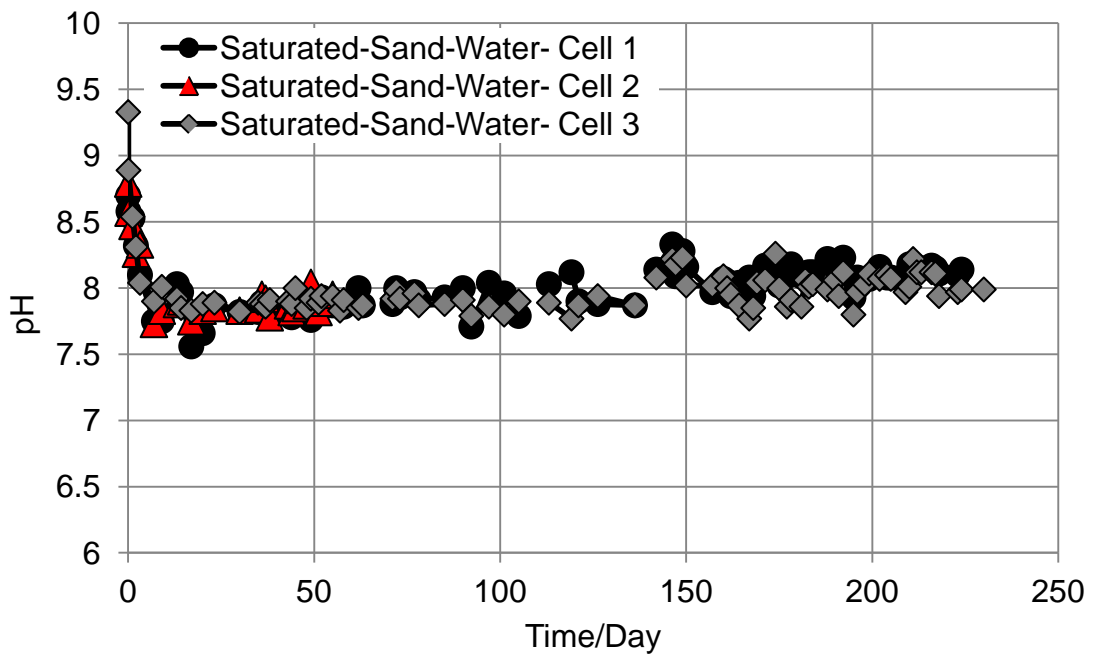


Figure 52: pH measured for triplicate specimens in saturated sand experiment.

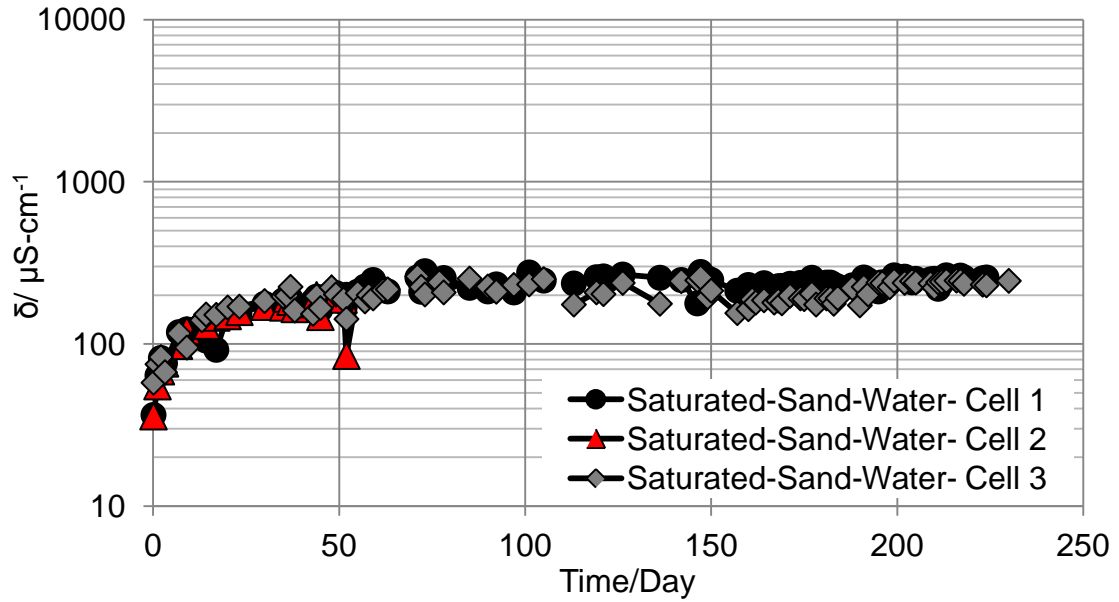


Figure 53: Conductivity measured for triplicate specimens in saturated sand experiment.

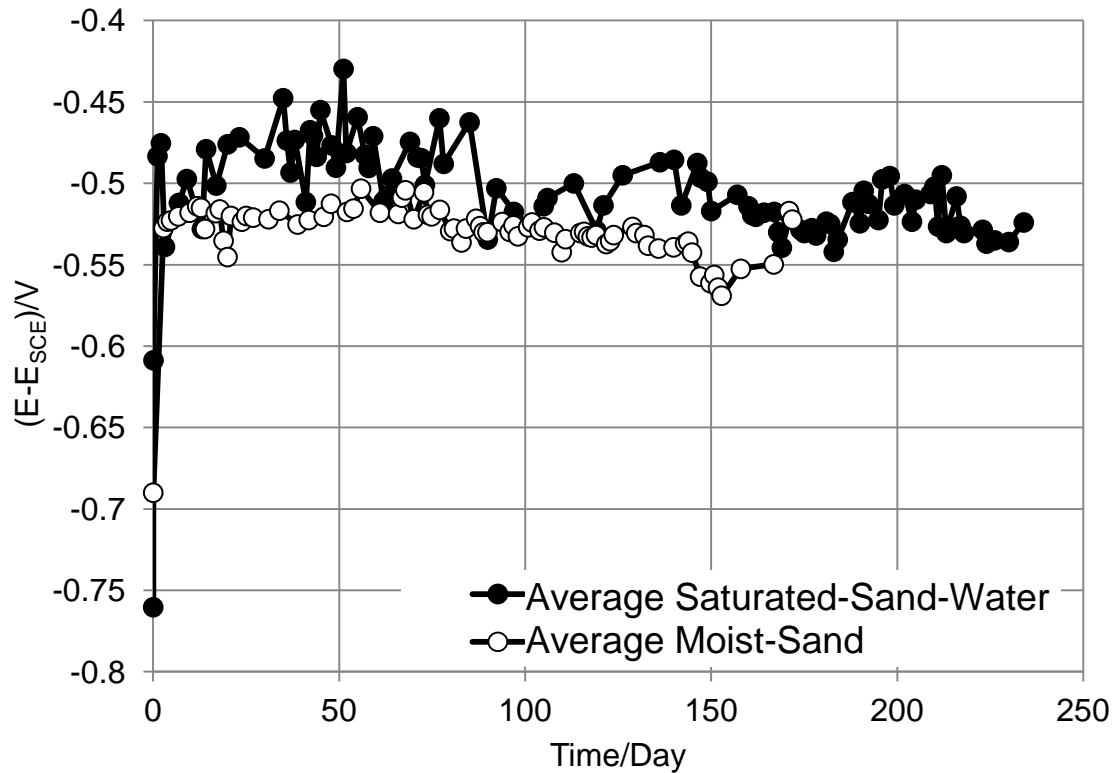


Figure 54: Average E_{OC} in saturated sand and moist sand experiments (Typical replicate variability: 20 mV (see explanation in Section 6.2.1).

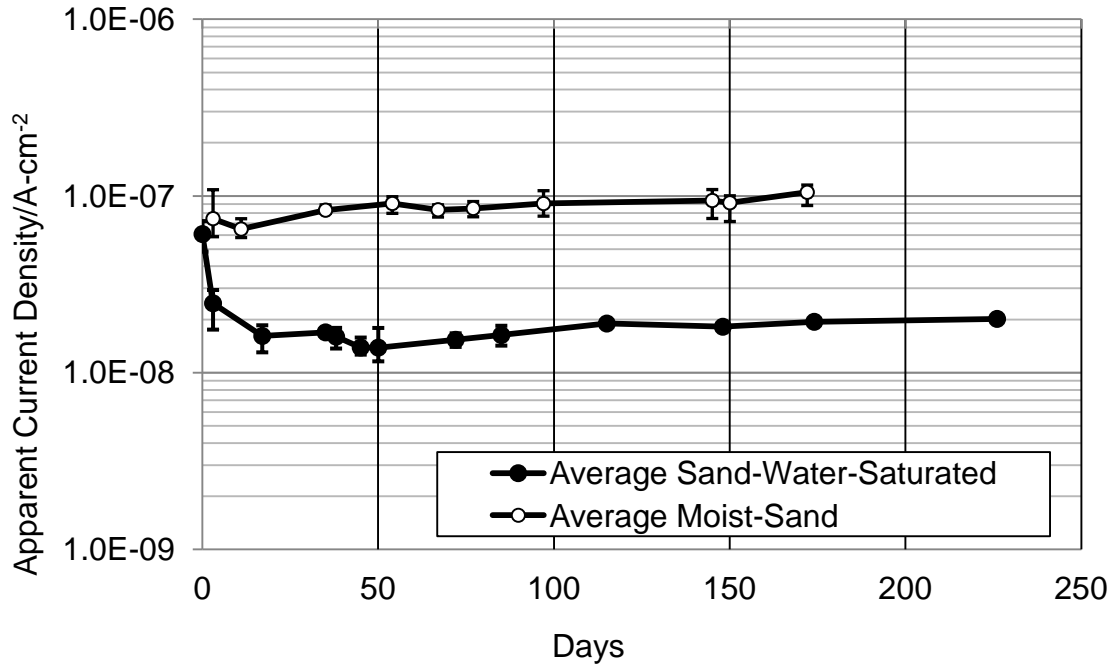


Figure 55: Apparent current densities (average and range) in saturated sand and moist sand experiment.

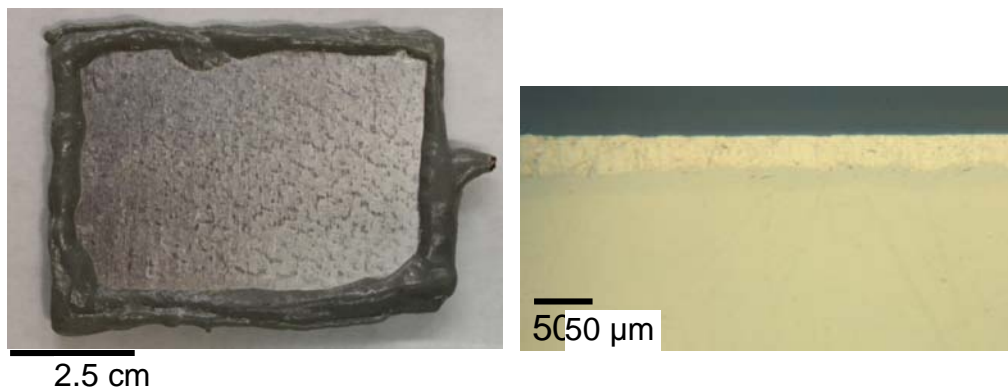


Figure 56: Bright appearance of specimen (Internal ID Code: Sandy 3) after 250 days of exposure to saturated-sand-water condition (Left). Metallographic cross-section are showing no significant aluminized layer consumption (Right).

7.2 Corrosion in Limestone Backfill

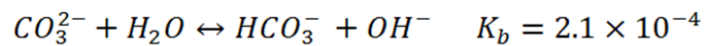
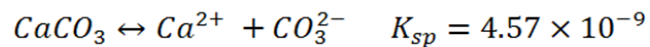
7.2.1 Introduction

Construction aggregates complying with ASTM C568-96 for bedding and backfill of pipes are often used to provide good structural support (Figure 22). Among these aggregates, crushed limestone (mostly CaCO_3) is frequently used for its availability (1.17 billion metric tons production in US in 2009) and cost effectiveness (Virta, 2009). The pipe in the Jacksonville SR 212 Mode B corrosion incident (Table 2) was placed in limestone, and, as noted in the introduction, complete penetration of the coating and mild steel substrate, starting from the soil side, took place in only 3 years at localized spots over a > 10 m long section of pipe. As detailed in chapter 3, a metallographic cross section of a field sample indicated widespread consumption of the outer aluminum layer, a less affected intermetallic inner layer, and severe undercutting attack of the steel substrate. Chemical tests of water in the pipe (in contact with external water through the wall perforations) showed insignificant amount of aggressive ions such as chloride and sulfate at the site.

It was speculated for Mode B that the dissolution of limestone backfill in the soil side water may have generated a high pH environment beyond the regime for stability of the aluminum passive film. A possible objection to that explanation is that water in contact with limestone in an open system equilibrated with atmospheric CO_2 develops only a mildly alkaline pH, typically ~8.3, (Snoeyink and Jenkins, 1980) that is virtually non-aggressive to a passive film on

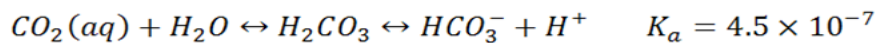
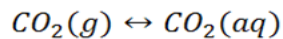
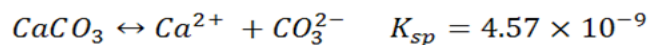
aluminum. However, previous studies on the use of limestone contactors for water treatment, (Letterman, 1983; Letterman et al., 1991) showed that dissolution of calcium carbonate in a closed system may increase the pH beyond 9.

The increase of pH when limestone reacts with water without having enough time to interact significantly with atmospheric CO₂ (that is in a nearly closed system) could be understood in terms of the following reactions:



Carbonate tends to be a weak base; therefore, it hydrolyses to form OH⁻ which results in an increase in pH (Harris, 2010).

In an open system, however, sustained interaction with CO₂ in the air leads to the formation of a weak acid; the generated H⁺ ions react with carbonate ions and form a lower pH solution compared to the closed system condition indicated above (Harris, 2010).



Computational chemical equilibrium model calculations (including the reactions indicated above as well as an expanded set of reactions) using the

program MINEQL⁺ (Schecher and McAvory, 2003) indicated that the pH for water at 25 °C in contact with solid calcium carbonate, but without effectively contact with atmospheric CO₂ (closed system), would be 9.91. If the water was assumed to be in equilibrium with atmospheric CO₂ before, but not after, contact with calcium carbonate the computed result was only slightly smaller, pH = 9.84, indicating that any atmospheric CO₂ present in the feed water before entering the cells should not be highly consequential.

In the case of AST2 pipes in limestone backfill, slowly flowing water (e.g. rain) that is not given enough time for equilibration could approach closed system conditions and result in significant corrosion. Therefore, the objective of this part of the work was to determine whether contact with limestone in flowing water could result in an elevated enough pH for the rapid corrosion of aluminized steel, such as that observed in the field, and to further understand the mechanism of that corrosion. The findings merit consideration to assist in updating specifications for the installation and use of backfill materials for aluminized steel culvert pipes.

7.2.2 Experimental Procedure

Laboratory experiments were conducted using 5 x 7.6 cm specimens (total exposed area of ~77 cm²) cut from as-received AST2 16-gage (1.6 mm thick) flat sheet stock. A contact wire with an insulating sheath was either spot welded or soldered to one of the edges. All the edges and wire connections were covered with two-component epoxy which was allowed to set for 24 hrs. Then, the

exposed metallic surfaces were degreased with ethanol and stored in a desiccator prior to immersion.

The immersion cells (Figure 57) were upright cylinders made of acrylic glass (10 cm internal diameter and 10 cm tall). The lower 8 cm contained ~0.8 kg of limestone crushed to a size between 1 cm and 3 cm, in which the specimen was embedded so its surface was in direct contact with multiple limestone particles. The composition of the rock used was tested in accordance with ASTM C1271 and confirmed to be ~97 wt% CaCO_3 (analysis conducted by X-ray Fluorescence spectrometry is shown in Appendix 4), comparable to commonly reported values for limestone (Boynton, 1980). Before being placed in the cells, the limestone particles were washed using the following procedure: About 1.5 Kg of rock particles were placed in a plastic strainer; tap water was run over the particles for about 15-20 minutes until the water was no longer murky. Then, particles were placed in another container which was filled with DI water. The container was shaken so that all the particles' surfaces were exposed to DI water. Then the DI water was drained. Washing and draining with DI water was repeated 3 to 5 times. Then, the particles were spread in a Pyrex tray to dry at room temperature overnight.

The cell feed water was commercially supplied distilled water, of resistivity > 50 k Ω -cm, representing rural rainwater (Sequeira and Lung, 1995). The feed water was held in a tank that allowed initial equilibration with atmospheric CO_2 . Peristaltic pumps fed that water into each cell at a rate of ~2 liter per day. The water entered the cell at the lower end, ran in contact with the fully immersed

specimen and the limestone and was removed through an opening level at the top of the limestone fill. The chosen flow rate was intended for dissolution of limestone while avoiding excessive introduction of additional CO₂ from air into the cell solution, approximating a post-dissolution closed system condition. A total of 14 specimens were tested in these conditions. The pH, conductivity, and open circuit potential (E_{OC}) measurements were taken daily. For six specimens (Coupon 1 to 6 listed in Table 5) an automated device (USB-1608FS MC Data Acquisition) was used to record the open circuit potential of the working electrodes against embedded titanium reference electrodes which also were manually calibrated against SCE. EIS test was not run for these six specimens; they were later used as undisturbed sources for metallographic coupon examinations.

For electrochemical measurements a titanium mesh with mixed metal oxide surface activation was placed around the inner wall of the cell to serve as a counter electrode. A similarly activated titanium rod 3 mm in diameter and 50 mm long was placed parallel to the specimen surface halfway to the counter electrode mesh, to serve as a low impedance temporary reference electrode (Castro, et al., 1996). It was periodically calibrated against a saturated calomel electrode (SCE). All potentials reported here are in the SCE scale. Electrochemical impedance spectroscopy (EIS) measurements were periodically obtained for 8 of the specimens (SP 1 to SP 8 listed in Table 5) at the E_{OC} with a Gamry™ Ref. 600 potentiostat in the frequency range 100 kHz to 10 mHz using sinusoidal signals of 10 mV rms amplitude. All tests were conducted at room

temperature. After exposure, the specimens were extracted and inspected for crevice corrosion. No crevice corrosion indications were observed in any of the cases. The tests and results for the first ~150 days are presented here.

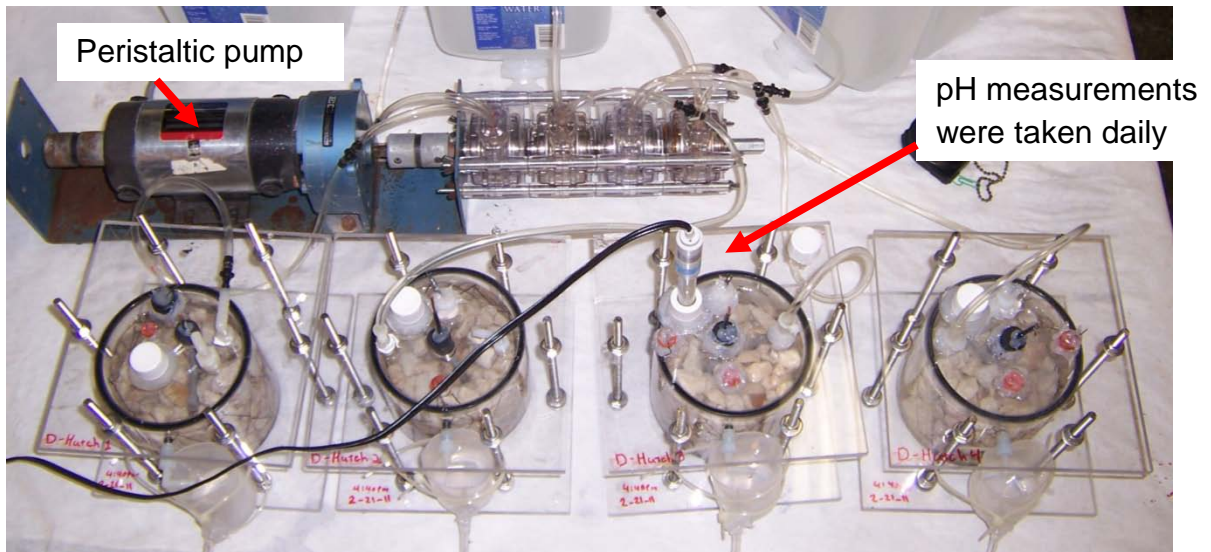
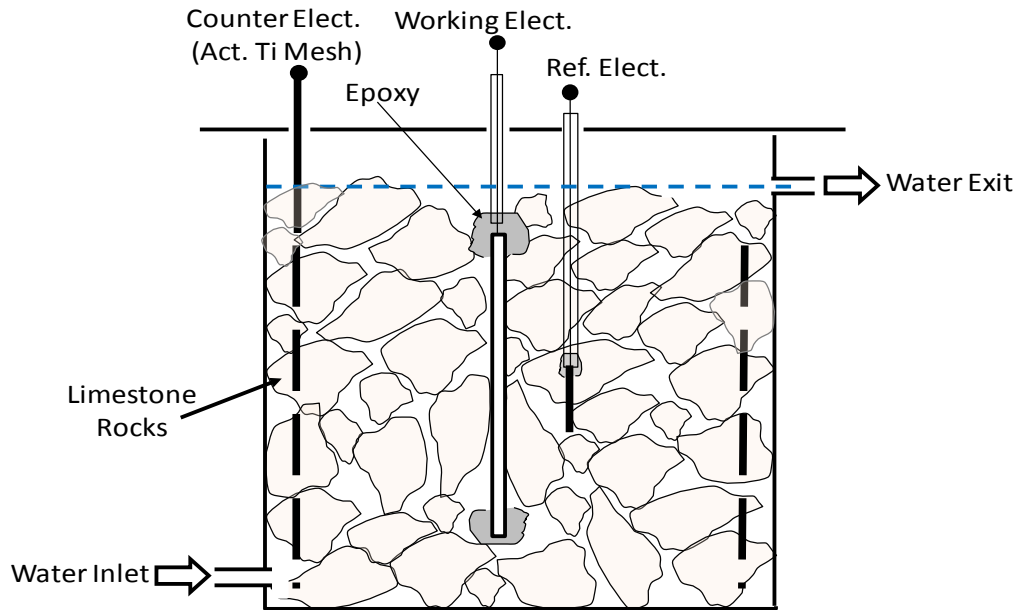


Figure 57: Limestone-cell configuration sketch (Top). Photo of four limestone cells and the peristaltic pump (Bottom).

Table 5: List of specimens for limestone experiment

	Specimen Number	Internal ID Code	Exposure Period Days	End of Stage I Period at Day	Critical Days	Symbol
Flowing Condition	SP1	Hutch 1	35	14	14-Nov	Empty Circle
	SP2	Hutch 2	27	10	none	Filled Circle
	SP3	Hutch 3	35	14	14	Empty Diamond
	SP4	Hutch 4	35	14	14	Filled Diamond
	SP5	Casta 1	71	10	9-10	Empty Square
	SP6	Casta 2	71	10	9-10	Filled Square
	SP7	S-hutch 1	155	15	14-15	Empty Triangle
	SP8	S-hutch 2	160	15	14-15	Filled Triangle
Non-Flowing (Control)	SP C1	Staglime 1A	137	NA	NA	X dash-line
	SP C2	Staglime 1B	137	NA	NA	X solid-line
	SP C3	Staglime 2A	137	NA	NA	Star dash-line
	SP C4	Staglime 2B	137	NA	NA	
Flowing Condition	Coupon 1	Pull Out 1	11	No EIS		
	Coupon 2	Pull Out 2	25			
	Coupon 3	Pull Out 3	45			
	Coupon 4	Pull Out 4	12			
	Coupon 5	Pull Out 5	46			
	Coupon 6	Pull Out 6	26			

Four Control specimens (SP C1 to C4 in Table 5) were exposed and tested in similar cells where the feed water was allowed to reach atmospheric equilibrium and was not replenished. In this case, for two of the specimens (SP C3 and SP C4), the limestone was pre-washed similarly to the procedure used for the flowing water cells.

For the other two specimens, (SP C1 and SP C2), the limestone were immersed in tap water (as opposed to running the tap water continuously for 15-

20 min) and shaken; the murky water was drained. Then the particles were washed similarly with DI water, and spread to dry at room temperature.

7.2.3 Results and Discussion

7.2.3.1 Solution pH

In the cells with no flowing water the pH decayed to < 8.5 after one day and reached terminal values ≤ 8.3 afterwards. These values approximate the expected condition, noted earlier, for water in contact with limestone and equilibrated with atmospheric CO_2 . As expected, non flowing water cells resulted a mild electrolyte condition where the average pH measured over 137 days of exposure for control specimens was about 8, and the average conductivity measured for the moderately washed limestone cells (SP C1 and SP C2) and thoroughly washed limestone were $\sim 1100 \mu\text{S}/\text{cm}^2$ and $\sim 200 \mu\text{S}/\text{cm}^2$ respectively. The pH evolution with time is shown in Figure 58 and is comparable to pH measurements recorded for sand-water experiments (section 7.1).

Notably, the pH within the flowing water cells was found to have a stable value of ~ 9.3 starting with the first day of exposure. The pH ~ 9.3 value in the flowing water cells indicated that the conditions tend to approximate those of a closed system, where the interaction with atmospheric CO_2 cannot keep pace with the dissolution of limestone in the flowing water.

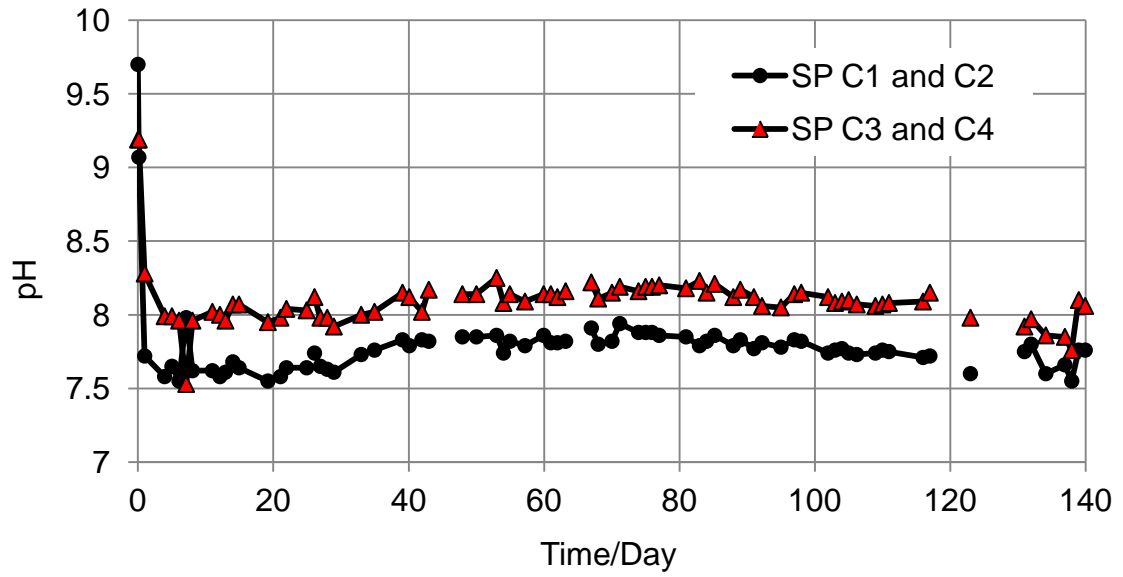


Figure 58: pH evolution of control specimens (non flowing condition) over time.

7.2.3.2 Corrosion Development - Physical Observations

Consistent with the resulting mild conditions, corrosion in the cells with no flowing water was relatively insignificant during the test period and details of those results are addressed later on.

In contrast, and as expected from the high pH solution, rapid corrosion of the aluminized coating took place in the flowing water cells. Direct observation of extracted specimens revealed that severe coating damage and surface discoloration took place starting after a short (about two weeks) exposure Figure 59. Metallographic and SEM observations confirmed severe loss of aluminized coating later on, as illustrated in Figure 60 A and B. As shown, the coating loss was rather generalized as opposed to sharply concentrated. The corrosion products consisted mainly of a dense, inner region that took the place of the consumed outer aluminized layer, and a usually thinner and more porous outer

region on top. In the inner layer of corrosion product, the Al-Fe intermetallic particles remained embedded and uncorroded, extending from the outer aluminized layer matrix, similar to the arrangement observed in the field sample (Figure 13).

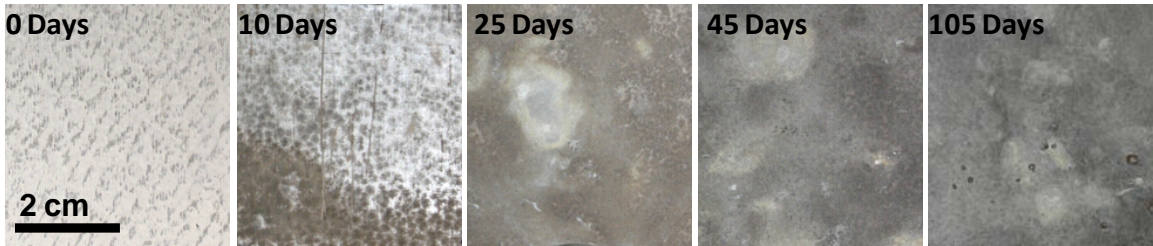


Figure 59: Surface discoloration over time.

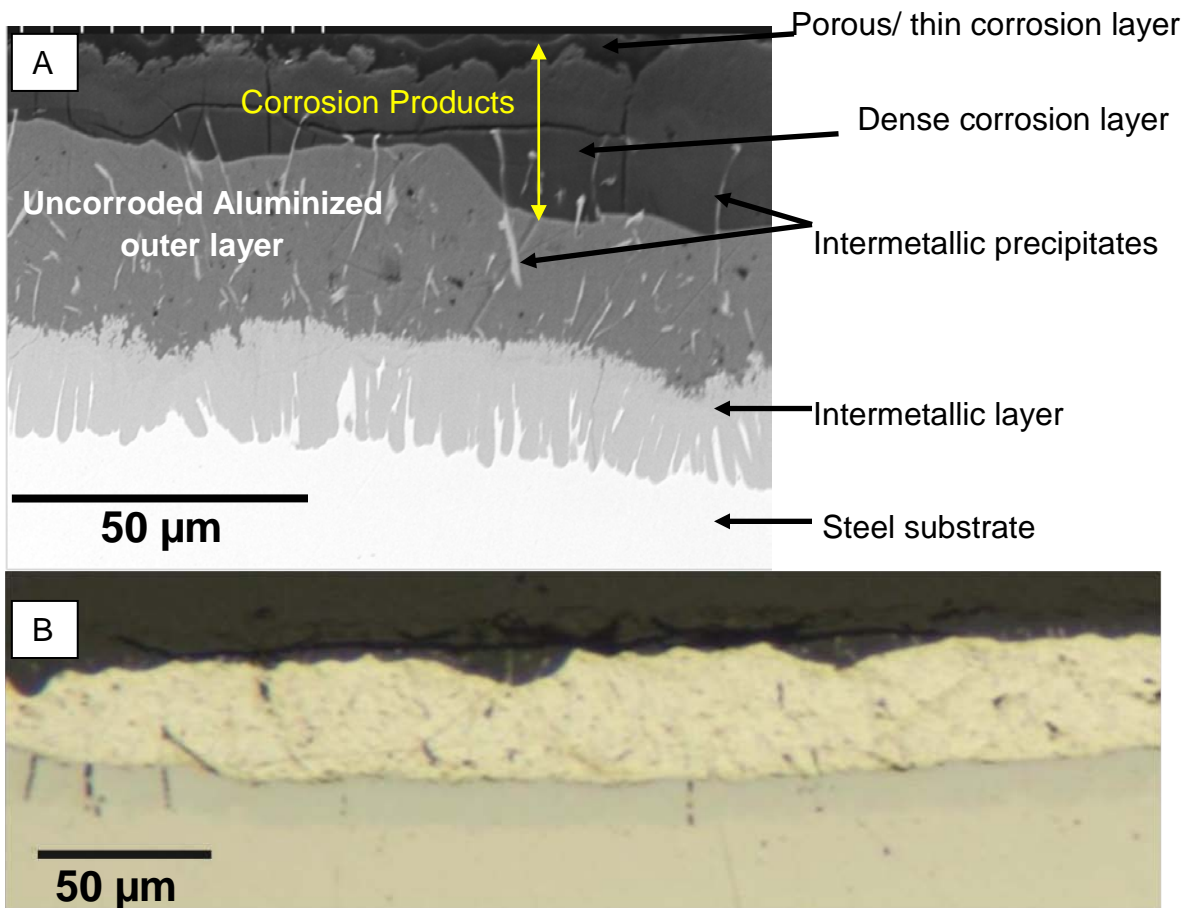


Figure 60: Coating condition after ~75 days exposure to flowing water (SP 3). SEM close up (A), Microscopic photo (B).

7.2.3.3 Corrosion Development - Electrochemical Behavior

The potentials values for non flowing water cells (Figure 61) approached a terminal value of ~ -500 mV_{SCE}, comparable to the values seen in the sand-water experiment (Section 7.1). Potential values significantly above ~ -900 mV_{SCE} are not uncommon for generally passive aluminum in non-aggressive waters (Sagüés, 1989). The EIS behavior for the control specimens is shown in the Appendix 2 (Figure A-4). To interpret the EIS data, and to estimate the corrosion rate for the control specimens, a similar approach to Stage I for flowing water condition, explained later, was used. Estimated corrosion rates were significantly smaller than those in the flowing water cells, as shown in comparative plots later on. These low corrosion rates maybe in agreement with observations of low corrosion rates in installations where limestone backfill was used but no failure occurred.

For flowing water cells, the E_{OC} initially decreased and reached a minimum (~ -1 V_{SCE}) indicative of highly active aluminum corrosion after about two weeks of exposure. Figure 61 shows the potential evolution for control specimens and the 8 specimens for which EIS measurements were frequently performed. The potential evolution of the 6 coupons that only were monitored for pH and potential (and later used as undisturbed sources for metallographic coupon examinations) are shown in Appendix 2 (Figure A-8). These potentials follow very similar pattern.

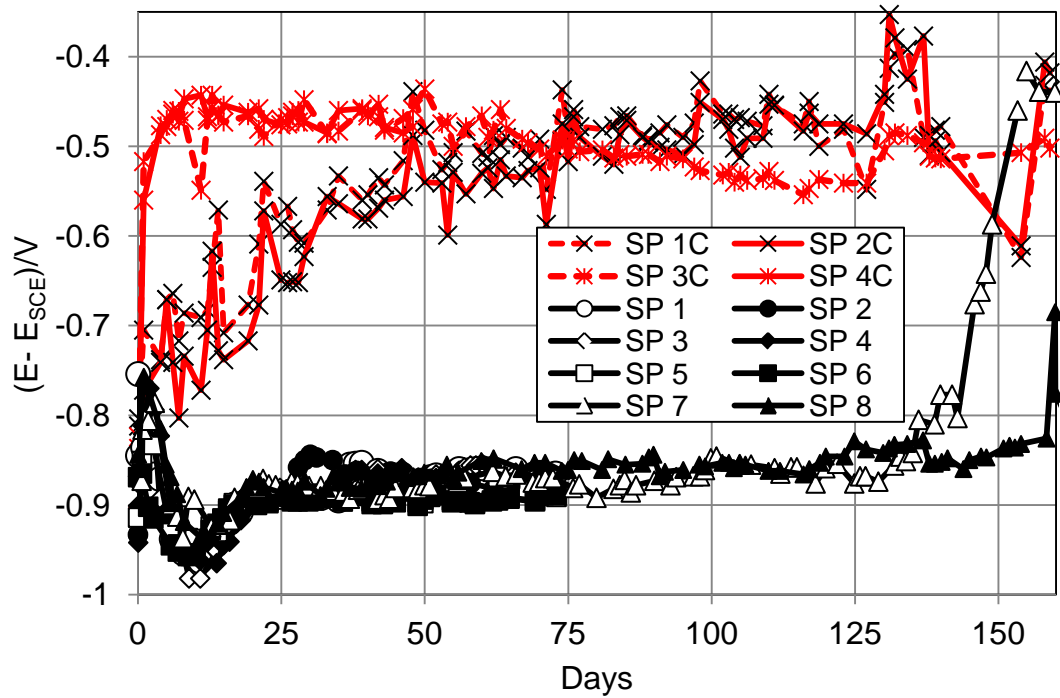


Figure 61: E_{OC} evolution for limestone specimens (data from multiple replicate specimens).

Typical EIS behavior is shown for different exposure times in Figure 63. The high frequency loop (100 Hz - 100 kHz), only shown for day 1, reflects water dielectric properties, apparent because of the high resistivity of the solution, and was omitted in subsequent analyses. The solution resistance is corresponded to the real value of the impedance at ~100 Hz. Variations with time of the solution resistance stemmed from minor changes in feed water composition and is not of consequence to the following analysis.

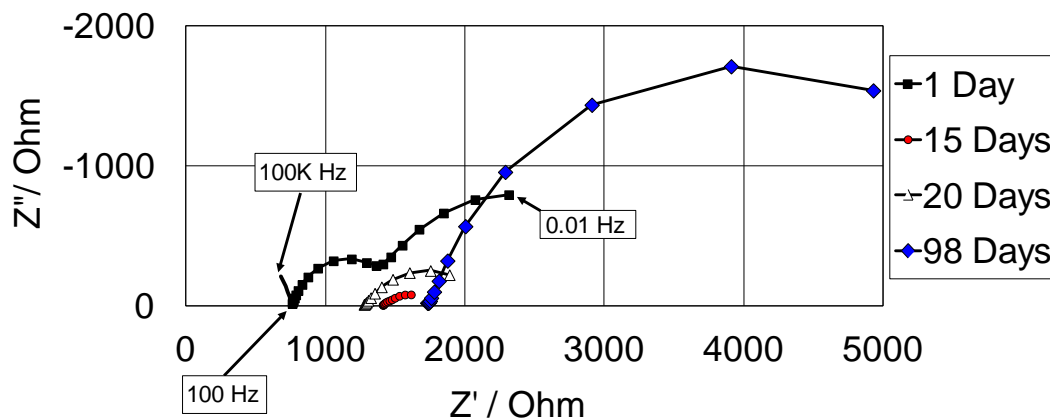


Figure 62: Typical EIS behavior of specimens exposed to limestone in cells with flowing water (shown for SP 8). [10 mHz (last datum) to 100 kHz; 3 data/decade; lines joining data are shown for clarity but do not represent a data fit]. Exposed area 77 cm².

The impedance behavior shown in Figure 62 and the Eoc evolution shown in Figure 61 make evident the presence of two Stages in the electrochemical evolution of the system. Stage I took place early in the exposure of the specimens (~two weeks) and is characterized by rapidly decreasing values of Eoc and an impedance that reaches minimum values after about two weeks. During most of Stage I, the impedance diagrams showed two clearly differentiated time constants (Figure 63).

Stage I is followed by a subsequent Stage II where the nominal polarization resistance gradually increased, and only one time constant is observed in impedance diagrams (Figure 64). The assumptions and the approach used to interpret the EIS results to obtain estimates of the corrosion rate prevalent in each of the stages are identified next.

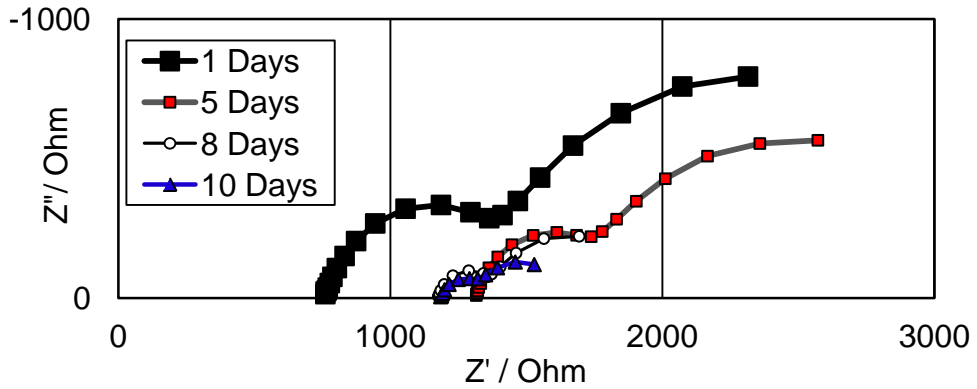


Figure 63: Stage I impedance behavior. Detailed for SP8. [10 mHz (last datum) to 100Hz; 3 data/decade]. Area = 77 cm². Lines joining data are shown for clarity but do not represent a data fit.

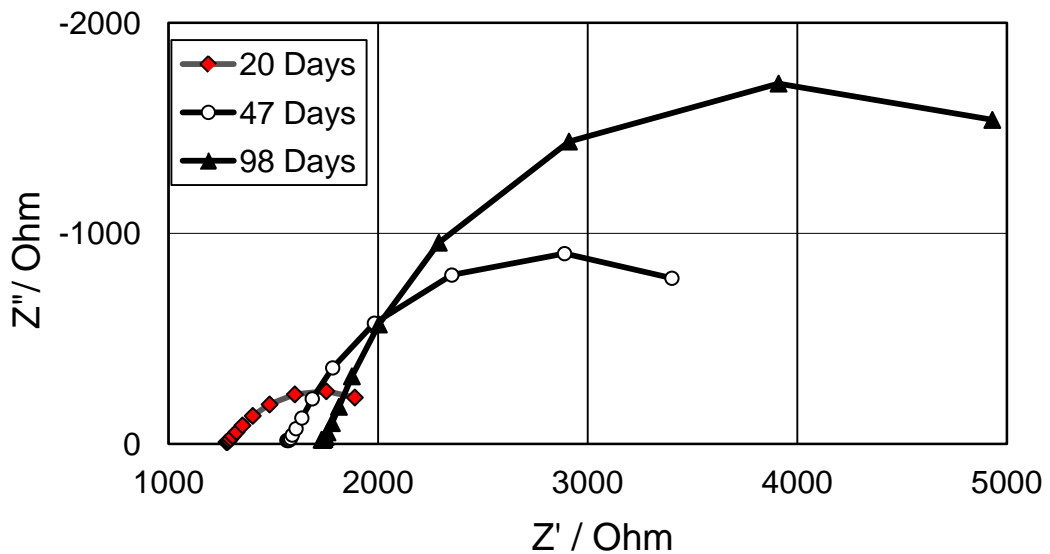


Figure 64: Stage II impedance behavior. Detailed for SP8. [10 mHz (last datum) to 100Hz; 3 data/decade]. Area = 77 cm². Lines joining data are shown for clarity but do not represent a data fit.

7.2.3.4 Interpreting EIS data: Control Specimens and Stage I of Flowing Water Condition

An equivalent analog circuit was used to fit the EIS data in Stage I for flowing water cells as well as the entire exposure times of non flowing water cells, and to find the parameters critical for calculation of corrosion rates. The chosen equivalent analog circuit was intended to account for the impedance response of the interfaces with the electrolyte of both the aluminum matrix and any intermetallic precipitate particles (where they are exposed at the outer surface) in the outer aluminized coating layer. The general idea for heuristically developing an equivalent circuit, where the impedances of different portions of the interface are assumed to be (at least on first approximation) independent of each other, is shown in Figure 65. The boxes on the left side of the figure indicate the individual impedances corresponding to the aluminum matrix and intermetallic particle interfaces, which are assumed to be acting as a simple parallel array. The solution resistance is shown as the simple ohmic resistor R_{sol} in series with the overall interfacial impedance, as a customarily used working approximation (Caseres, 2007).

Each of the aluminum matrix and precipitate interfacial impedances is in turn assumed to be represented by the parallel combination of independent impedances for the anodic and cathodic reactions, and the interfacial charge storage process (top and bottom right side of Figure 65). This assumption would require detailed proof in rigorous analysis, and it would likely not be justified if the products of the anodic reaction would participate in the cathodic reaction

(Sluyters, 1984). However, for mixed potential systems where the species involved in the anodic and cathodic reactions are different, the assumption is often justified (Sagüés and Kranc, 1996) and will be used here as a working hypothesis.

The interfacial charge storage process is assumed to be dominated on each interface by the capacitance of the respective passive film, represented by Constant Phase Elements (CPE). The admittance of the CPE is $Y_0 (j\omega)^{-n}$ where Y_0 is the pre-exponential admittance term, ω is the angular frequency, and $0 \leq n \leq 1$ (see section 1.2.3) with an expected n value not far from 1. In a more sophisticated analysis, the film capacitance could be considered to be in series with a double layer capacitance. However, the admittance of a double layer is expected to be significantly greater than that of the passive film, so in a series combination the latter would dominate and consequently the former is neglected here (Caseres, 2005).

The corrosion potential of the passive interfaces is assumed to be the combined mixed potential of the passive anodic dissolution processes and cathodic reactions such as oxygen reduction, taking place primarily on the intermetallic precipitates present at the surface. The rate of the anodic reaction on the aluminum matrix, or the precipitates, around the corrosion potential is assumed to be in the near-potential independent region characteristic of passive dissolution (Figure 5). Assuming that no other variables significantly affect the rate of the anodic reactions in that regime, the impedance for those components is then simply resistive and inversely proportional to the slope of the anodic curve

at that point. Hence the impedance was approximated (Figure 65) in both interfaces by a resistor, considered to have a very large value; the contribution of that component can be considered negligible on first approximation, given the parallel circuit configuration used.

The cathodic reactions on both interfaces at the system's mixed potential are expected to be significantly potential-dependent and possibly involving a complicated chain of processes, and are designated, for now, as rectangles.

Before further analysis, additional simplifications can be made by first noting that the rate of the cathodic reaction on the aluminum matrix can be negligible since the oxide film tends to develop an electron depletion zone as thick as the film itself (Caseres, 2007; Scully, 1993), and hence the associated impedance would be negligibly large in the parallel circuit configuration considered. Next, another simplification can be made by neglecting the (comparatively large) impedance of the interfacial capacitance of the intermetallic particle-electrolyte interface compared to that of the aluminum matrix, since the former covers only about 5% of the total surface as noted in Section 1.1. Consideration of all the simplifications leads to the circuit in Figure 66.

The circuit in Figure 67 implies recognition that intermetallic precipitates' surfaces are considered to be the primary site of the cathodic reaction for aluminized steel (Nisancioglu, 1990; Caseres, 2007). In an attempt to explain the presence of two time constants in the impedance diagram for Stage 1, it is proposed that the cathodic reaction taking place on these precipitates occurs in

two steps: first a species A that undergoes the cathodic reaction (e.g. O_2 g) reacts on the surface to generate an intermediate compound, Species B (e.g. hydrogenperoxide). This reaction takes place on some area fraction X of the intermetallic surface in contact with the electrolyte. It is assumed that species B deposits on the remaining area fraction (1-X). Species B then reacts to form a final compound C (e.g. $4OH^-$) that leaves the surface.

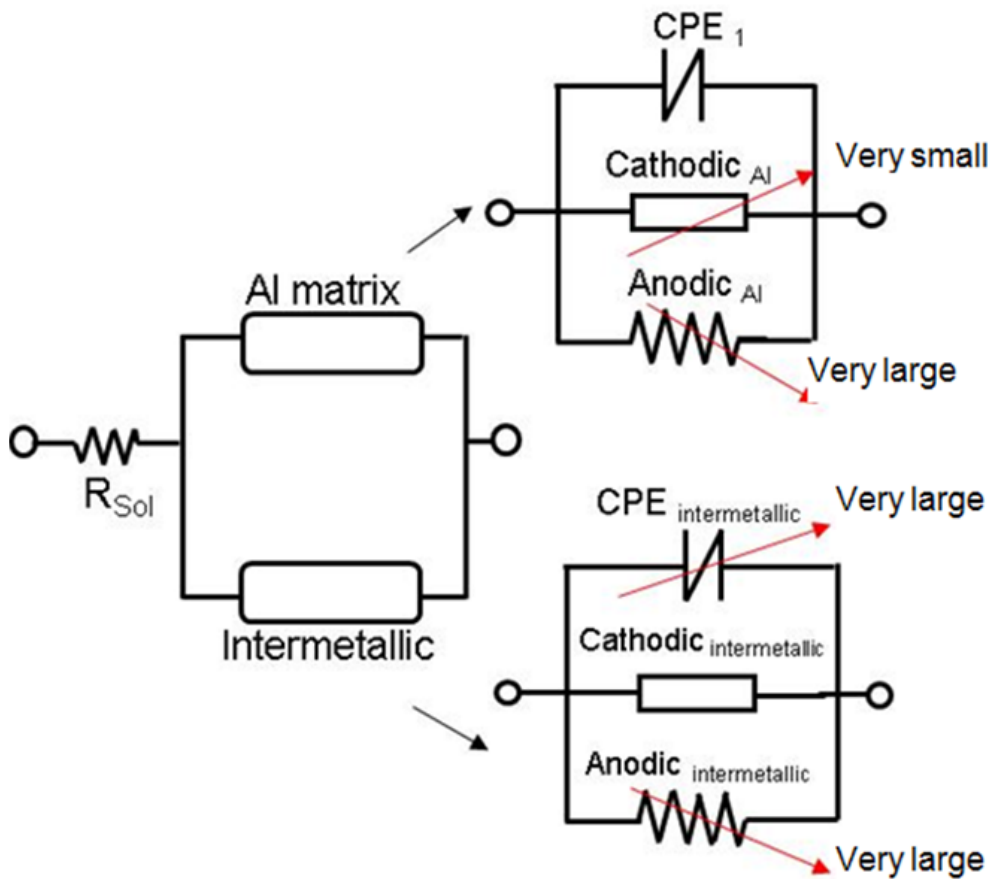


Figure 65: General concepts in developing an analog equivalent circuit for Stage I behavior.

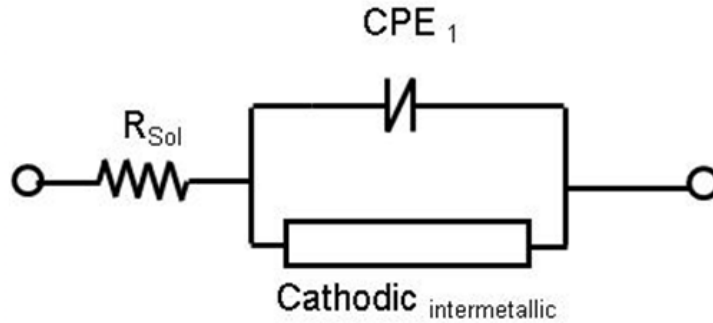


Figure 66: Simplification of preliminary circuit.

As an illustration, a two-step reduction reaction for oxygen is shown below (Genies et al., 2003):



Each reaction has its Tafel slope (β_1 and β_2). In a two step reaction, the overall rate of cathodic reaction depends on the rate of each step (specific to the portion of the surface on which the step takes place), and also depends on the potential (Epelboin and Keddam, 1970; Caseres, 2007; Montella, 2001).

If the potential of the system (assuming it is in a steady state condition) was suddenly altered, the rate of each reaction would experience a sudden change followed by relaxation toward a final new steady state value. The sudden change reflects the effect of the new potential value in the rate of the each reaction in its respective area fraction, but before the area fractions have a chance to evolve toward their new steady state values. The slow relaxation

reflects the establishment of new area fractions. Immediate responses can be associated with the high frequency limit impedance behavior of the system (corresponding to the value of the charge transfer resistance), while the new steady state condition is related to the low frequency limit of the impedance (corresponding to the polarization resistance). These concepts have been analyzed in terms of impedance response of multi-step reactions (Epelboin and Keddam, 1970; Macdonald and McKubre, 1982) showing that the Faradaic impedance behavior can be expressed in terms of the equivalent circuit in Figure 67. For immediate potential changes (high frequencies), the impedance of the circuit is given by Resistor R_1 , since C_2 acts as a short circuit at high frequencies. At the new steady state (essentially zero frequency) C_2 corresponds to an open circuit, and the overall impedance is the sum of R_1 and R_2 . Thus, R_1 is the value of the charge transfer resistance and R_1+R_2 the value of the polarization resistance. C_2 , together with R_2 , determine the characteristic time constant of the relaxation process in between both conditions. As indicated in the above literature sources, the value of R_1 is given by (Epelboin and Keddam, 1970, Macdonald and McKubre, 1982):

$$R_1 = \frac{n+m}{(n * 2.303 / \beta_1 + m * 2.303 / \beta_2)} \cdot \frac{1}{I_c} \quad \text{Eq (9)}$$

where:

n, m , are the number of electrons consumed in each reaction (for Reaction 4 and 5, $n = m = 2$).

I_c (treated here as a positive number) is the total cathodic current taking place on the intermetallic precipitate surfaces.

β_1 and β_2 are the Tafel slopes for Reaction M and N shown above.

The typical Tafel slope values for oxygen reduction reactions in alkaline environments for noble metals such as platinum are in the order of 60 mV/dec at low current densities $<10^{-4}$ A/cm² and 120 mV/dec at higher current densities $>10^{-4}$ A/cm² (Genies et al., 2003). However the Tafel slopes reported for less noble metals, as may be the case of the intermetallic precipitates, can be significantly greater e.g. in the order of 75 to 200 mV/dec (Fabjan et al., 1989). For the purpose of this analysis a Tafel slope value of 120 mV/dec was assumed, which is also a value customarily used to approximate calculations when the actual values of Tafel slopes are unknown (Jones, 1996, p.84). Inserting the assumed parameter values Eq (9) reduces to:

$$R_1 = 0.052 \text{ V} / I_c \quad \text{Eq (10)}$$

Since, under open circuit steady state conditions, the total cathodic current is equal to the total anodic current, the value $I_{\text{corr}} = 0.052\text{V} / R_1$ provides an estimate of the anodic reaction current, effectively the corrosion current of the system under the above assumptions (that the cathodic reaction only takes place at intermetallic precipitates and consists of two reaction steps). If the anodic reaction were uniformly distributed over the specimen surface, the corresponding corrosion current density would be given by $i_{\text{corr}} = I_{\text{corr}} / A$ where $A = 77 \text{ cm}^2$. This issue is addressed in more detail later on.

It is noted that the value of R_2 is a complicated function of the system parameters and not directly associated with the overall rate of the cathodic reaction. Hence, the value of R_2 will not be used to estimate the corrosion rate here.

In actual systems the idealized conditions leading the circuit in Figure 67 are not completely met, and the impedance behavior is better matched by using a CPE (CPE_2) instead of the ideal capacitor C_2 . Introduced in Figure 67, the equivalent circuit of the cathodic impedance just discussed, the overall circuit for the assumed conditions is shown in Figure 68.

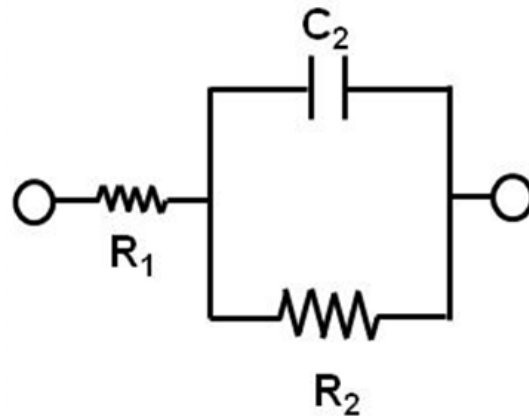


Figure 67: Equivalent analog model for impedance response of a two step reaction system.

This equivalent circuit provides a good fit for the data of Stage I as well as the entire exposure time for non flowing cells; examples of the fit quality are illustrated in Appendix 2. Figures 69 and 70 summarize the evolution of the CPE_1 , n and R_1 parameters during Stage I for flowing water condition.

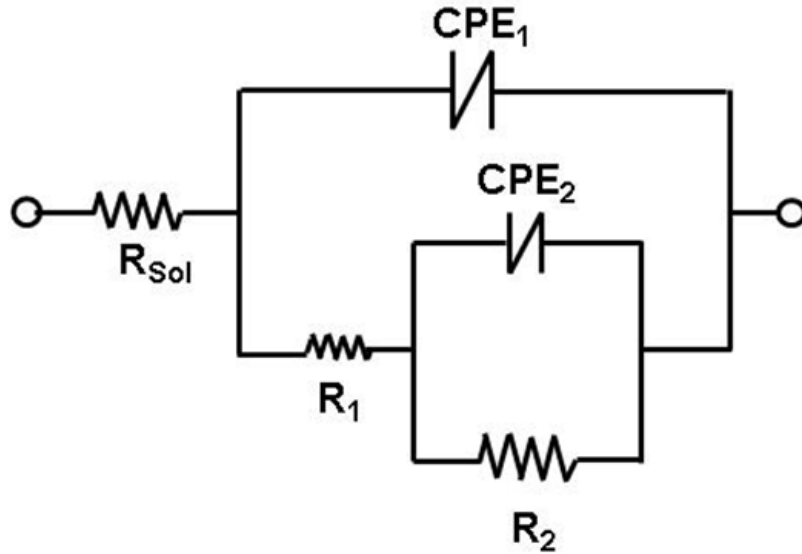


Figure 68: Final analog equivalent circuit to interpret the EIS data for Stage I.

For all specimens during most of Stage I, the n value obtained for CPE_1 was typically ~ 0.9 (approaching ideally capacitive behavior with nominal capacitance $C \sim Y_0 \text{ sec}^{(1-n)}$). Nominal capacitance values for this CPE were in the order of $4 \mu\text{F cm}^{-2}$ initially and increased with time. Such values are consistent with those expected for the capacitance of naturally formed aluminum passive films (Scully, 1993; Bessone et al., 1992). An estimate of the nominal thickness (d) of the film during Stage I was made using:

$$d = \epsilon_0 * \epsilon * A / C \quad \text{Eq (11)}$$

where:

ϵ is the dielectric constant of the passive film (estimated to be ~ 8) (Scully, 1993),

ϵ_0 is the permittivity of free space ($8.85 \times 10^{-14} \text{ F/cm}$),

A is the area of the metal coating ($\sim 77\text{cm}^2$)

C was the capacitance value obtained from CPE_1 .

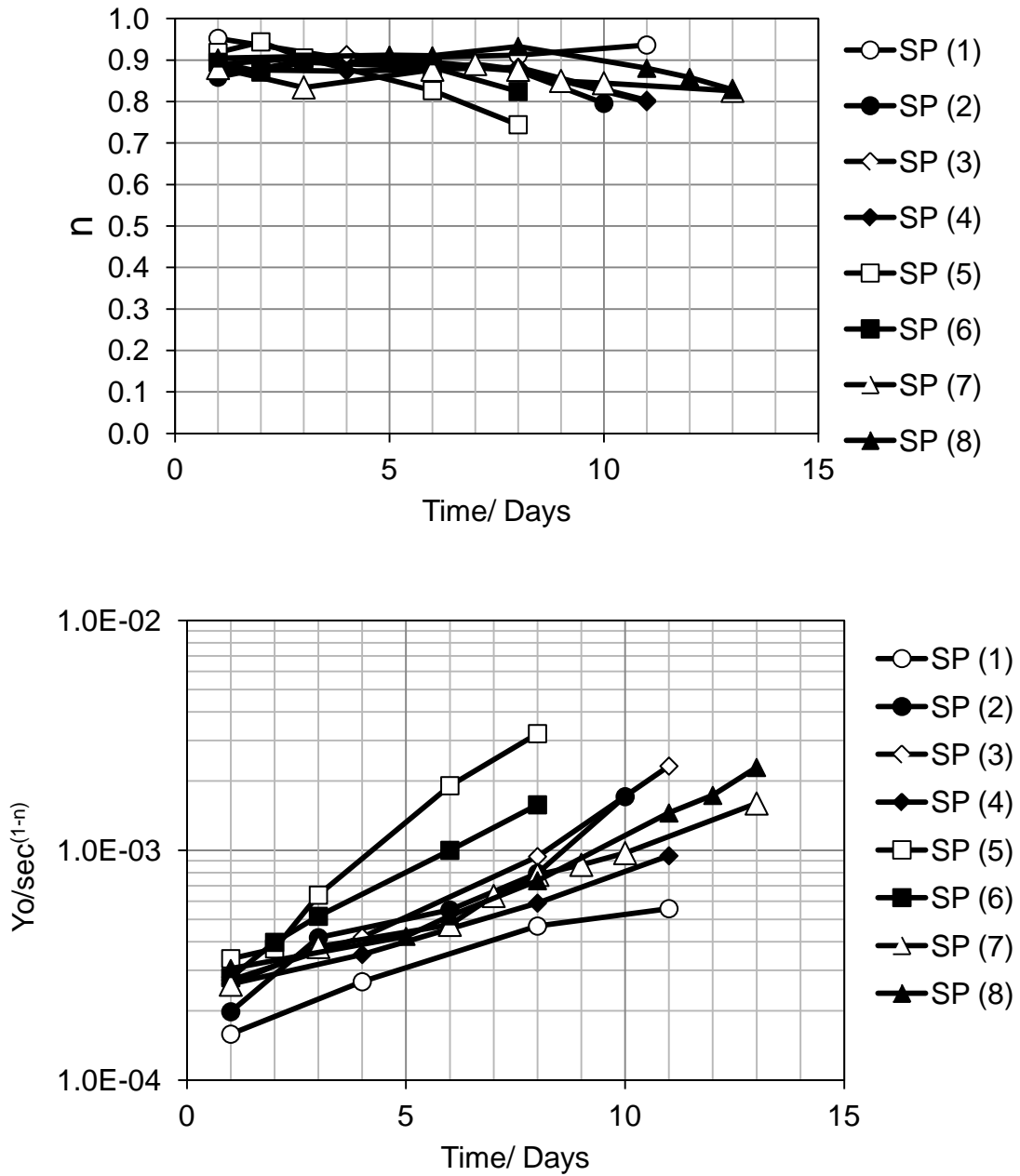


Figure 69: The evolution of the CPE_1 parameters Y_0 and n during Stage I.

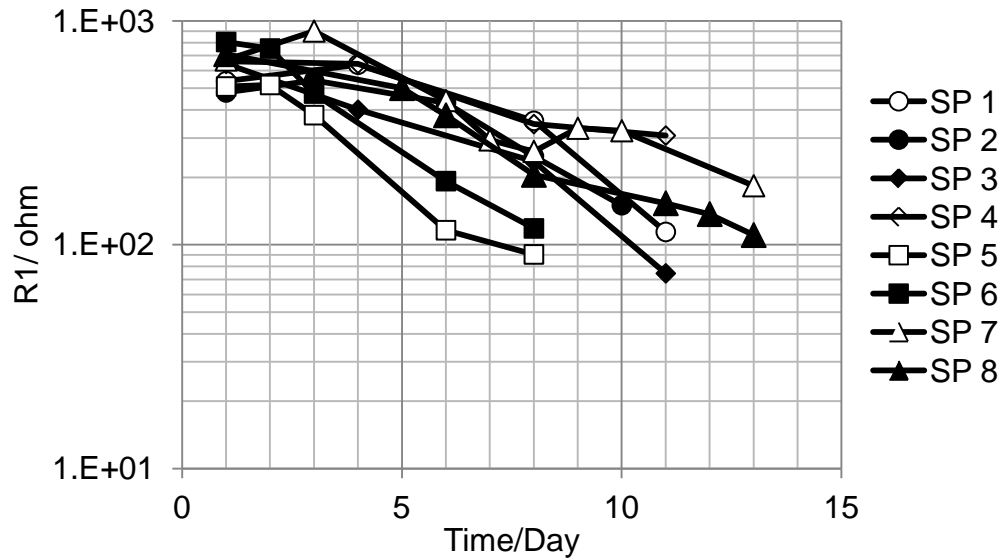


Figure 70: Evolution of R_1 during Stage I for all specimens tested.

The nominal film thickness is plotted as a function of time in Figure 71 for multiple replicate specimens. The initial thicknesses were about 2-3 nm thick, comparable to values reported in previous studies (Scully, 1993; Bessone et al., 1992). The values decreased with time and reached atomic dimensions (e.g. ~0.2 nm) after about 2 weeks. That condition may be viewed as being indicative of full consumption of the film at that time. Such interpretation is consistent with the concurrent strong drop in nominal polarization values (onset of severe corrosion), lowered E_{oc} (approaching the potential of actively corroding aluminum), and the appearance of a light grey shade on the surface of the specimens at the end of Stage I.

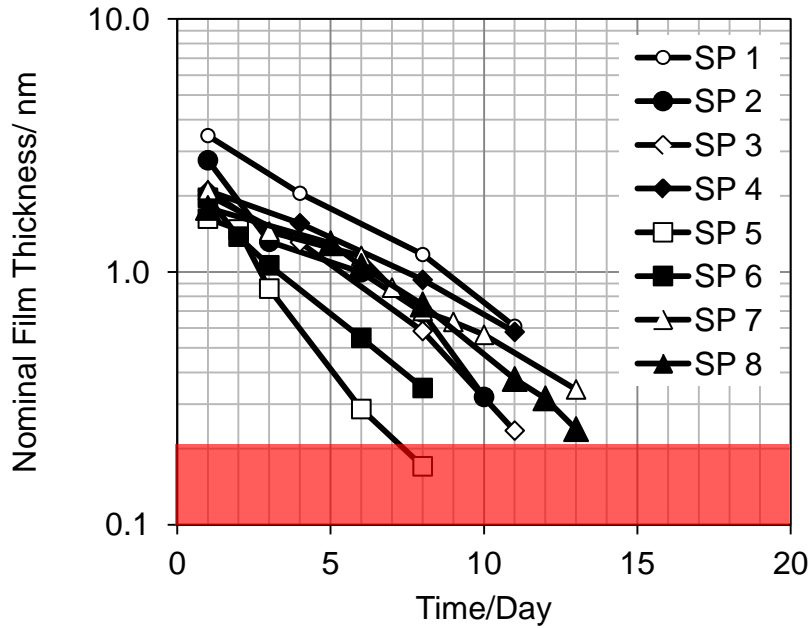


Figure 71: Nominal film thickness during Stage I. Data from multiple replicate specimens. Red band indicates values approaching typical atomic dimensions.

Around the transition between Stages I and II, for a short period (~0-5 days, somewhat different for each specimen), the EIS impedance diagrams did not show clearly differentiated semicircles. The fit using the equivalent circuit in Figure 68 was affected by considerable uncertainty when applied to the EIS data obtained during the transition period; therefore, an alternative rough estimate of the corrosion rate for the transition period was conducted as follows. First, a nominal polarization resistance, R_{pn} , was defined for all tests during Stage I by subtracting the solution resistance from the real part of impedance at 10 mHz. Then, the ratio of $r = R_1 / R_{pn}$ was calculated for each specimen for each EIS experiment in Stage I that was conducted before the transition period. A linear regression of the value of r as a function of time was performed for each specimen, yielding slope and intercept values for the specimen. The trend lines

had comparable parameters, so an average slope (0.00135 / day) and an average intersection (0.376) were calculated and used as master parameters for the group. The master parameters were then applied to the time corresponding to each of the transition period experiments that provided an extrapolated value of r for each instance. Then, the R_{pn} values obtained during the transition period were multiplied by the extrapolated r value to obtain an estimate of R_1 . That value was then used to obtain the estimate of the corrosion current using $I_{corr} = 0.052V / R_1$ as explained previously.

7.2.3.5 Interpreting EIS Data: Stage II

The impedance diagrams obtained during Stage II, (Figure 64), differed from those in Stage I. Starting shortly after the onset of Stage II and, from then on, there was typically only one loop, consisting of a moderately depressed semicircle. The impedance spectrum, concentrating again on frequencies below ~100 Hz for the reasons stated in the Stage I discussion, could be closely approximated by the response of a simple parallel combination of a CPE (CPE_3) and a resistor (R_3) in series with an ohmic solution resistance element (Figure 72).

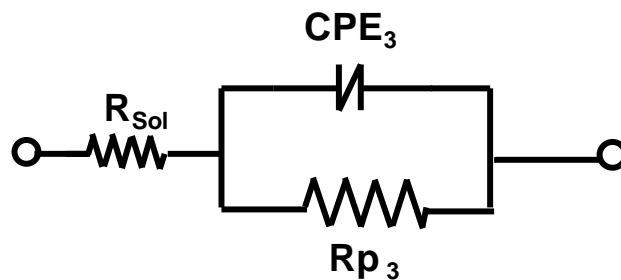


Figure 72: Analog equivalent circuit to interpret the EIS data for Stage I.

Figure 73 and 74 exemplify, with data from one of the specimens, the typical evolution of the CPE_3 , n , and Rp_3 parameters during Stage II.

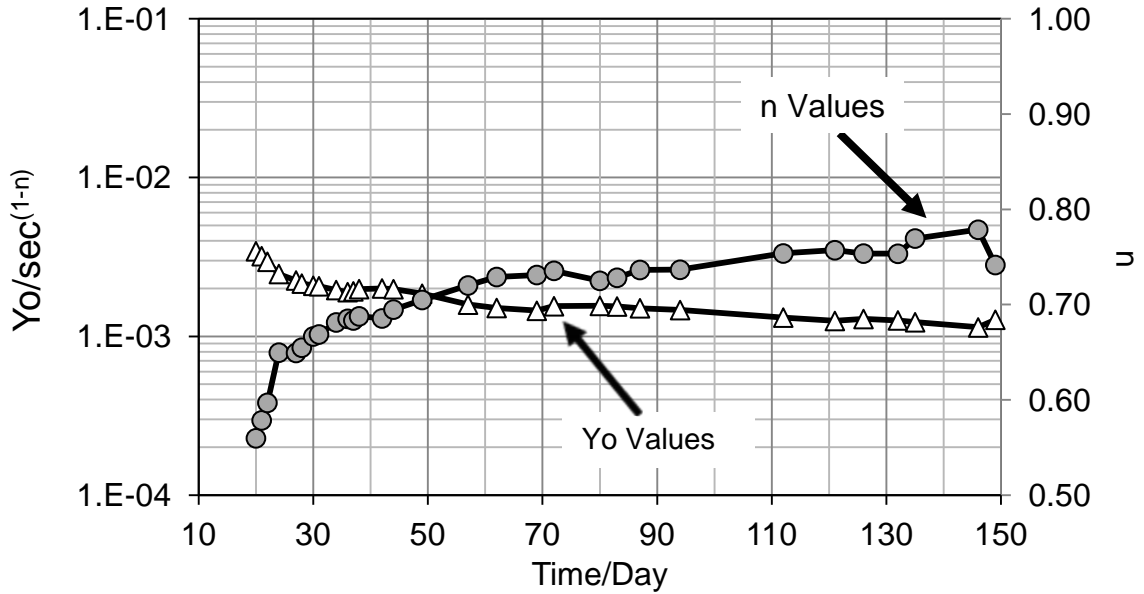


Figure 73: Typical evolution of the CPE_3 (triangles) and n (circles) during Stage II (shown for SP 7).

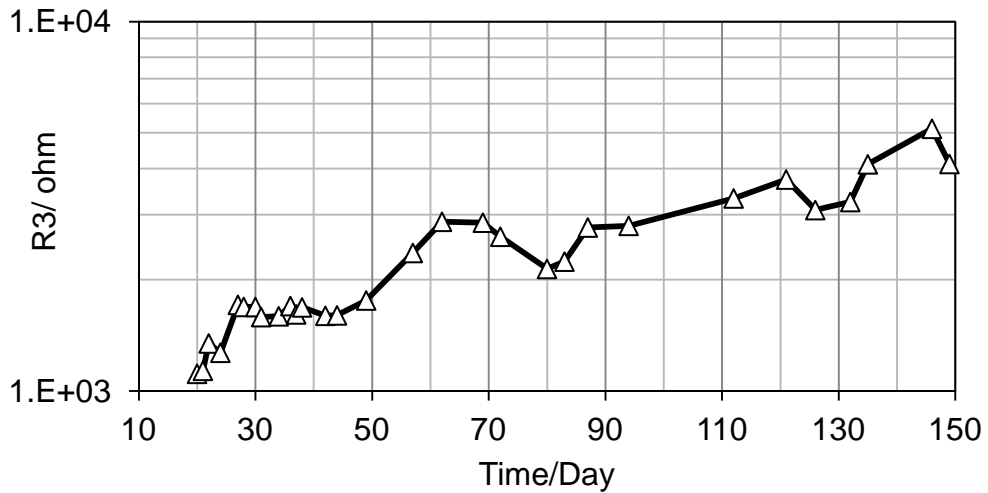


Figure 74: Typical evolution of Rp_3 during Stage II (shown for SP 7).

The relatively large value of CPE_3 and moderate deviation from ideality (n_3 typically ~ 0.7) obtained from the above analysis were comparable to those often observed for the surface of metals undergoing corrosion in the active state (Caseres, 2007). It will be assumed that the value of R_{p3} represents the polarization resistance of an actively corroding electrode. Following the arguments explained for Stage I, R_{p3} can be envisioned as being the parallel combination of two impedance elements, related to the anodic and cathodic processes respectively.

For reasons explained next, it will be further assumed that one of the reactions is subject to near complete diffusional control which would result in a very high impedance value at the low frequencies associated with the observed loop. Hence, the contribution of that element can be ignored in the following. Given that the spectrum contains only one identifiable loop, the other reaction can then be speculatively associated with a simple one-step, activation limited reaction with polarization resistance (Caseres, 2007). Using R_{p3} values and assuming Tafel slope values of 120 mV/dec (Jones, 1996, p.84), the corrosion current (assuming that the reaction is uniformly distributed over the specimen's surface) at this stage was calculated by $I_{corr} = 0.052V / R_{p3}$. Estimated corrosion current densities for R_{p3} values shown in Figure 74 were calculated and shown in Figure 75. The figure shows that the apparent corrosion rate decreases with time, typical of all the specimens, after the onset of Stage II.

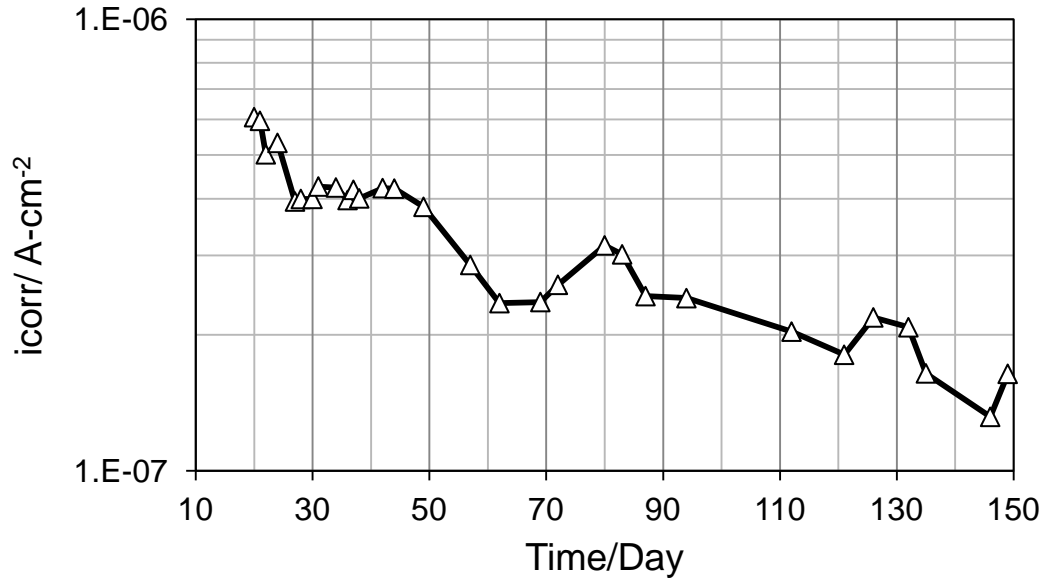


Figure 75: Typical evolution of i_{corr} during Stage II (shown for SP 7).

Estimated corrosion current densities for all specimens exposed to the flowing water condition, as well as for control specimens, are shown in Figure 76. This graph shows the increasing trend of estimated corrosion density for Stage I and decreasing trend for Stage II for flowing water cells. The results for the control specimens are shown in red lines; as noted earlier, these current densities are significantly lower than those estimated for the flowing water condition.

As shown by the metallographic evidence, as aluminum corrodes, the corrosion products are retained in the form of an increasingly deep penetration layer that, while not highly protective, may act as an increasingly thick barrier to the diffusion of one of the reacting species. The subsequent gradual decrease in apparent corrosion current density during Stage II may be interpreted as being

the result of the growth of that corrosion product layer. If, on first approximation, the rate of corrosion is inversely proportional to the thickness of the growing layer, then the rate would decay proportionally to the square root of time (Stoudt et al., 1995).

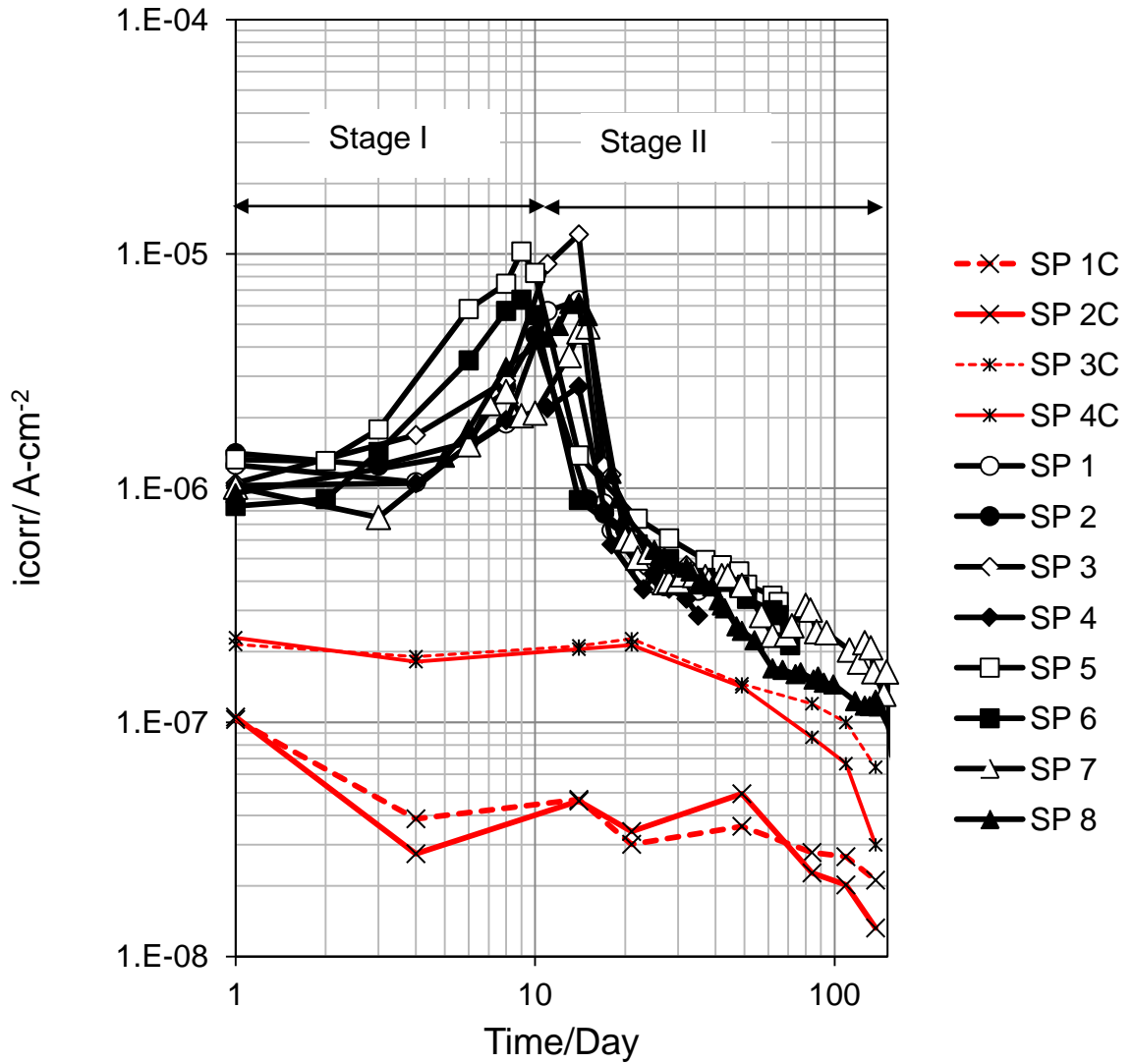


Figure 76: Estimated corrosion current density as a function of time for both stages.

In an attempt to explain that hypothesis, one could imagine a corrosion film that grows inward from the surface of a metal with thickness h that increases with time. As noted earlier, with the exception of a relatively thin outer deposit, the penetration did not appear to be in the form of expansive corrosion products so the thickness of the corrosion product layer is on first approximation equal to the thickness of metal lost. The corrosion rate by definition is the change in thickness h with time, dh/dt , which, under a diffusional limitation hypothesis, is proportional to the inverse of the film thickness (since for thicker film the transport of the species involved in the corrosion process would be slower). Therefore:

$$dh / dt = K / h \quad \text{Eq (12)}$$

K is a constant expected to be proportional to the diffusivity of the species involved. Equation (12) can be rewritten as:

$$h * dh = K * dt \quad \text{Eq (13)}$$

Integration was done on both sides of Eq (13):

$$\int_{h_i}^H h * dh = \int_{t_i}^T K * dt \quad \text{Eq (14)}$$

H and T are the final cumulative thickness and exposure time respectively and t_i is the time at the beginning of Stage II. Integration results in Eq (15):

$$(H^2 - h_i^2) = 2K (T - t_i) \quad \text{Eq (15)}$$

For the case where $h_i = 0$ and $t_i = 0$, Eq (15) simplifies to:

$$H^2 = 2KT \quad \text{Eq (16)}$$

By taking the square root of both sides:

$$H = (2KT)^{0.5} \quad \text{Eq (17)}$$

Replacing H for above equation into Eq (12) and for simplicity we introduce another constant $K' = (K/2)^{0.5}$:

$$dh / dt = K' * t^{-0.5} \quad \text{Eq (18)}$$

Therefore, for this case, the corrosion rate is simply proportional to the inverse of the square root of time.

Taking the logarithm of both sides (with appropriate normalization for units):

$$\log (dh / dt) = 0.5 \log (K') - 0.5 \log (t) \quad \text{Eq (19)}$$

where $0.5 \log (K')$ is a constant, then Eq (19) can be rewritten as:

$$\log (dh / dt) = -0.5 \log (t) + C \quad \text{Eq (20)}$$

Therefore, a log-log graph of corrosion rate vs. time should illustrate a -0.5 slope. Likewise, a log-log graph of Eq (16) should show a slope of 1. When corrosion rate for Stage II was plotted vs. time assigning a value $t=0$ and $h=0$ for the start from Stage II, it was noticed that the slopes were much greater than 0.5. Likewise, log-log graphs of H^2 vs T showed a slope significantly greater than 1. Those observations were interpreted as an indication that the initial thickness was not zero at the beginning of Stage II. Hence it is proposed that before the onset of Stage II, while the oxide film still remained on much of the surface, some non-uniform corrosion was taking place that resulted eventually in the presence of a small but significant corrosion product thickness on some regions of the

specimen surface. Such occurrence can be exemplified by the condition shown in Figure 59, at day 10 (near the end of but still during Stage I). Therefore, going back to Eq (15), and taking the logarithm of both sides:

$$\log (H^2-h_i^2) = \log [2K (T-t_i)] \quad \text{Eq (21)}$$

Which can be simplified as:

$$\log (H^2-h_i^2) = \log (T-t_i) + \log 2K \quad \text{Eq (22)}$$

Eq (22) indicates that there should be a slope of unity for the log-log scale graph of accumulated thickness loss as a function of the time elapsed from the beginning of stage II. The accumulated thickness loss was calculated based on the corrosion current density values in Figure 76 and by Faradaic conversion, Eq (1), (for aluminum anodic reaction: $n=+3$, $M= 26.98$ g/mol and density of 2.69 g/cm³) and accounted for the time step that for which these corrosion rates took place.

The resulting combined graph for the data from all available specimens up to 150 days of exposure is presented in Figure 77. The overall slope closely approached the ideal value of 1, in support of the proposed scenario. This outcome was part of the reason for postulating earlier that one of the corrosion reactions was subject to diffusional control in interpreting the impedance data.

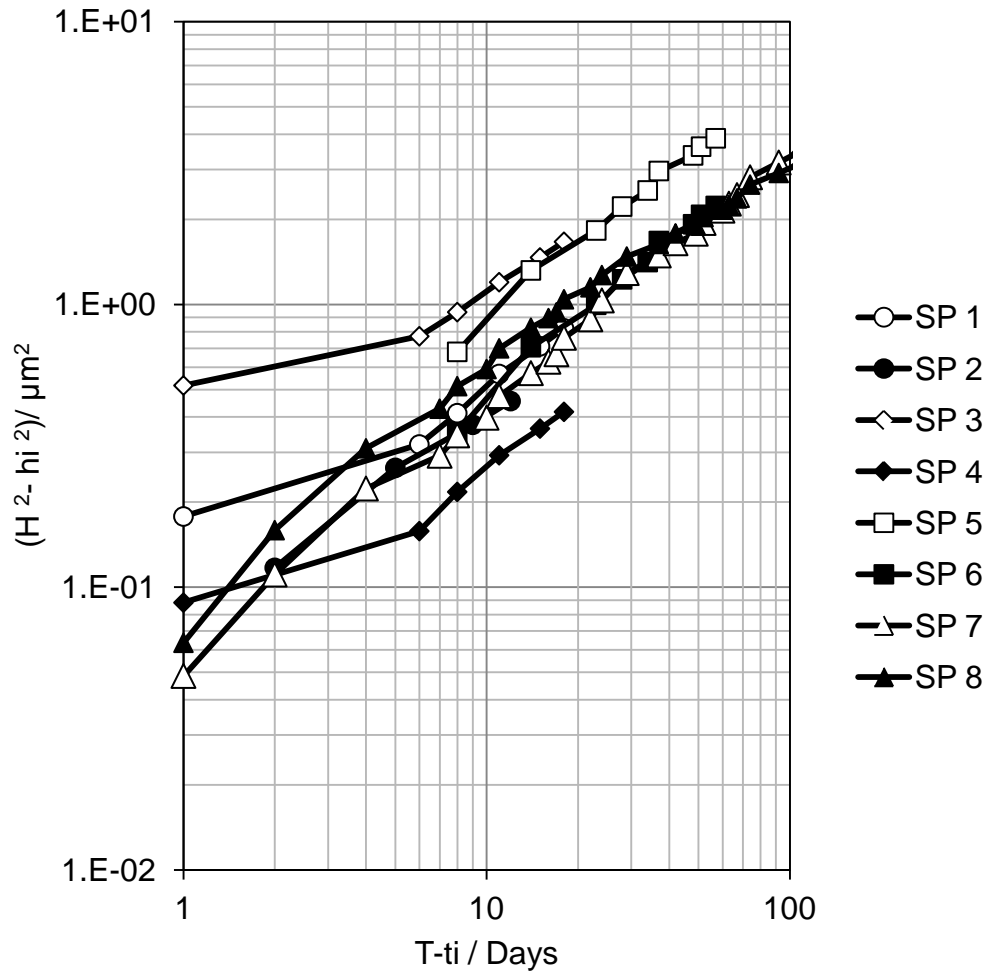


Figure 77: Accumulated thickness loss as a function of time starting at Stage II.

7.2.3.6 Comparison of EIS Results and Metallography

Metal loss determined by direct observation of metallographic cross sections of extracted specimens was subject to considerable spatial variability. To obtain a representative indication of direct metal loss, metallographic samples of 2 to 4 random cross sections of each specimen were prepared. For each cross section multiple (8-18) metallographs at different spots were taken, each spanning an approximate width of $480 \mu\text{m}$ of the interface. In each photo frame

15 evenly distributed vertical lines were traced perpendicular to the coating. The coating loss was measured for each line, recorded, and averaged to provide a penetration value for the frame (T_{AF}). The position of uncorroded intermetallic precipitates at the corroded layer helped to detect the position of the original coating before corrosion. The averaged penetration values (T_{AF}) for all the frames were averaged to find an overall penetration thickness (T_{ov}) for each specimen, with the result shown by red X symbols in Figure 78 A, where comparison with the metal loss estimated by EIS can be made as well. Appendix 2 shows representative metallographic evidence for each of the specimens evaluated, as well as a tabulation of mean, standard deviation, and range of the penetration values of all the frames of each specimen.

For clarity, Figure 78 B illustrates T_{ov} for each specimen as well as the uncertainty range which was obtained by finding the maximum and minimum value of T_{AF} for each specimen. In this graph the envelope of the penetration thickness data obtained from EIS data is shown as well.

As can be seen, the EIS estimates and the direct observations show the same general increasing trend with time, and differ numerically on average by not much above a factor of 2 (EIS yielding the lower values), with some overlap in the T_{ov} uncertainty range. This degree of correlation between electrochemical and direct corrosion assessments is typical of similar studies (Andrade et al., 1978; Mansfeld, 1976) and reflects both the natural scatter of both diagnostic procedures. Furthermore, there is likelihood of some corrosion rate underestimation on the part of the EIS data due to intrinsic limitations resulting

from corrosion localization (Sagüés and Kranc, 1996), which may have occurred during Stage I as indicated earlier. Consequently, both methods indicate an average loss of aluminized coating in the order of several μm after exposure times of only 1-3 months. Considering that the total outer aluminized layer is only about 35 μm thick, and that the coating loss showed large spatial variability in the cross sections examined, it is likely that penetration of the coating could take place after only a few years of service at multiple locations when a large surface area of aluminized steel (e.g. many square meters as was the case in the field) is exposed to limestone backfill.

Moreover, in the case of steel substrate exposure due to occurrence of pits, after initiation of corrosion (shown in Figure 59 for 150 days), the rate of the cathodic reaction, and as a result the overall rate of corrosion, is expected to be significantly enhanced. Such phenomena may significantly increase the rate of coating loss, at least locally, and therefore reduce the service life of the pipe.

7.3 Summary

The findings suggest the overall corrosion progression in flowing water as summarized in Figure 79. During Stage I the passive film on the outer layer of the aluminized coating is consumed by interaction with the high pH generated by dissolution of limestone under near-closed system conditions. After 1-2 weeks the film is completely consumed and active corrosion of the aluminum begins (Stage II) at a high rate. Corrosion products remain in place and transport limitation of one or more of the species responsible for the rate of corrosion

ensues in an increasingly thick film. Nevertheless, after several months of exposure a significant fraction of the aluminized coating had been consumed. Aluminate inclusions and the inner aluminized layer are less attacked. Corrosion of the underlying carbon steel, not addressed in the present experiments, is expected to take place at a later date, but the observed attack of the aluminized coating in such short time portends a dramatic reduction in the life expectancy of the pipe compared to the desired performance. The results thus provide an explanation for the early damage observed in the field.

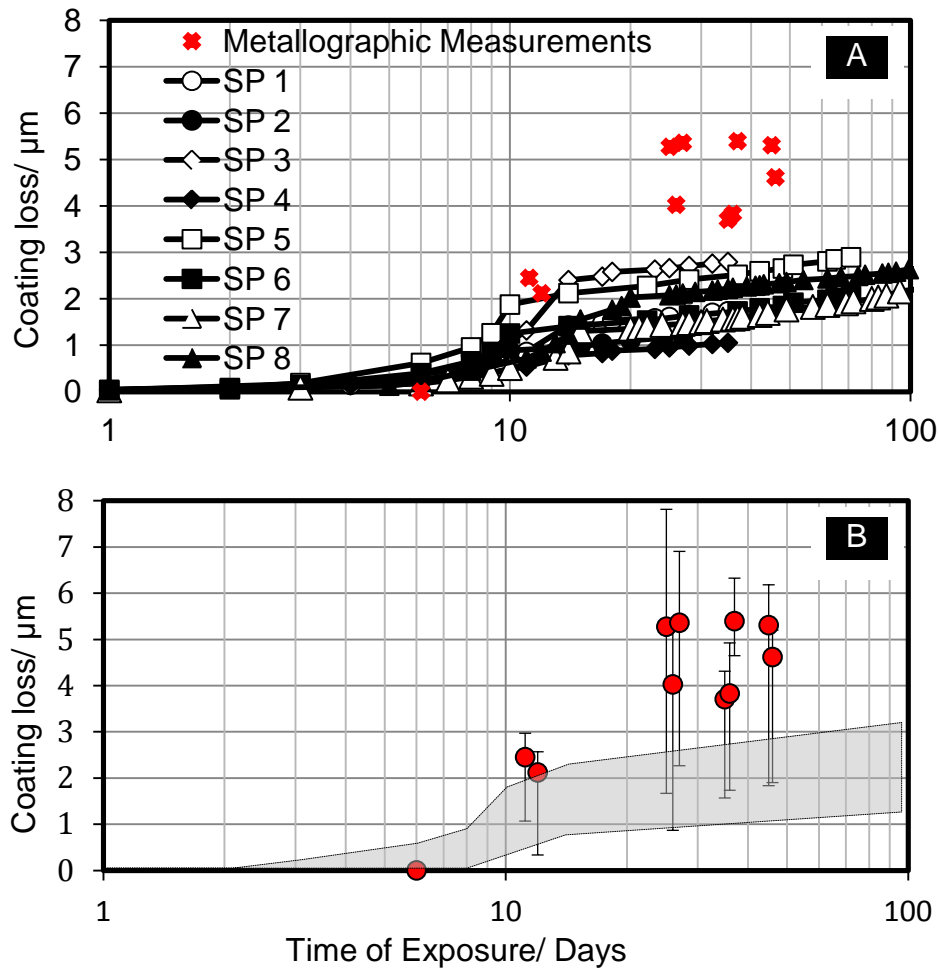


Figure 78: Total coating loss as a function of time measured by EIS data and by direction observation (Stars). B: Uncertainty range and EIS envelope.

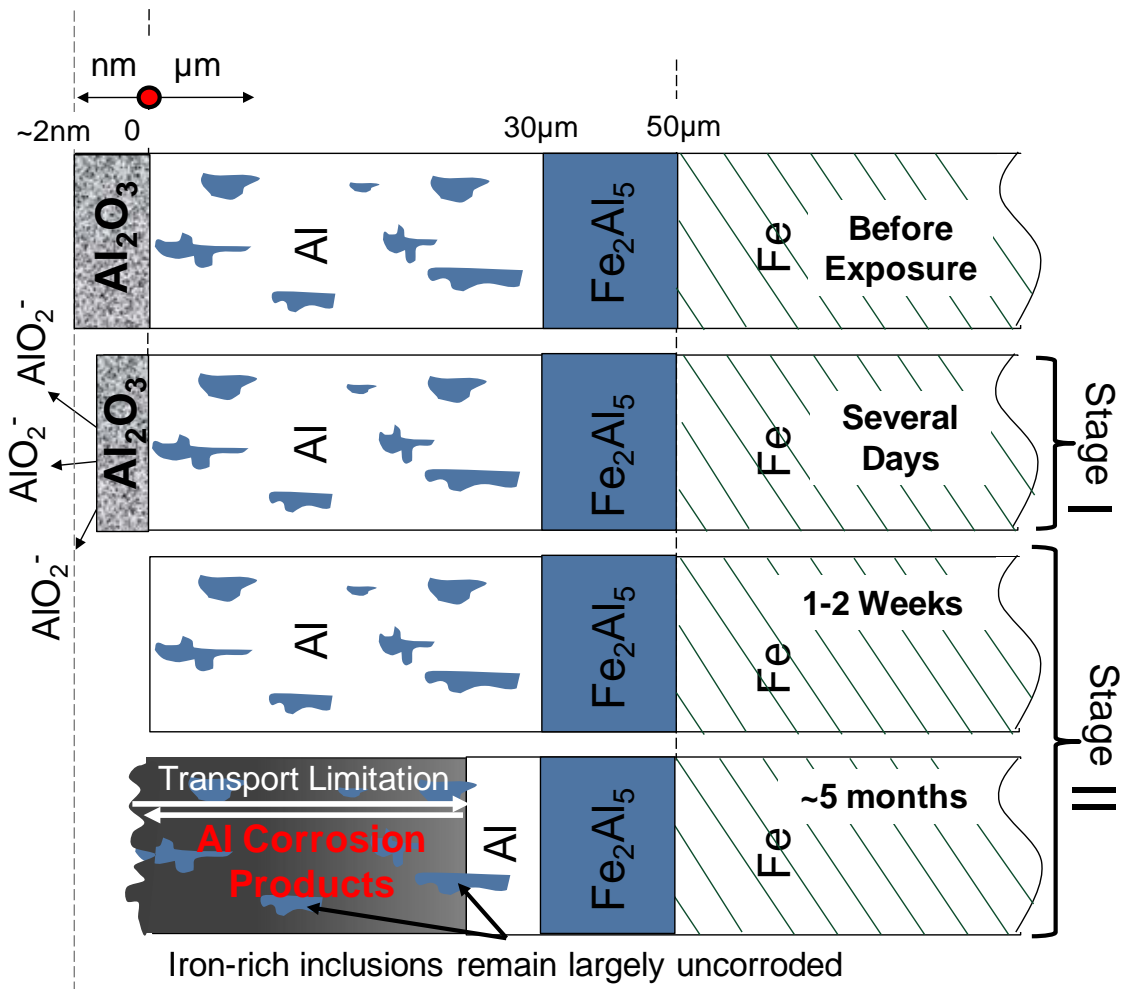


Figure 79: Scenario of corrosion progression under flowing water condition.

8. GENERAL DISCUSSION

8.1 Mode A Corrosion Issues

This research work has provided further evidence that the rib deformations of SRAP are prone to corrosion even in the absence of evident manufacturing defects. Experiments with heavily deformed aluminized steel (section 6.1) showed that severe corrosion can develop in heavily mechanically formed regions. The preliminary experiments, with small specimens (section 6.2.1) also showed indications of preferential corrosion at normally formed ribs in pipe that was recently manufactured to carefully implemented standards. However, the more extensive experiments, with large surface area samples, of similarly, newly produced pipe in both stagnant and renewed water (sections 6.2.2 and 6.2.3) did not show severe corrosion at the ribs. In those, more comprehensive tests, SRAP showed some rib corrosion but, overall, did not perform markedly different from regular corrugated pipe which is not subject to the severe local forming needed for SRAP.

The bending radius measurements reported in section 4 provided no indication of distinctly sharper radii in the ribs of pipe that experienced heavy Mode A corrosion, than in more recent pipe produced under careful quality control. Thus, those measurements failed to provide support to the hypothesis that much of that corrosion was due to routinely sharper radius settings when

forming the earlier pipe. Since the most severe Mode A corrosion incidents were associated with gross manufacturing defects (i.e. helical cuts), the above findings suggest that preferential rib corrosion in those cases reflected more some sort of associated production deficiency more than a feature inherent to the rib making process. Such deficiency (for example tearing from stuck rollers or inadequate lubrication) could have involved, in some of the ribs, mechanical coating distress significantly beyond that which is found in normal forming and resulted in conspicuous corrosion damage.

The experimental findings did not provide enough evidence to support the hypothesis that Mode A corrosion could have been mitigated by a somewhat more aggressive environment which would have partially activated the aluminized layer surface and hence galvanically protected the exposed steel. As shown in section 6.2.2, tests of large SRAP specimens with the most aggressive S+ solution showed only marginally more negative potentials than parallel tests with the solution S, and visual appearance as well as electrochemical impedance results were not dramatically different in comparison specimens exposed to both solutions. The small size preliminary experiments showed no significant S /S+ solution differentiation either. In all of the tests exposed steel was limited to small imperfections present in the as-received material.

The exposed edge experiments (section 6.3) were specifically designed to reveal the extent to which galvanic protection could be provided by the aluminized layer to a large area of exposed steel as it would be present in the case of a helical cut resulting from manufacturing deficiency. The experiments

confirmed that some protecting galvanic current was delivered to the steel, but they also indicated that the amount of protection was insufficient to substantially arrest corrosion of the steel. Importantly, these tests also revealed no strong differentiation between the S and S+ solution exposures which does not support the hypothesis that moderately more aggressive waters would have a strong beneficial effect in mitigating exposed steel corrosion. It is noted that, while the protective galvanic effect (regardless of how aggressive the solution is) was not substantial in the cut edge case, it may have had a more important mitigating effect for the smaller flaws present in the surface of as-received material. Such mitigation may have contributed to the lesser amount of rib corrosion encountered in the large specimen experiments (sections 6.2.2 and 6.2.3) than in the preliminary tests with small specimens (section 6.2.1). The latter had about half the ratio of ribbed surface to smooth surface than the former, and consequently less expected galvanic protection of any steel exposed at the rib deformations.

In summary, the findings from this work continue to suggest that much of the corrosion damage observed in the Mode A incidents was promoted more by manufacturing deficiencies and less by any possible inherent susceptibility of corrosion at the ribs of SRAP that is produced following appropriate quality control. The work confirmed the presence of some galvanic protection to exposed steel, but no particular protection enhancement was found by exposure to a lower resistivity environment.

8.2 Mode B Corrosion Issues

The results of the experiments in section 7.2 showed that high pH values, sufficient to cause dissolution of the passive film on aluminum, can develop under exposure to limestone in flowing natural water. In these conditions, extensive loss of coating was observed over a short time period. In contrast, exposure to water in contact with sand (section 7.1) did not result in alkaline conditions, and aluminized steel (in the absence of mechanical deformation) remained essentially corrosion free.

Corrosion of the aluminized film in the limestone medium with renewed water took place in two consecutive stages. In Stage I the passive film was consumed by interaction with the high pH medium. In Stage II active corrosion of the outer layer aluminized coating took place with formation of an increasingly thick corrosion product layer with associated transport limitations.

The findings substantiate for the first time an important vulnerability of aluminized steel in limestone soils and provide an explanation for the rapid onset deterioration observed at the field. It is noted that the experiments did not extend to a period where the underlying steel is significantly corroded, but that event is to be expected once the protective aluminized layer is compromised. With the environment remaining alkaline, it is natural to anticipate penetration of the steel to be mostly localized since that mode of corrosion is prevalent for steel under those conditions. These findings also provide strong evidence in support of service guidelines to disallow the use of limestone bedding for aluminized steel

pipe, including SRAP. Consideration should be given to examine the need of extending that provision to the use of solid aluminum alloy pipe.

9. CONCLUSIONS

1. Spiral Ribbed Aluminized Pipe (SRAP) premature corrosion incidents have occurred in two modalities. Mode A is associated with extensive corrosion at or near the ribs and has taken place in near-neutral regular soil environments. Mode A has been often associated with gross manufacturing defects (i.e. helical cuts). Mode B took place in pipe in contact with limestone backfill and corrosion damage was in the form of perforations not preferentially at the ribs and not necessarily associated with other deficiencies. Both modes resulted in severe corrosion after only a few years of service.
2. Corrosion, comparable to that in Mode A, was replicated in aluminized steel that had been severely deformed to expose significant amounts of steel at aluminized layer breaks. However, moderately strong deformation such as that involved in the normal forming of SRAP ribs did not consistently result in severe corrosion. In comparison tests SRAP showed some rib corrosion but, overall, did not perform markedly different from regular corrugated pipe (PCAP) which is not subject to the extent of forming needed for SRAP.

3. Experiments confirmed the presence of some galvanic protection to exposed steel in conditions comparable to those of Mode A. Limited evidence suggests that the protection was somewhat greater in the case of a lower resistivity environment.
4. A simple semi-quantitative computer model was constructed (using a Finite Element Modeling (FEM) platform) to investigate the corrosion propagation pattern of aluminized steel with exposed cut edges, replicating the severe manufacturing distress cases (Mode A). The model indicated that the aluminum coating next to the exposed edge was susceptible to severe corrosion, in accordance with the experimental data and initial assumptions.
5. Overall, the findings continue to suggest that much of the corrosion damage observed in the Mode A incidents was promoted more by manufacturing deficiencies and less by any possible inherent susceptibility of corrosion at the ribs of SRAP that is produced following appropriate quality control.
6. Experiments to explore the causes of Mode B corrosion showed that high pH values, sufficient to cause dissolution of the passive film on aluminum, can develop under exposure of limestone to flowing natural water. In these conditions, extensive loss of coating was observed over a short time

period. In contrast, exposure to water in contact with sand did not result in alkaline conditions, and aluminized steel, in the absence of mechanical deformation, remained essentially corrosion free.

7. Corrosion of the aluminized film in the limestone medium with renewed water, approximating Mode B conditions, took place in two consecutive stages. In Stage I the passive film was consumed by interaction with the high pH medium. In Stage II active corrosion of the outer layer aluminized coating took place with formation of an increasingly thick corrosion product layer with associated transport limitations.

8. The findings substantiate for the first time an important vulnerability of aluminized steel in limestone soils and provide an explanation for the rapid onset deterioration observed at the field under Mode B. Therefore, these findings provide strong evidence in support of service guidelines to disallow the use of limestone bedding for aluminized steel pipe, including SRAP.

10. FUTURE WORK

The following list addresses future investigations that merit consideration to further enhance our understanding of the corrosion performance of SRAP.

- Mode A investigation: As discussed in section 6.3.2, a simplistic computer model was formulated to investigate the corrosion propagation pattern at cut edges of aluminized steel (replicating the condition of mechanically damaged pipes in the field) exposed to simulated natural waters. The model provided good semi-quantitative analysis and indicated that the aluminum next to the cut edge is corroding faster than elsewhere, in accordance with the initial expectations. However, the model does not incorporate anodic corrosion of the steel substrate. Anodic corrosion of the steel substrate may intensify the corrosion of aluminum coating and may result in a shorter projected service life. Therefore, to create a realistic model, such feature should be considered in future work.
- Mode B investigation: As addressed in section 7.2.3.6, the corrosion of aluminized coating in contact with wet limestone is assumed to be generally uniform. However, at around 150 days of exposure, pits were observed at the surface of specimens. In the case of steel substrate exposure due to occurrence of pits, the rate of the cathodic reaction (and

the overall rate of corrosion), is expected to be significantly enhanced. Such phenomena may significantly increase the rate of coating loss, at least locally, and therefore reduce the service life of the pipe. This issue should be investigated in future work.

- Furthermore, as briefly mentioned in chapter 3, severe corrosion of the plain corrugated galvanized pipe segments that are used to join sections of SRAP was observed at a failure site (Appendix 5). The observation was not addressed in this work because the corrosion of galvanized steel pipes was not the focus of the study. However, as mentioned in the introduction, the premature failures of the pipe installations can be very costly. Therefore, any factors that may have an adverse effect on the service life of these pipes should be investigated carefully. In this case, future experiments with galvanically coupled galvanized and aluminized steel pipes may be conducted to further investigate the vulnerability of SRAP joining sections and their effect on overall performance of aluminized steel culvert pipes.

REFERENCES

- AK Steel, Aluminized Steel Type 2 Product Features (2007), http://www.aksteel.com/pdf/markets_products/carbon/T2_Data_Bulletin.pdf
- Akhoondan M. (2007), Electrochemical Corrosion Assessment of Mechanically Formed Aluminized Steel, Master's Thesis, University of South Florida.
- Akhoondan M, Sagüés A., Caseres L. (2008), Corrosion Assessment of Mechanically Formed Aluminized Steel, Corrosion/2008, Paper No. 1462, NACE International, Houston, TX, 2008.
- An J., Liu Y.B., Sun D.R. (2001), Mechanism of Bonding of Al–Pb Alloy Strip and Hot-Dip Aluminized Steel Sheet by Hot Rolling, *Materials Science Technology* 17, pp. 451-454.
- Andrade C., Gonzalez J. A. (1978), Quantitative measurements of corrosion rate of reinforcing steels embedded in concrete using polarization resistance measurements, *Werkstoffe Korrosion*, 29, pp. 515-519.
- Armstrong R.D., Braham V.J. (1996), Mechanism of Aluminum Corrosion in Alkaline Solutions, *Corrosion Science* 38, pp. 1463-1471.
- ASM Metals Handbook (1972), Vol. 7: Atlas of Microstructures of Industrial Alloys, 8th Ed. Metals Park, OH, p.260.
- Bednar L. (1989), Galvanized Steel Drainage Pipe Durability Estimation with a Modified California Chart, Paper No. 88-0341, 68th Annual Meeting, Transportation Research Board, Washington, D.C.
- Bessone J.B., Salinas D.R., Mayer C.E., EBERT M., Lorenz W.J. (1992), An EIS Study of Aluminium Barrier-Type Oxide Films Formed in Different Media, *Electrochimica Acta*, 37, pp. 2283-2290.
- Birbilis N., Buchheit R. G. (2005), Electrochemical Characteristics of Intermetallic Phases in Aluminum Alloys: An Experimental Survey and Discussion, *Journal of The Electrochemical Society*, 152, pp. 140-151.
- Bouayad A., Gerometta Ch., Belkebir A., Ambari A. (2003), Kinetic Interactions Between Solid Iron and Molten Aluminium, *Materials Science and Engineering*, A363, pp. 53-61.

- Boynton R. B. (1980), Chemistry and Technology of Lime and Limestone, John Wiley & Sons, NY.
- Caseres L. (2007), Electrochemical Behavior of Aluminized Steel Type 2 in Scale-Forming Waters, Ph.D. Dissertation, University of South Florida.
- Caseres L. and Sagüés A. (2006), Galvanic Behavior of Type 2 Aluminized Steel in Simulated Natural Waters", L. Cancun, Mexico, "Corrosion of Infrastructure", The Electrochemical Society, Pennington, NJ, 2007, ECS Transactions Vol. 13, Issue 13, 210th ECS Meeting , October 29-November 3, 2006, pp. 147-157.
- Caseres L., Sagüés A. (2005), Corrosion of Aluminized Steel in Scale Forming Waters, Paper No. 05348, Corrosion/2005, NACE International, Houston, TX.
- Castro P., Sagüés A., Moreno E.I., Maldonado L., Genesca J. (1996), Characterization of Activated Titanium Solid Reference Electrodes for Corrosion Testing of Steel in Concrete, Corrosion, 52, pp. 609-617.
- Cerlanek W.D., Powers R.G. (1993), Drainage Culvert Service Life Performance and Estimation, State of Florida Department of Transportation, Report No. 93-4A.
- CONCORR Florida (2007), Curlew Road Aluminized Steel Type II Pipe Failure Investigation, Prepared for FDOT State Materials Office, Gainesville, FL.
- Creus J., Mazille H., Idrissi H. (2000), Porosity Evaluation of Protective Coatings Electrodeposited on Steel, Surface and Coatings Technology 130, pp. 224-232.
- Davis J. R., (2000), Corrosion of Aluminum and Aluminum Alloys, p. 26, ASM International, OH.
- Epelboin L., Keddam M. (1970), Faradaic Impedances: Diffusion Impedance and Reaction Impedance, Journal of Electrochemical Society, Vol 117, pp.1052-1056.
- Fabjan C., Kazemi M., Neckel A. (1989), Untersuchungen über den Mechanismus und die Katalyse der kathodischen Sauerstoffreduktion an verschiedenen Metallen, Berichte der Bunsengesellschaft für physikalische Chemie, 84, pp. 1026-1031.
- Federal Highway Administration (FHWA) (2000), Durability Analysis of Aluminized Type 2 Corrugated Metal Pipe, US Department of Transportation Report No. FHWA-RD-97-140, McLean, VA.
- Florida Department of Transportation (2008) Optional Pipe Materials Handbook.
- Genies L., Bultel Y., Faure R., Durand R. (2003), Impedance Study of the Oxygen Reduction Reaction on Platinum Nanoparticles in Alkaline Media, Electrochimica Acta, 48, pp. 3879-3890.

- Godard H. P. (1967), Oxide Film Growth over Five Years on Some Aluminum Sheet Alloys in Air of Varying Humidity at Room Temperature, *Journal of Electrochemical Society*, Vol. 114, No. 4, pp. 354-356.
- Gupta A., Kumar R. (2006), Formability of galvanized interstitial-free steel sheets, *Journal of Materials Processing Technology*, 172, pp. 225-237.
- Harris D. C. (2010), *Quantitative Chemical Analysis*, 8th Ed., Freeman and Co., NY.
- Hong, Lim, Chung, Choi, (2002), Texture and Corrosion Mechanisms of Aluminized Steel Sheets, *Material Science Forum*, 408-412, pp. 1031-1036.
- Hwang, Song, Kim (2004), Effects of Carbon Content of Carbon Steel on Its Dissolution Into a Molten Aluminum Alloy, *Materials Science and Engineering* 390, pp. 437-443.
- Johnsson T., Nordhag L. (1984), Corrosion Resistance of Coatings of Aluminum, Zinc and their Alloys: Results of Four Years' Exposure, *Interfinish 84*, 11th World Congress on Metal Finishing, Jerusalem, Israel, 21-26 October 1984, pp. 412-418.
- Jones D.A. (1996), *Principles and Prevention of Corrosion*, Prentice Hall, NJ, pp. 75-113.
- Kimoto H. (1999), Galvanic Corrosion Behavior of Aluminized Steel in Seawater, *Corrosion Engineering*, 48, pp. 579-588.
- Kobayashi Sh., Yakou T. (2002), Control of Intermetallic Compound Layers at Interface Between Steel and Aluminum by Diffusion-treatment, *Materials Science and Engineering*, A338, pp. 44-53.
- Legault R.A., Pearson V.P. (1978), Kinetics of the Atmospheric Corrosion of Aluminized Steel, *Corrosion*, 34, pp. 344-348.
- Letterman R.D. (1983), Limestone Contactors for Corrosion Control in Small Water Supply Systems, Final Report submitted to the U.S. Environmental Protection Agency, Drinking Water Research, MERL, OH.
- Letterman R.D., Driscoll C. T., Hadad M. (1991), Contactors-Steady-State Design Relationships, *Journal of Environmental Engineering*, ASCE, 117, pp. 339-358.
- Li W., Liu S., Huang Q., Gu M. (2003), Hot- Dipped Aluminising (HDA) of a Low Carbon Steel Wire, *Materials Science and Technology*, 19, pp. 1025-1028.
- Liao C., Wei R. (1999), Galvanic Coupling of Model Alloys to Aluminum - A Foundation for Understanding Particle-induced Pitting in Aluminum Alloys, *Electrochimica Acta* 45, pp.881-888.

Lucas K.A., Clarke H. (1993), Corrosion of Aluminum-Based Metal Matrix Composites, p. 25, Research Studies Press LTD., NY.

Macdonald D. D., McKubre M. C. H. (1982), In Modern Aspects of Electrochemistry, Vol. 15, J. O'M Bockris, B. E. Conway, R. E. White, Editors, p. 61, Plenum, N.Y. Chapter 2, "Impedance Measurements in Electrochemical Systems".

Mansfeld F. (1976), The Polarization Resistance Technique for Measuring Corrosion Currents, in Advances in Corrosion Engineering and Technology (M. G. Fontana and R. H. Staehle, Ed.), Plenum Press 1976.

Materials Performance (2002), Historical Congressional Study: Corrosion Costs and Preventative Strategies in the United States. A Supplement to Materials Performance. NACE, July 2002.

McCafferty E. (2010), Introduction to Corrosion, Springer; Washington DC.

Molinas A., Mommandi A. (2009), Development of New Corrosion/Abrasion Guidelines for Selection of Culvert Pipe Materials, Final Report on Project No. CDOT-2009-11 to Colorado Department of Transportation, November 2009.

Montella C. (2001), EIS Study of Hydrogen Insertion Under Restricted Diffusion Conditions Two-step Insertion reaction, Journal of Electroanalytical Chemistry, 497 pp. 3-17.

Moon S. M., Pyun S. I. (1996), The Corrosion of Pure Aluminum During Cathodic Polarization in Aqueous Solutions, Corrosion Science, 39, pp. 399-408.

Morris G.E., Bednar L. (1998), Comprehensive Evaluation of Aluminized Steel Type 2 Pipe Field Performance, Published by AK Steel Corporation, Middletown, OH.

Murer N., Oltra R., Vuillemin B., and Neel O. (2010), Numerical Modelling of the Galvanic Coupling in Aluminium Alloys: A discussion on The Application of Local Probe Techniques, Corrosion Science, 52, pp. 130-139.

NACE, Corrosion Glossary (2012),
<http://events.nace.org/library/corrosion/glossaryletters/glossary-a.asp>.

Najafi T., Salem S., Bhattachar D., Salman B. (2008), An Asset Management Durability of In-situ Pipe Repair, Final Report on Project No. 0092-07-19 to Wisconsin Department of Transportation, June, 2008.

Najafi T., Harris W., Muszynski L., Alwood D., Mamaghani T., McBride D. (2011), An Asset Management Approach for Drainage Infrastructure and Culverts, Final Report on BD75 977-38 to Florida Department of Transportation, November, 2011.

Nisancioglu K. (1990), Electrochemical Behavior of Aluminum-Base Intermetallics Containing Iron, *Journal of Electrochemical Society* 137, pp. 69-77.

Pourbaix M. (1995), *Lectures on Electrochemical Corrosion*, p. 146, NACE International, TX.

Sagüés A. and Kranc S.C. (1996), Computer Modelling of Effect of Corrosion Macrocells on Measurement of Corrosion Rate of Reinforcing Steel in Concrete, p. 58 in *Techniques to Assess the Corrosion Activity of Steel Reinforced Structures*, ASTM STP 1276, N. Berke, E. Escalante, C. Nmai and D. Whiting, Eds., American Society for Testing and Materials, W. Conshohoken, PA.

Sagüés A. and Kranc S.C. (1992), Computation of Corrosion Macrocell Current Distribution and Electrochemical Impedance of Reinforcing Steel in Concrete, *Computer Modeling in Corrosion*. ASTM STP /154. R. S. Munn. Ed. American Society for Testing and Materials, PA 1992. pp. 95-112.

Sagüés A., N. D. Poor, L. Caseres, M. Akhoondan (2009), Development of a Rational Method for Predicting Corrosion of Metals in Soils and Waters, Final Report on Project No. BD497 submitted to Florida Department of Transportation. <http://www.dot.state.fl.us/research-center/>

Sagüés A. (1989), Corrosion Measurements of Aluminum Alloys and Reinforced Concrete for Determination of Culver Service Life, Final Report on Project No. 99700-7324 submitted to Florida Department of Transportation.

Schecher W. D., McAvory D. C. (2003), MINEQL+: A Chemical Equilibrium Modeling System, Environmental Research Software, Version 4.6 for Windows.

Scully J. R. (1993), Characterization of the Corrosion of Aluminum Thin Films Using Electrochemical Impedance Methods, *Electrochemical Impedance: Analysis and Interpretation*, ASTM STP 1188, J. R. Scully, D. C. Silverman, and M. W. Kendig, Eds., Philadelphia, pp. 276-296.

Sequeira R., Lung F. (1995), A Critical Data Analysis and Interpretation of The pH, Ion Loadings and Electrical Conductivity of Rainwater From The Territory of Hong Kong, *Atmospheric Environment*, 29, pp. 2439-2447.

Sluyters-Rehbach M., Sluyters J.H. (1984), *Comprehensive Treatise of Electrochemistry; Volume 9 Electrode Processes: Experimental Techniques*; E. Yeager, J.O'M. Bockris, B.E. Conway, S. Sarangapani, chapter 4 "AC Techniques", Plenum Press, 1984.

Snoeyink V. L., Jenkins D. (1980), Water Chemistry, p. 287, John Wiley & Sons, NY.

Stoudt M. R., Fink J. L., Dante J. F., Ricker R.E. (1995), Compatibility with Metals, Fire Suppression System Performance of Alternative Agents in Aircraft Engine and Dry Bay Laboratory Simulations, NIST SP 890, Vol. 1, R. G. Gann, Ed., NM, p. 128.

Townsend H.E., Borzillo A.R. (1987), Twenty-Year Atmospheric Corrosion Tests of Hot-dip Coated Sheet Steel, Materials Performance 26, pp. 37-41.

United States Department of Agriculture (USDA) (2003), Natural Resources Conservation Service, Soil Survey, Florida Counties, 2003.

Virta R. L. (2010), 2009 Minerals Yearbook, U.S. Geological Survey.

Zhang J., Klasky M., Letellier B. (2009), The Aluminum Chemistry and Corrosion in Alkaline Solutions, Journal of Nuclear Materials, 384, pp.175-189.

APPENDICES

Appendix 1: Sample Polarization Diagrams of Al and Steel

These tests were exploratory in nature and addressed limited experimental conditions, but they are presented here for completeness as they provide some insight on the corrosion conditions prevalent in this system. Typical polarization diagrams based on preliminary experiments are shown in Figure A-1 for aluminized steel and steel specimens in solution S.

The steel specimens (exposed area of 1cm^2) were prepared by grinding off the aluminum coating from aluminized steel sheets using 600 US grit SC paper. These specimens were immersed in the solution for periods ranging from 6 to 12 days until a uniform rust layer formed over the entire exposed steel surface. The aluminized specimens were rectangular, 2 in by 3 in (5 by 7.6 cm) with both sides exposed but with the edges covered with epoxy. For the aluminized specimens the cell configuration was similar to that shown in Figure 27. These specimens were kept in the solution for 1 day before conducting the polarization tests. Table A-1 lists the tests conducted. All potentiodynamic scans started at or close to the E_{OC} and were conducted at a scan rate of 0.05mV/sec per the schedule indicated. The results shown in Figure A-1 (normalized for exposed metal area) are not corrected for solution resistance, which may be the cause of the curvature in the anodic portion of the aluminized steel polarization curves. Before reaching that suspected resistance polarization regime, the anodic aluminized steel behavior appeared to be indicative of activation polarization, possibly reflecting some incipient pitting, considering the relatively high values of E_{OC} in the samples that were evaluated.

Appendix 1 (continued)

To elucidate this issue, continuation tests with a larger sample population and detailed accounting for solution resistance would be necessary.

For the steel specimens the exact distances between reference electrode and specimens were not recorded in these exploratory tests. However, the results from multiple specimens show similar curves with the onset of a nearly potential-independent regime together with random current fluctuations. This behavior is typical of diffusional limitation of the cathodic reaction in the presence of some amount of convective action.

The corresponding limiting current density is in the order of $\sim 4 \cdot 10^{-5} \text{ A/cm}^2$, which is in the order of values normally associated with reduction of oxygen in stagnant water conditions on atmospheric exposure (McCafferty, 2010, p188) where the IR drop would not be significant. This value was taken into account when addressing the cathodic current rate on exposed steel in the current distribution I model discussed in section 6.3.2.

Appendix 1 (continued)

Table A-1: Exploratory polarization tests

Specimen	Internal ID Code	Initial E / V _{SCE}	Apex E / V _{SCE}	Final E / V _{SCE}	Scan Rate / mV-sec ⁻¹	Exposure Time
Aluminized SP 1	New 2by3 in S specimen 9-22-11	-0.601	-0.05	-1.507	0.05	1 Day
Aluminized SP 2	New 2by3 in fresh S 10-17-12	-0.593	0	-1.589	0.05	1 Day
Aluminized SP 3	New 2by3 in fresh S 10-20-12	-0.500	-1	0	0.05	1 Day
Steel SP 1	Fe1 in bin 4	-0.621	-0.9	-0.1	0.05	7 Days
Steel SP 2	Fe2 in bin 3	-0.603	-0.9	-0.603	0.05	12 Days
Steel SP 3	Fe2 in bin 2	-0.628	-0.9	-0.1	0.05	6 Days

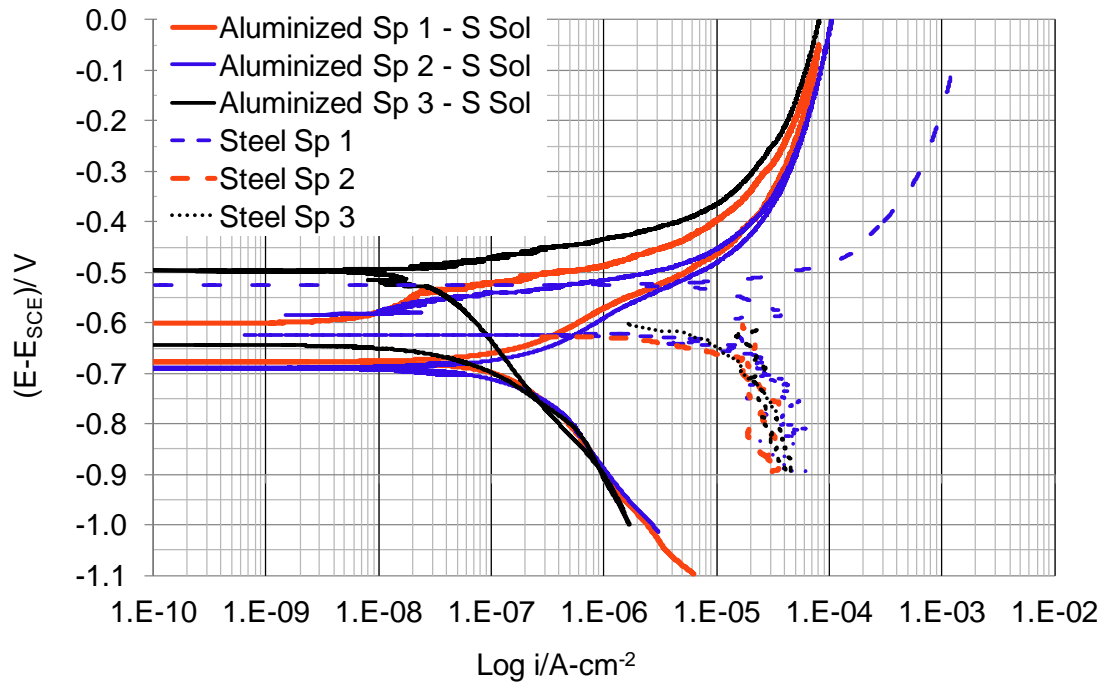


Figure A-1: Polarization diagrams for aluminized steel with sealed edges (solid lines) and steel (dashed-lines) in S solution.

Appendix 2: Example of Fit and EIS Raw Data for EIS Interpretation of Stage I, Stage II and Control Specimens

For Stage I, the equivalent circuit shown in Figure 68 provided a close fit for the EIS data of Stage I as explained in section 7.2.3.4. A representative example of EIS data and the fit at Stage I is shown in Nyquist and Bode diagrams in Figure A-2. As explained in section 7.2, EIS tests were conducted using a Gamry™ Ref. 600 potentiostat in the frequency range 100 kHz to 10 mHz using sinusoidal signals of 10 mV rms amplitude (3 point / decade). It was determined that the EIS response at frequencies >100 Hz was dominated by water dielectric properties and was irrelevant to determination of corrosion performance. Therefore, the data was only fitted for the frequency range 10 mHz to 100Hz. The analyses were conducted with the Gamry Echem Analyst software using the Simplex algorithm.

The example in Figure A-2 corresponds to SP 8 at 5 days of exposure. Table A-2 indicates the calculated fit parameter values of each component as well as the uncertainty range provided by the analysis software.

Table A-2: EIS fit parameter values, SP 8

Stage I	Fit Values	+/- Error	Units
R _{sol}	1.32E+03	20.2	ohms
R ₂	1406	430.9	ohms
R ₁	500.9	135.0	ohms
CPE ₂	5.65E-03	2.2E-03	Sec ⁽¹⁻ⁿ⁾
n ₂	8.23E-01	0.2	
CPE ₁	4.22E-04	1.6E-04	Sec ⁽¹⁻ⁿ⁾
n ₁	9.12E-01	0.1	

Appendix 2 (continued)

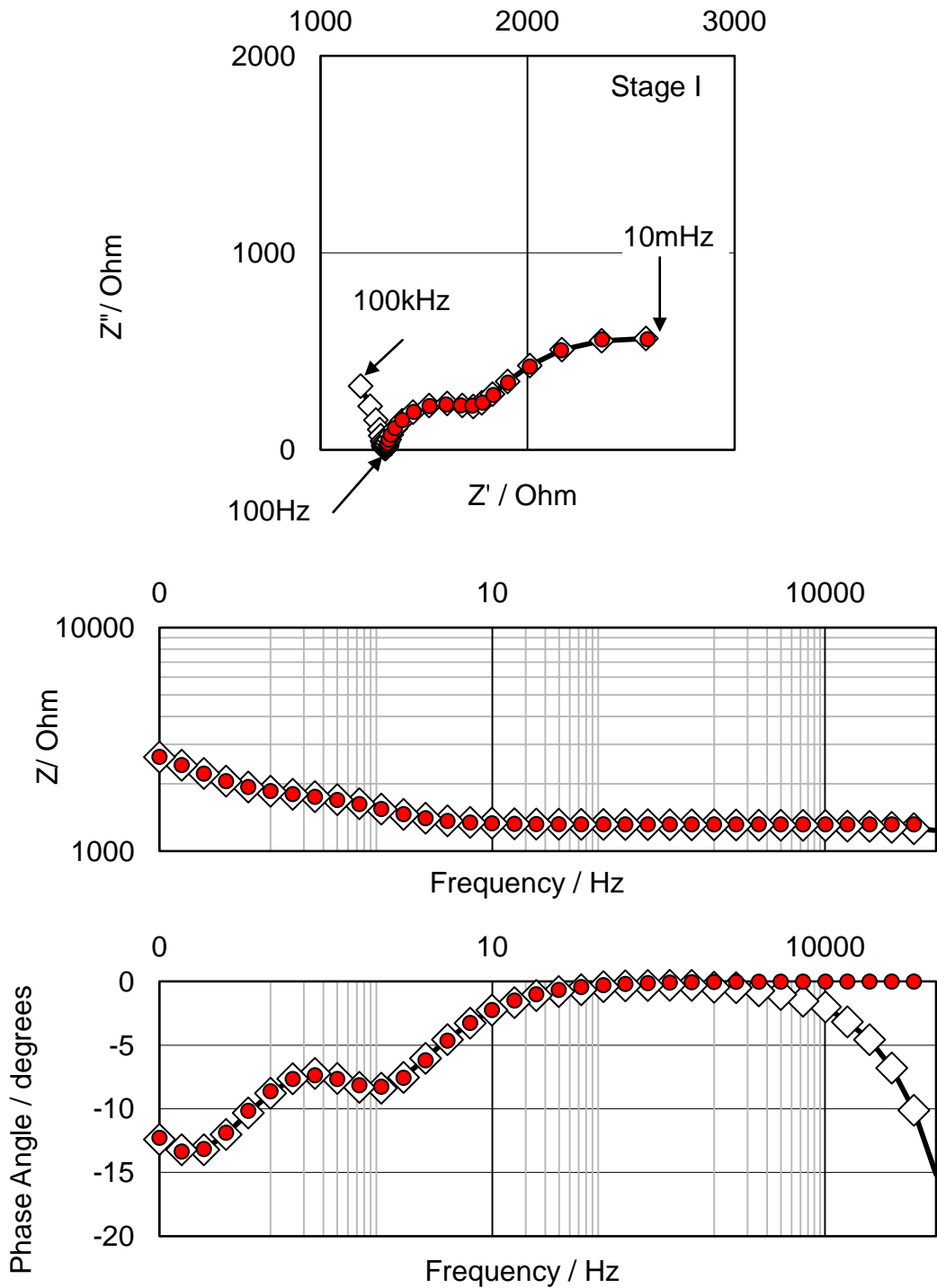


Figure A-2: Nyquist diagrams (Top), bode (Middle), and phase angle (Bottom) for Stage I. Raw data is shown with empty squares, and the fit ($10\text{mHz} < \text{freq} < 100\text{Hz}$) is shown with red dots. Shown for SP 8 and 5 days of exposure. (3 points/decay).

Appendix 2 (continued)

The following is an example calculation of estimated corrosion rate for this EIS measurement. Using Eq (10), the estimated corrosion current density for stage I (shown in Table A-2) was calculated by:

$$R_1 = 500.9 \Omega$$

$$i_{\text{corr}} = B/R_p = 0.052 \text{ V} / (500.9) = 1.04 \times 10^{-4} \text{ A}$$

$$\text{Given exposure area} = \sim 77 \text{ cm}^2$$

$$\Rightarrow i_{\text{corr}} = 1.04 \times 10^{-4} \text{ A} / 77 \text{ cm}^2 = 1.35 \times 10^{-6} \text{ A/cm}^2 = 1.35 \mu\text{A/cm}^2$$

where by Faradaic conversion for aluminum: $1 \mu\text{A/cm}^2 = 10.89 \mu\text{m/Yr}$

$$\Rightarrow i_{\text{corr}} = 14.704 \mu\text{m/Yr}$$

For Stage II, the equivalent circuit shown in Figure 72 provided a close fit for the EIS data of Stage II as explained in section 7.2.3.5. A representative example of EIS data and the fit at Stage II is shown in Nyquist and Bode diagrams in Figure A-3. A similar test set up to Stage I was applied.

Table A-3: EIS fit values for Stage II

Stage II	Fit Values	+/- Error	Units
R _{p3}	1.48E+03	1.60E+02	ohms
R _{sol}	1.50E+03	1.80E+01	ohms
CPE ₃	2.34E-03	2.05E-04	Sec ⁽¹⁻ⁿ⁾

Appendix 2 (continued)

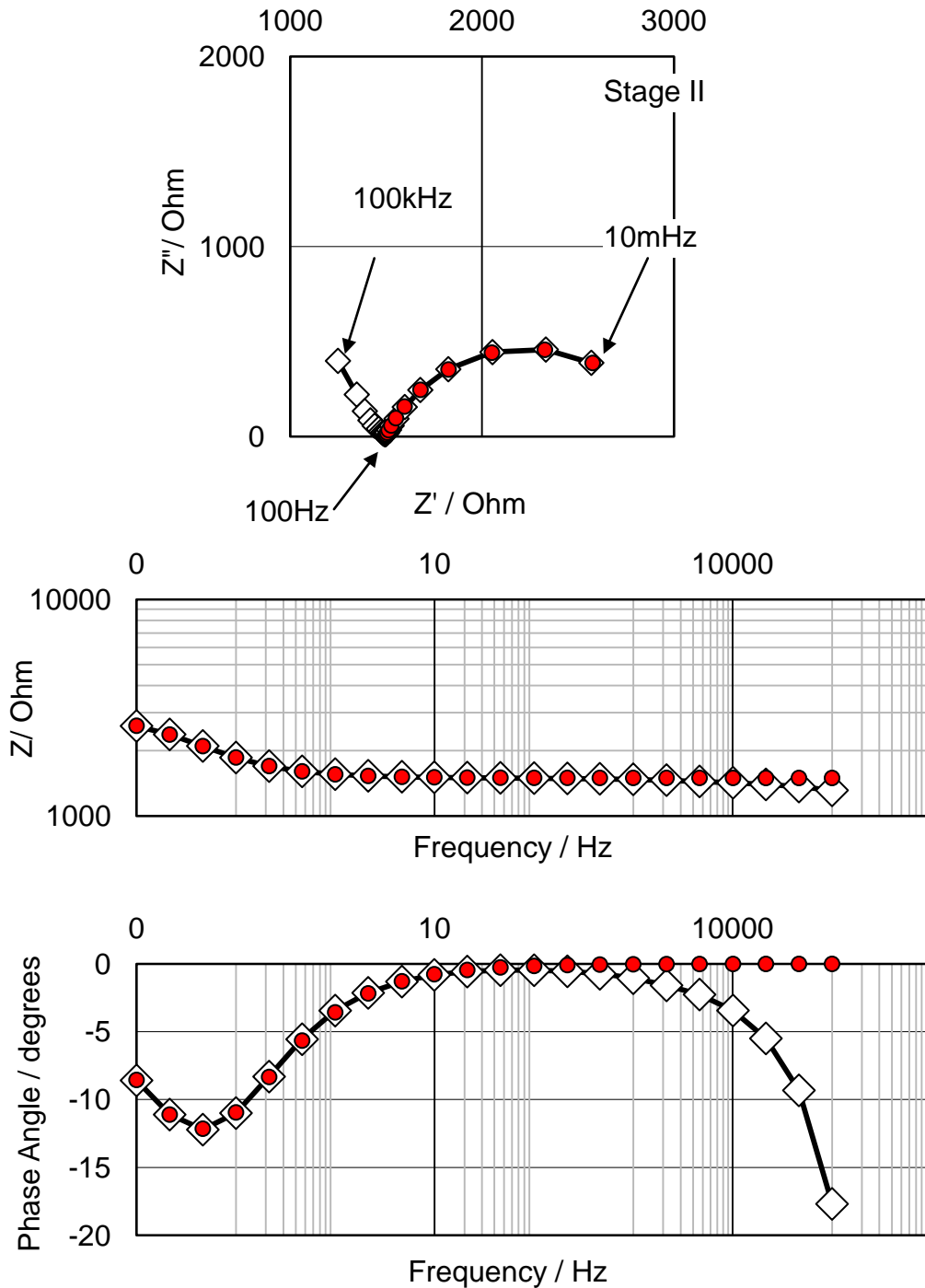


Figure A-3: Nyquist diagrams (Top), bode (Middle), and phase angle (Bottom) for Stage II. Raw data is shown with empty squares, and the fit ($10\text{mHz} < \text{freq} < 100\text{Hz}$) is shown with red dots. Shown for SP 8 and 32 days of exposure. (3 points/ decay).

Appendix 2 (continued)

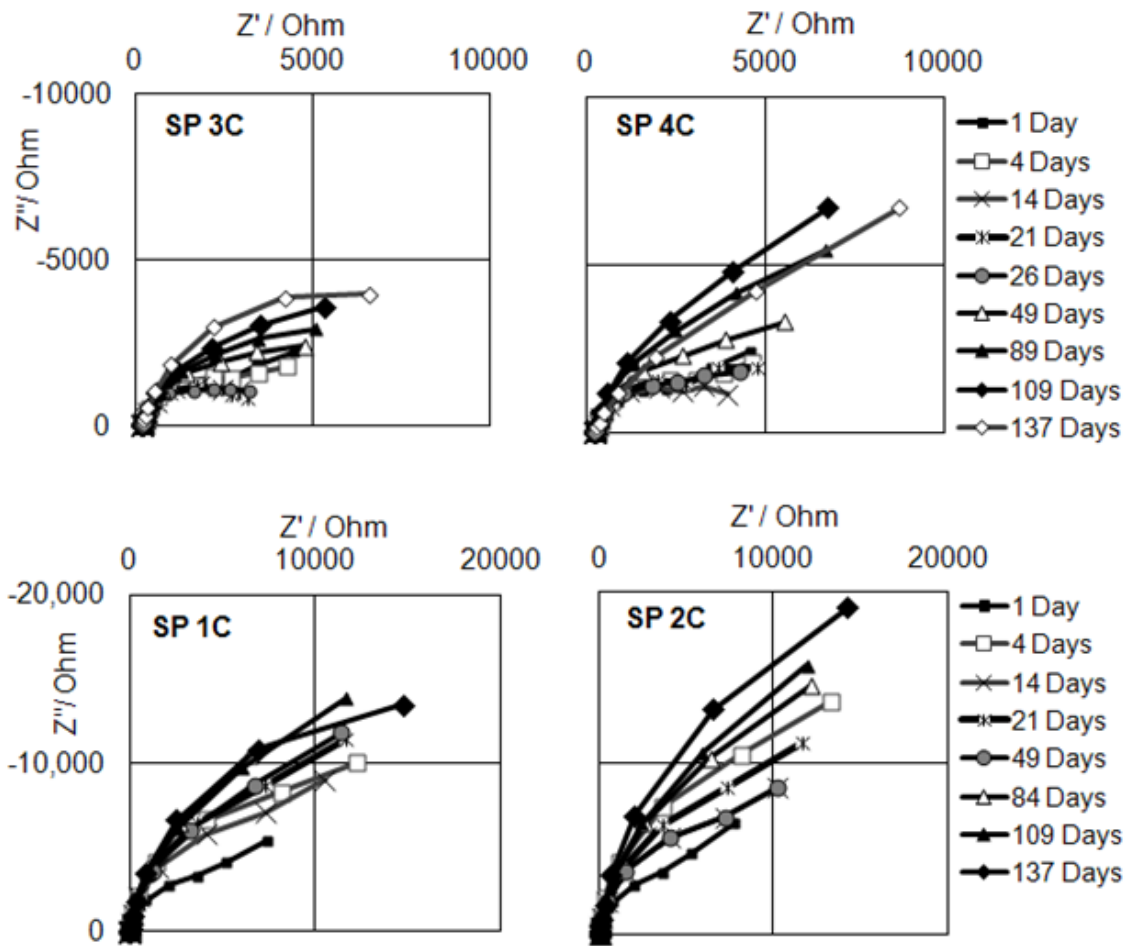


Figure A-4: Nyquist diagrams for control specimens over 137 days of exposure. Diagrams generally consist of a depressed arc with increasing size as a function of time ($10\text{mHz} < \text{freq} < 100\text{Hz}$ and 3 points/ decay).

Appendix 2 (continued)

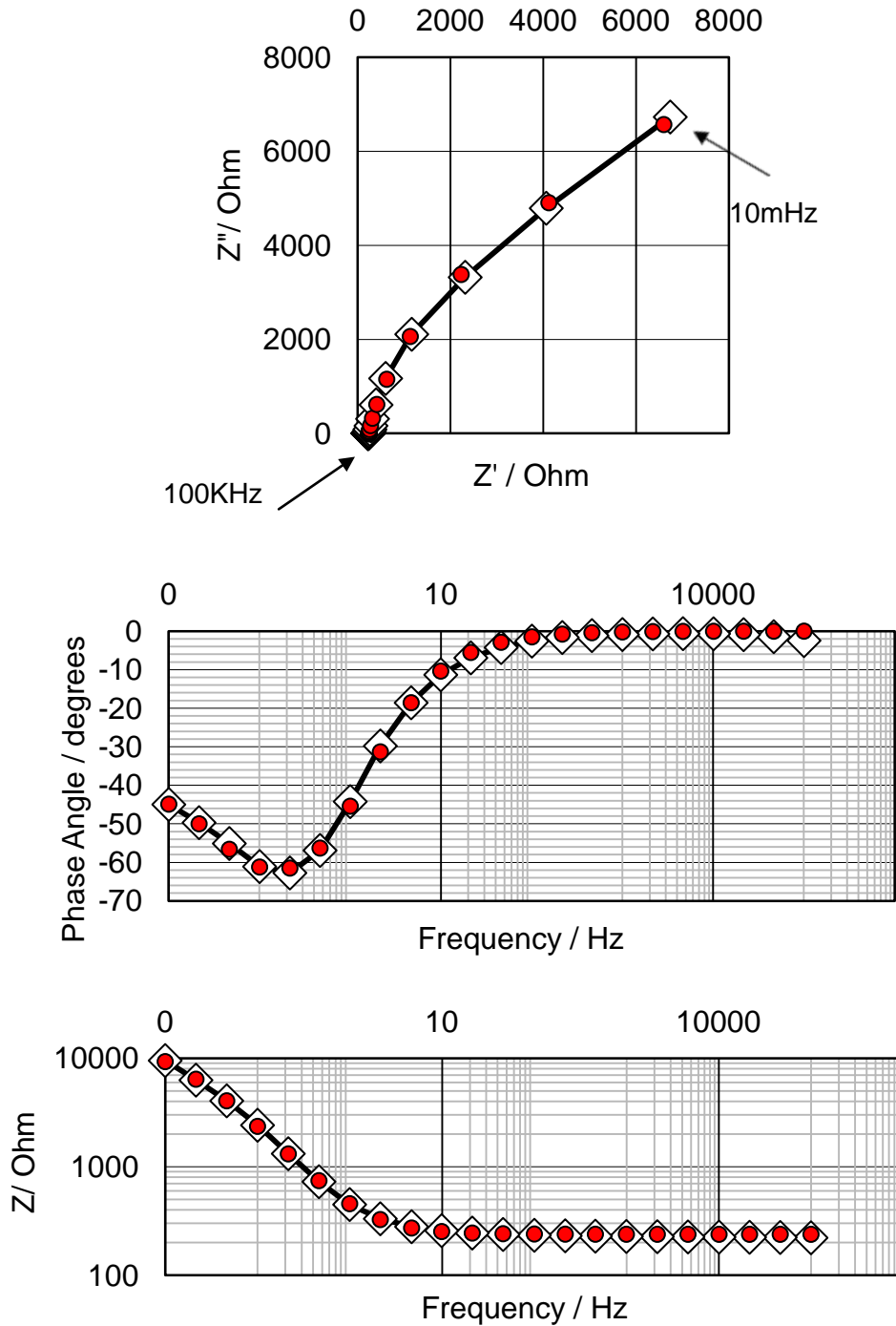


Figure A-5: Typical fit for late exposure days of control specimens. Nyquist diagrams (Top), bode (Middle), and phase angle (Bottom) for SP C 4 at 109 Days. Raw data is shown with empty squares, and the fit (10Hz<freq<100Hz) is shown with red dots (3 points/ decay).

Appendix 2 (continued)

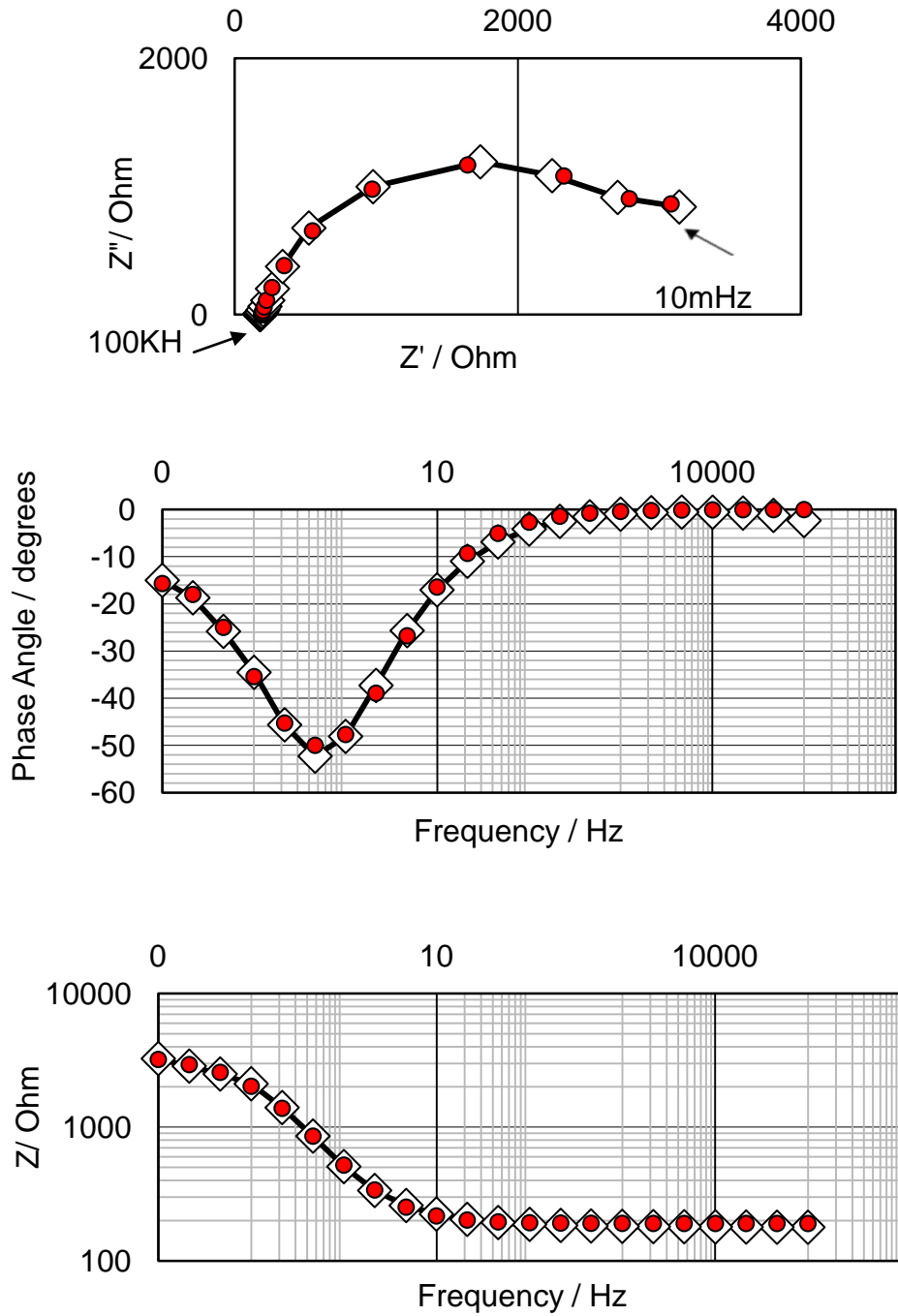


Figure A-6: Typical fit for early exposure days of control specimens. Nyquist diagrams (Top), Bode (Middle), and phase angle (Bottom) for SP C 3 at 21 Days. Raw data is shown with empty squares, and the fit (10Hz<freq<100Hz) is shown with red dots (3 points/ decay).

Appendix 2 (continued)

For Tables A-4 through Table A-11, symbol * indicates the extrapolated values during transition time. All resistance values are in ohms and the capacitances are in sec⁽¹⁻ⁿ⁾ units.

Table A-4: EIS analysis parameters for SP1

SP 1									
Days	Rpn	Rsol	R2	R1	Yo2	n2	Yo1	n1	R1/Rpn
1	1.4E+03	7.3E+02	1.9E+03	5.4E+02	5.1E-03	0.747	1.6E-04	0.952	0.376
4	1.4E+03	7.0E+02	1.4E+03	6.4E+02	5.7E-03	0.823	2.7E-04	0.903	0.452
8	6.9E+02	7.7E+02	6.2E+02	3.6E+02	1.1E-02	0.781	4.7E-04	0.912	0.515
11	3.0E+02	9.0E+02		1.2E+02*					0.391*
14	2.7E+02	8.7E+02		1.1E+02*					0.395*

Days	Rpn	Rsol	Rp3	n3	Yo3
17	3.8E+02	8.2E+02	7.9E+02	0.482	3.40E-03
18	6.1E+02	9.6E+02	1.0E+03	0.522	3.34E-03
23	9.3E+02	9.2E+02	1.5E+03	0.562	2.31E-03
25	1.0E+03	9.4E+02	1.7E+03	0.578	2.19E-03
28	1.0E+03	8.6E+02	1.5E+03	0.597	2.02E-03
32	1.1E+03	8.7E+02	1.6E+03	0.597	1.78E-03
35	1.3E+03	9.0E+02	1.9E+03	0.615	1.70E-03

Appendix 2 (continued)

Table A-5: EIS analysis parameters for SP2

		SP 2									
		Days	Rpn	Rsol	R2	R1	Yo2	n2	Yo1	n1	R1/Rpn
Stage I		1	1.6E+03	1.2E+03	2.3E+03	4.8E+02	5.5E-03	0.910	2.0E-04	0.859	0.308
		3	1.2E+03	1.6E+03	2.6E+03	5.4E+02	5.1E-03	0.710	4.2E-04	0.900	0.440
		6	9.7E+02	1.5E+03	1.2E+03	4.3E+02	7.8E-03	0.800	5.5E-04	0.890	0.445
		8	5.3E+02	1.4E+03	5.4E+02	2.5E+02	1.3E-02	0.760	7.9E-04	0.874	0.470
		10	3.0E+02	1.7E+03	3.0E+02	1.5E+02	2.5E-02	0.780	1.7E-03	0.796	0.502
		Days	Rpn	Rsol	Rp3	n3	Yo3				
Stage II		15	3.2E+02	1.6E+03	7.6E+02	0.395	5.2E-03				
		17	4.5E+02	1.6E+03	8.7E+02	0.475	4.2E-03				
		20	5.7E+02	1.5E+03	1.0E+03	0.533	3.5E-03				
		24	8.3E+02	1.4E+03	1.4E+03	0.581	2.7E-03				
		27	1.0E+03	1.5E+03	1.8E+03	0.609	2.3E-03				

Table A-6: EIS analysis parameters for SP3

		SP 3									
		Days	Rpn	Rsol	R2	R1	Yo2	n2	Yo1	n1	R1/Rpn
Stage I		1	1.6E+03	1.5E+03	1.9E+03	6.4E+02	5.1E-03	0.830	2.7E-04	0.890	0.414
		4	1.2E+03	2.0E+03	1.3E+03	4.0E+02	6.6E-03	0.810	4.2E-04	0.913	0.327
		8	1.1E+03	1.8E+03	5.7E+02	2.4E+02	1.3E-02	0.790	9.4E-04	0.876	0.221
		11	5.3E+02	2.0E+03	2.8E+02	7.5E+01	2.0E-02	0.350	2.3E-03	0.800	0.139
		14	1.4E+02	2.1E+03		5.6E+01*					
		Days	Rpn	Rsol	Rp3	n3	Yo3				
Stage II		17	1.4E+02	2.2E+03	5.4E+02	0.546	6.1E-03				
		18	2.2E+02	2.3E+03	5.9E+02	0.579	5.2E-03				
		23	4.1E+02	2.4E+03	1.4E+03	0.646	3.4E-03				
		25	8.6E+02	2.3E+03	1.6E+03	0.666	3.0E-03				
		28	9.7E+02	2.1E+03	1.5E+03	0.672	2.7E-03				
		32	9.8E+02	2.1E+03	1.4E+03	0.683	2.5E-03				
		35	1.0E+03	2.2E+03	1.7E+03	0.692	2.3E-03				

Appendix 2 (continued)

Table A-7: EIS analysis parameters for SP4

SP 4

Days	Rpn	Rsol	R2	R1	Yo2	n2	Yo1	n1	R1/Rpn
1	1.6E+03	1.1E+03	2.3E+03	6.6E+02	4.7E-03	0.830	2.62E-04	0.878	0.404
4	1.5E+03	1.6E+03	1.6E+03	6.4E+02	4.5E-03	0.820	3.52E-04	0.873	0.428
8	1.5E+03	1.5E+03	1.2E+03	3.5E+02	8.0E-03	0.790	5.89E-04	0.883	0.224
11	8.5E+02	1.9E+03	5.5E+02	3.1E+02	1.4E-02	0.870	9.47E-04	0.803	0.360
14	6.3E+02	1.8E+03		2.5E+02*					0.395*

Days	Rpn	Rsol	Rp3	n3	Yo3
17	2.6E+02	1.8E+03	8.3E+02	0.413	5.2E-03
18	3.0E+02	2.1E+03	1.2E+03	0.413	4.2E-03
23	4.5E+02	1.9E+03	1.8E+03	0.560	2.7E-03
25	9.1E+02	2.3E+03	1.6E+03	0.666	3.0E-03
28	1.0E+03	1.6E+03	1.8E+03	0.618	2.3E-03
32	1.1E+03	1.6E+03	2.0E+03	0.640	2.0E-03
35	1.3E+03	1.8E+03	2.4E+03	0.639	1.8E-03

Appendix 2 (continued)

Table A-8: EIS analysis parameters for SP5

SP 5

Days	Rpn	Rsol	R2	R1	Yo2	n2	Yo1	n1	R1/Rpn
1	1.6E+03	6.9E+02	2.1E+03	5.1E+02	6.6E-03	0.890	3.4E-04	0.918	0.327
2	1.6E+03	6.8E+02	5.6E+03	5.2E+02	3.5E-03	0.630	3.7E-04	0.944	0.328
3	1.0E+03	7.8E+02	1.9E+03	3.8E+02	7.5E-03	0.750	6.4E-04	0.905	0.379
6	3.1E+02	8.6E+02	2.4E+02	1.2E+02	2.9E-02	0.720	1.9E-03	0.826	0.376
8	2.5E+02	1.2E+03	2.1E+02	9.1E+01	3.7E-02	0.660	3.2E-03	0.744	0.359
9	1.7E+02	7.5E+01		6.6E+01*					0.388*
10	2.1E+02	1.1E+03		8.1E+01*					0.390*

Days	Rpn	Rsol	Rp3	n3	Yo3
14	3.8E+02	1.2E+03	4.9E+02	0.569	8.4E-03
22	9.7E+02	1.2E+03	9.1E+02	0.651	4.2E-03
28	9.6E+02	1.3E+03	1.1E+03	0.681	3.2E-03
37	1.2E+03	1.2E+03	1.4E+03	0.707	2.7E-03
42	1.2E+03	1.2E+03	1.4E+03	0.719	2.6E-03
48	1.3E+03	1.2E+03	1.5E+03	0.726	2.4E-03
51	1.5E+03	1.2E+03	1.7E+03	0.734	2.3E-03
62	1.6E+03	1.2E+03	1.9E+03	0.745	2.1E-03
65	1.7E+03	1.2E+03	2.1E+03	0.748	2.1E-03
71	2.1E+03	1.2E+03	2.7E+03	0.758	2.0E-03
90	1.8E+03	1.2E+03	2.4E+03	0.769	1.9E-03
97	1.8E+03	1.2E+03	2.3E+03	0.769	1.9E-03
104	1.7E+03	1.1E+03	2.3E+03	0.771	1.8E-03

Appendix 2 (continued)

Table A-9: EIS analysis parameters for SP6

SP 6

Days	Rpn	Rsol	R2	R1	Yo2	n2	Yo1	n1	R1/Rpn
1	2.2E+03	1.0E+03	2.9E+03	8.1E+02	4.5E-03	0.870	2.8E-04	0.895	0.360
2	2.0E+03	1.2E+03	2.7E+03	7.5E+02	5.2E-03	0.880	4.0E-04	0.871	0.382
3	1.4E+03	1.2E+03	2.3E+03	4.7E+02	5.4E-03	0.750	5.2E-04	0.895	0.349
6	3.9E+02	1.3E+03	5.4E+02	1.9E+02	1.3E-02	0.650	1.0E-03	0.883	0.496
8	3.3E+02	1.5E+03	1.0E+03	1.2E+02	1.9E-02	0.490	1.6E-03	0.824	0.354
9	2.7E+02	1.5E+03		1.1E+02*					0.388*
10	3.1E+02	1.6E+03		1.2E+02*					0.390*

Days	Rpn	Rsol	Rp3	n3	Yo3
14	5.0E+02	1.7E+03	7.6E+02	0.504	6.2E-03
22	1.3E+03	1.8E+03	1.2E+03	0.630	3.5E-03
28	1.1E+03	1.8E+03	1.4E+03	0.653	2.8E-03
37	1.3E+03	1.8E+03	1.6E+03	0.680	2.4E-03
42	1.4E+03	1.8E+03	1.7E+03	0.692	2.3E-03
48	1.5E+03	1.8E+03	1.8E+03	0.698	2.2E-03
51	1.6E+03	1.7E+03	2.0E+03	0.702	2.1E-03
62	1.8E+03	1.8E+03	2.2E+03	0.714	1.9E-03
65	1.9E+03	1.8E+03	2.4E+03	0.720	1.9E-03
71	2.3E+03	1.7E+03	3.2E+03	0.728	1.8E-03
90	1.9E+03	1.7E+03	2.7E+03	0.738	1.7E-03
97	1.9E+03	1.6E+03	2.6E+03	0.741	1.7E-03
104	2.0E+03	1.7E+03	2.8E+03	0.741	1.7E-03

Appendix 2 (continued)

Table A-10: EIS analysis parameters for SP7

SP 7

Days	Rpn	Rsol	R2	R1	Yo2	n2	Yo1	n1	R1/Rpn
1	2.2E+03	1.0E+03	1.8E+03	6.7E+02	5.0E-03	0.840	2.6E-04	0.881	0.309
3	2.2E+03	9.8E+02	1.9E+03	9.0E+02	4.0E-03	0.890	3.8E-04	0.834	0.417
6	1.1E+03	1.1E+03	1.3E+03	4.4E+02	7.1E-03	0.860	4.7E-04	0.877	0.386
7	7.2E+02	1.1E+03	6.4E+02	2.9E+02	1.1E-02	0.790	6.3E-04	0.891	0.411
8	6.0E+02	1.2E+03	4.4E+02	2.6E+02	1.3E-02	0.810	7.8E-04	0.877	0.433
9	8.3E+02	1.2E+03	7.8E+02	3.3E+02	8.8E-03	0.820	8.7E-04	0.850	0.397
10	7.9E+02	1.2E+03	6.2E+02	3.2E+02	1.0E-02	0.840	9.7E-04	0.844	0.411
13	4.2E+02	1.2E+03	2.7E+02	1.8E+02	2.0E-02	0.840	1.6E-03	0.826	0.437
14	3.7E+02	1.2E+03		1.5E+02*					0.395*
15	3.5E+02	1.2E+03		1.4E+02*					0.397*

Days	Rpn	Rsol	Rp3	n3	Yo3
20	7.7E+02	1.3E+03	1.1E+03	0.560	3.4E-03
21	8.0E+02	1.2E+03	1.1E+03	0.579	3.2E-03
22	9.4E+02	1.3E+03	1.3E+03	0.597	3.0E-03
24	1.1E+03	1.4E+03	1.3E+03	0.650	2.5E-03
27	1.3E+03	1.5E+03	1.7E+03	0.649	2.3E-03
28	1.3E+03	1.5E+03	1.7E+03	0.655	2.2E-03
30	1.4E+03	1.5E+03	1.7E+03	0.667	2.1E-03
31	1.3E+03	1.5E+03	1.6E+03	0.669	2.1E-03
34	1.3E+03	1.5E+03	1.6E+03	0.681	2.0E-03
36	1.4E+03	1.6E+03	1.7E+03	0.685	1.9E-03
37	1.4E+03	1.7E+03	1.6E+03	0.683	1.9E-03
38	1.5E+03	1.5E+03	1.7E+03	0.688	2.0E-03
42	1.4E+03	1.5E+03	1.6E+03	0.686	2.0E-03
44	1.4E+03	1.5E+03	1.6E+03	0.695	2.0E-03
49	1.5E+03	1.5E+03	1.8E+03	0.705	1.9E-03
57	2.0E+03	1.5E+03	2.4E+03	0.720	1.6E-03
62	2.3E+03	1.5E+03	2.9E+03	0.729	1.5E-03
69	2.3E+03	1.6E+03	2.9E+03	0.731	1.5E-03
72	2.2E+03	1.5E+03	2.6E+03	0.736	1.6E-03
80	1.8E+03	1.5E+03	2.1E+03	0.725	1.6E-03
83	1.9E+03	1.5E+03	2.2E+03	0.728	1.5E-03
87	2.3E+03	1.6E+03	2.8E+03	0.736	1.5E-03
94	2.4E+03	1.6E+03	2.8E+03	0.737	1.5E-03
112	2.7E+03	1.6E+03	3.3E+03	0.754	1.3E-03
121	2.9E+03	1.6E+03	3.7E+03	0.757	1.3E-03
126	2.6E+03	1.6E+03	3.1E+03	0.754	1.3E-03
132	2.7E+03	1.7E+03	3.2E+03	0.753	1.3E-03
135	3.2E+03	1.7E+03	4.1E+03	0.769	1.2E-03
146	3.8E+03	1.7E+03	5.1E+03	0.779	1.1E-03
149	3.0E+03	1.7E+03	4.1E+03	0.742	1.3E-03
155	2.2E+03	1.2E+03	9.4E+03	0.695	2.5E-03

Appendix 2 (continued)

Table A-11: EIS analysis parameters for SP8

SP 8

Days	Rpn	Rsol	R2	R1	Yo2	n2	Yo1	n1	R1/Rpn
1	1.7E+03	7.6E+02	2.1E+03	7.1E+02	5.0E-03	0.820	3.1E-04	0.905	0.428
5	1.3E+03	1.3E+03	1.4E+03	5.0E+02	5.7E-03	0.820	4.2E-04	0.912	0.385
6	1.1E+03	1.3E+03	1.2E+03	3.8E+02	7.2E-03	0.840	5.2E-04	0.910	0.348
8	5.9E+02	1.2E+03	5.9E+02	2.1E+02	1.3E-02	0.800	7.4E-04	0.933	0.348
11	4.4E+02	1.2E+03	3.4E+02	1.5E+02	1.7E-02	0.760	1.5E-03	0.880	0.352
12	3.9E+02	1.3E+03	2.8E+02	1.4E+02	1.9E-02	0.760	1.7E-03	0.858	0.356
13	3.5E+02	1.4E+03	2.9E+02	1.1E+02	2.3E-02	0.700	2.3E-03	0.829	0.316
14	2.8E+02	1.3E+03		1.1E+02*					0.395*
15	3.1E+02	1.4E+03		1.2E+02*					0.397*

Days	Rpn	Rsol	Rp3	n3	Yo3
18	4.8E+02	1.4E+03	5.9E+02	0.602	5.9E-03
19	6.5E+02	1.5E+03	7.5E+02	0.633	5.0E-03
20	8.1E+02	1.3E+03	8.9E+02	0.656	3.9E-03
25	9.9E+02	1.4E+03	1.2E+03	0.698	3.0E-03
26	1.1E+03	1.4E+03	1.3E+03	0.700	2.8E-03
27	1.1E+03	1.4E+03	1.3E+03	0.700	2.7E-03
29	1.2E+03	1.6E+03	1.4E+03	0.704	2.5E-03
32	1.3E+03	1.5E+03	1.5E+03	0.712	2.3E-03
33	1.2E+03	1.5E+03	1.5E+03	0.720	2.3E-03
35	1.4E+03	1.5E+03	1.7E+03	0.726	2.2E-03
36	1.4E+03	1.5E+03	1.7E+03	0.723	2.2E-03
39	1.5E+03	1.5E+03	1.8E+03	0.728	2.1E-03
41	1.7E+03	1.5E+03	2.0E+03	0.738	2.0E-03
42	1.8E+03	1.6E+03	2.1E+03	0.734	2.0E-03
43	1.8E+03	1.6E+03	2.2E+03	0.747	1.9E-03
47	2.2E+03	1.6E+03	2.6E+03	0.763	1.8E-03
49	2.2E+03	1.6E+03	2.8E+03	0.764	1.7E-03
54	2.4E+03	1.5E+03	3.0E+03	0.761	1.6E-03
62	3.0E+03	1.7E+03	4.0E+03	0.768	1.4E-03
67	2.7E+03	1.8E+03	4.0E+03	0.783	1.4E-03
74	3.2E+03	1.7E+03	4.2E+03	0.792	1.4E-03
77	3.2E+03	1.6E+03	4.1E+03	0.794	1.3E-03
85	3.4E+03	1.4E+03	4.4E+03	0.799	1.3E-03
88	3.3E+03	1.4E+03	4.3E+03	0.796	1.3E-03
92	3.8E+03	1.7E+03	4.6E+03	0.794	1.2E-03
99	3.6E+03	1.7E+03	4.7E+03	0.807	1.2E-03
117	3.9E+03	1.7E+03	5.5E+03	0.791	1.2E-03
126	4.3E+03	1.8E+03	5.7E+03	0.813	1.1E-03
131	4.3E+03	1.8E+03	5.8E+03	0.809	1.1E-03
137	4.2E+03	1.8E+03	5.4E+03	0.820	1.1E-03
140	4.4E+03	1.5E+03	5.8E+03	0.832	1.1E-03
151	5.1E+03	1.6E+03	7.0E+03	0.835	1.1E-03
154	5.4E+03	1.7E+03	7.9E+03	0.832	1.1E-03

Appendix 2 (continued)

Table A-12: List of all specimens used for metallography analysis.*ND: non-detectable.

Experimental Name	Internal ID Code	Average (Tov)	Max Average of all frames	Min Average of all frames	STD	Days
pull out 1	Coupon 1	2.45	1.93	1.07	1.26	11
pull out 2	Coupon 2	5.27	2.73	1.67	1.01	25
pull out 3	Coupon 3	5.31	4.43	1.83	1.45	45
pull out 4	Coupon 4	2.12	2.57	0.33	1.32	12
pull out 5	Coupon 5	4.02	2.80	0.87	1.42	26
pull out 6	Coupon 6	4.62	4.03	1.90	1.53	46
D-hutch 4	SP 4	3.70	3.10	1.57	1.46	35
D-hutch 3	SP 3	3.83	2.73	1.73	1.40	36
D-hutch 2	SP 2	5.36	3.81	8.45	0.82	27
D-hutch 1	SP 1	5.39	6.32	4.65	1.19	37
D-hutch 2a	Extra	ND	ND	-	-	6

Appendix 2 (continued)

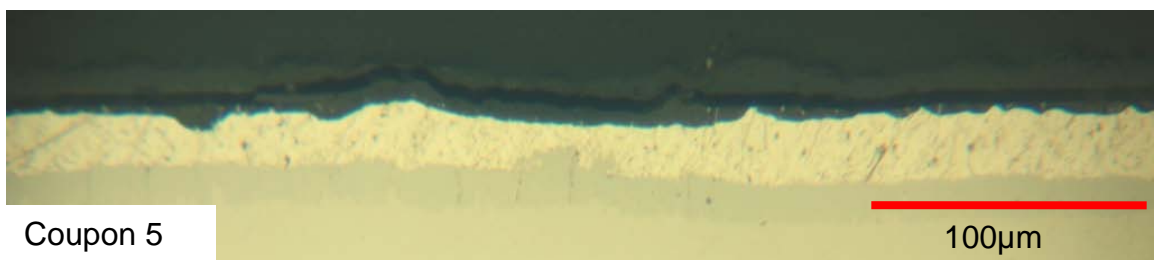
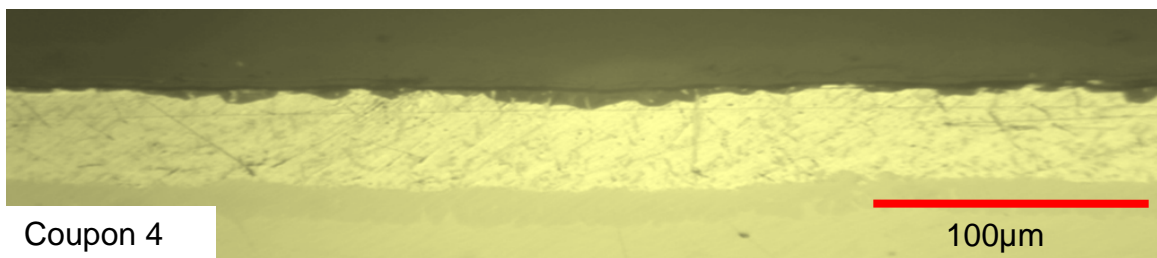
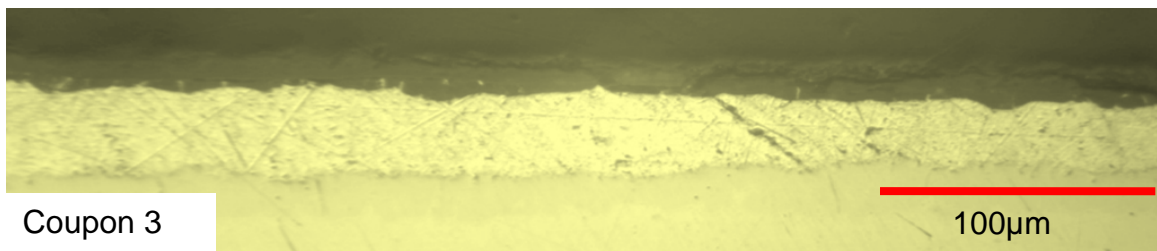
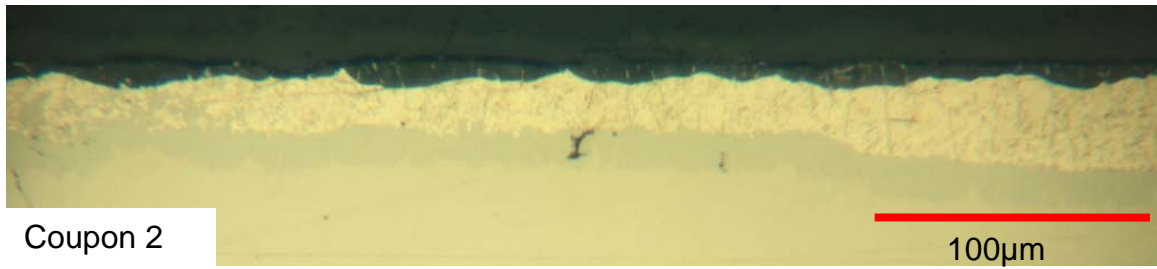
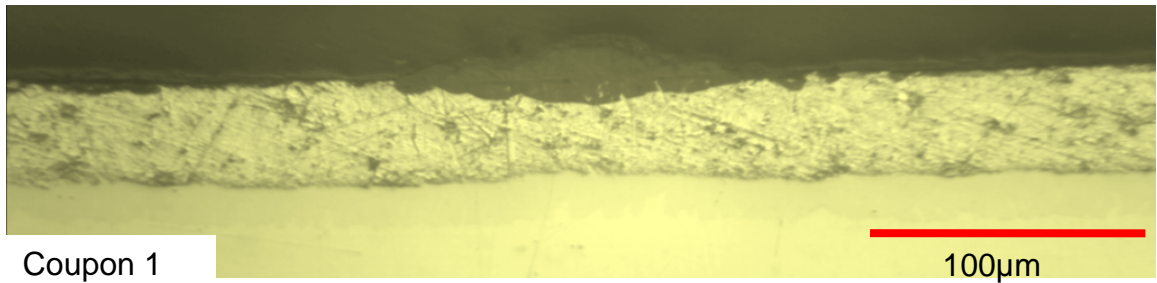


Figure A-7: Representative metallographic cross section used for direct coating loss measurements.

Appendix 2 (continued)

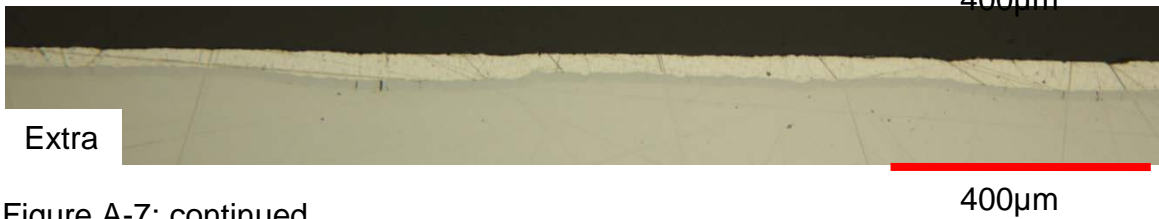
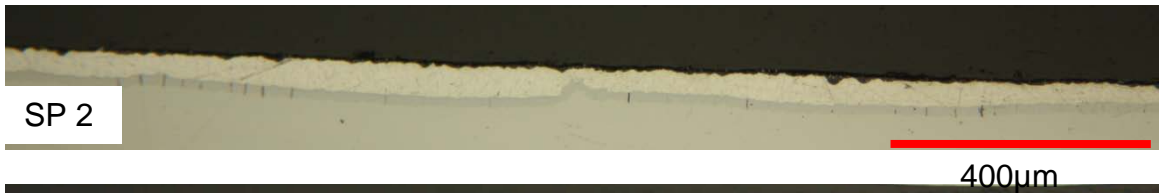
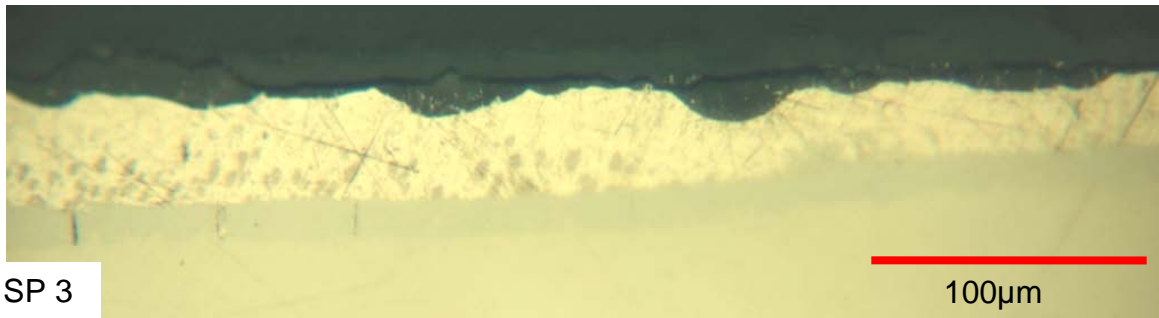
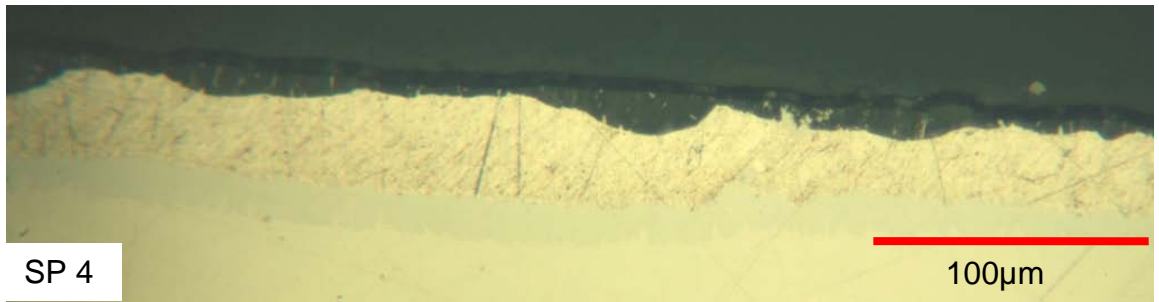
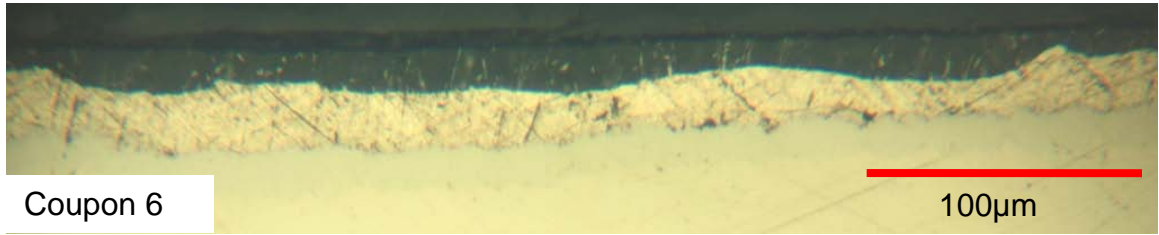


Figure A-7: continued

Appendix 2 (continued)

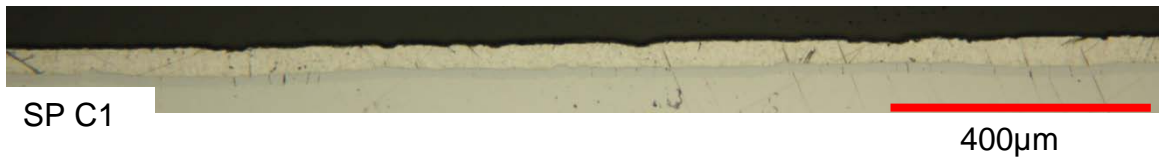
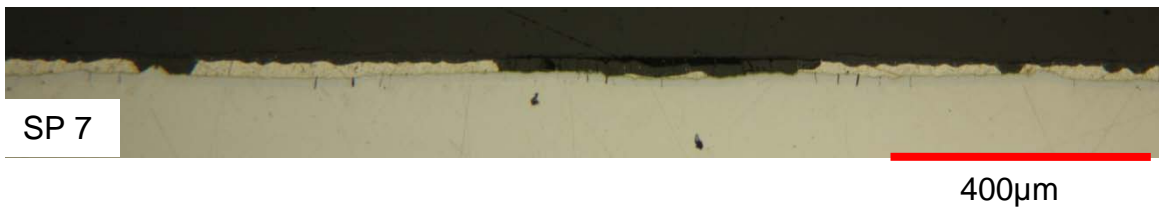
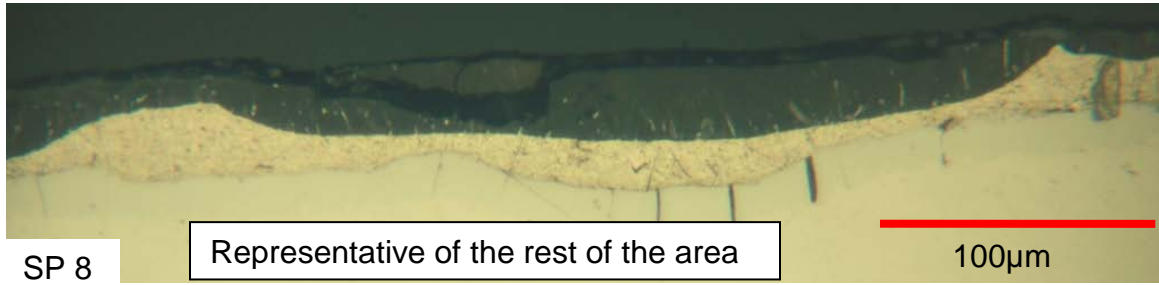
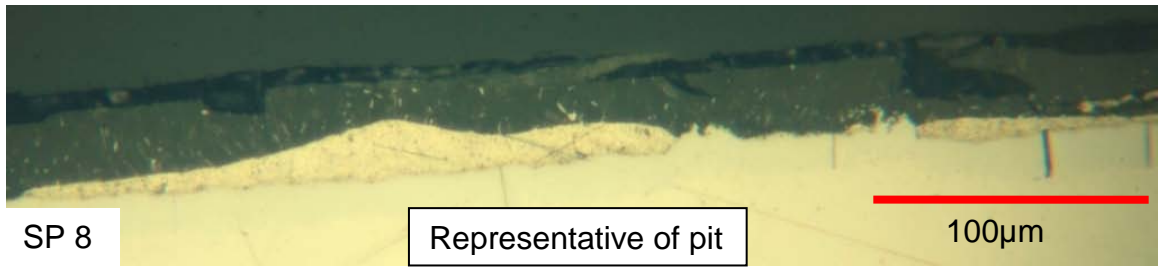


Figure A-7: continued

Appendix 2 (continued)

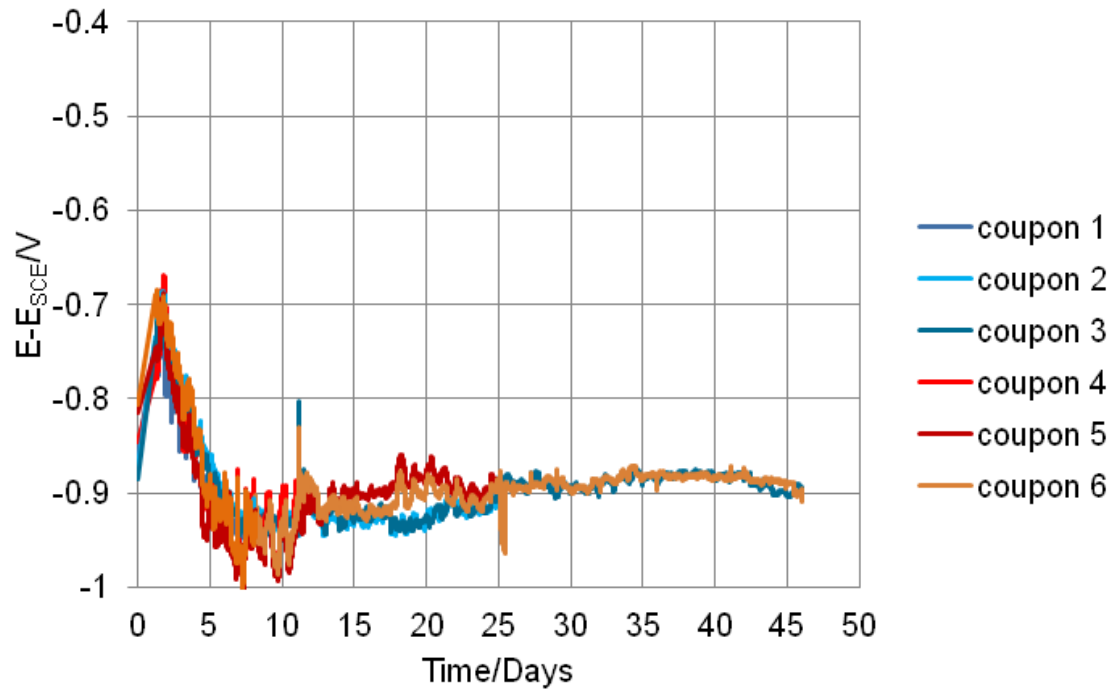


Figure A-8: Potential evolution for six coupon specimens (Coupon 1 - 6 listed in Table 5). Potentials were measured by an automated device (USB-1608FS MC Data Acquisition).

Appendix 3: Corrosion and Simulated Severe Manufacturing Distress



Figure A-9: Specimens with exposed edges (Bottom) and their counterpart specimen (Top) (two years of exposure). Specimens on the left side were exposed to solution S (Cell#1) and specimens on right side were exposed to solution S+ (Cell#3).

Appendix 3 (continued)

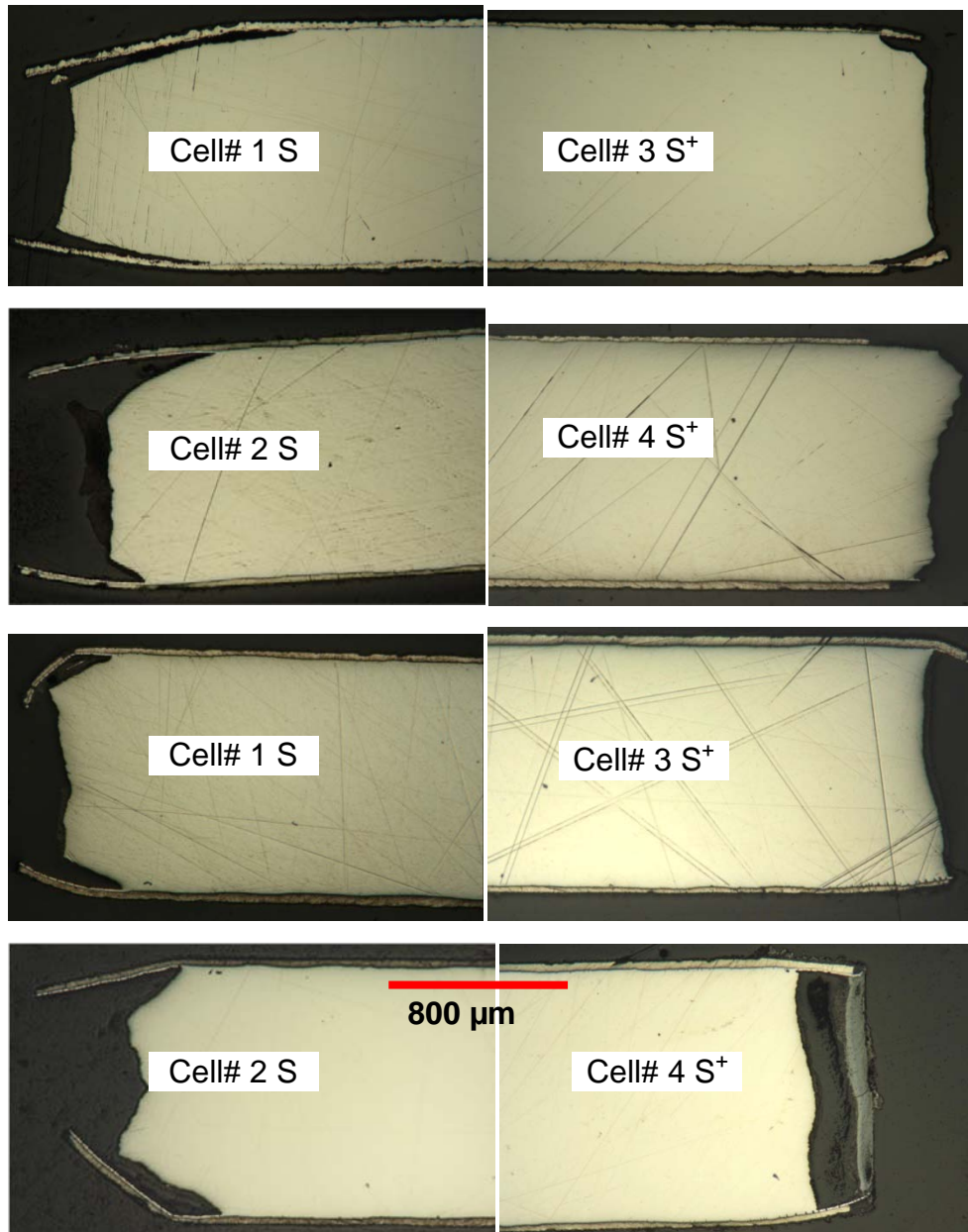


Figure A-10: Metallographic cross section of the edges of aluminized steel specimens in solution S (Left) and S⁺ (Right).

Appendix 3 (continued)

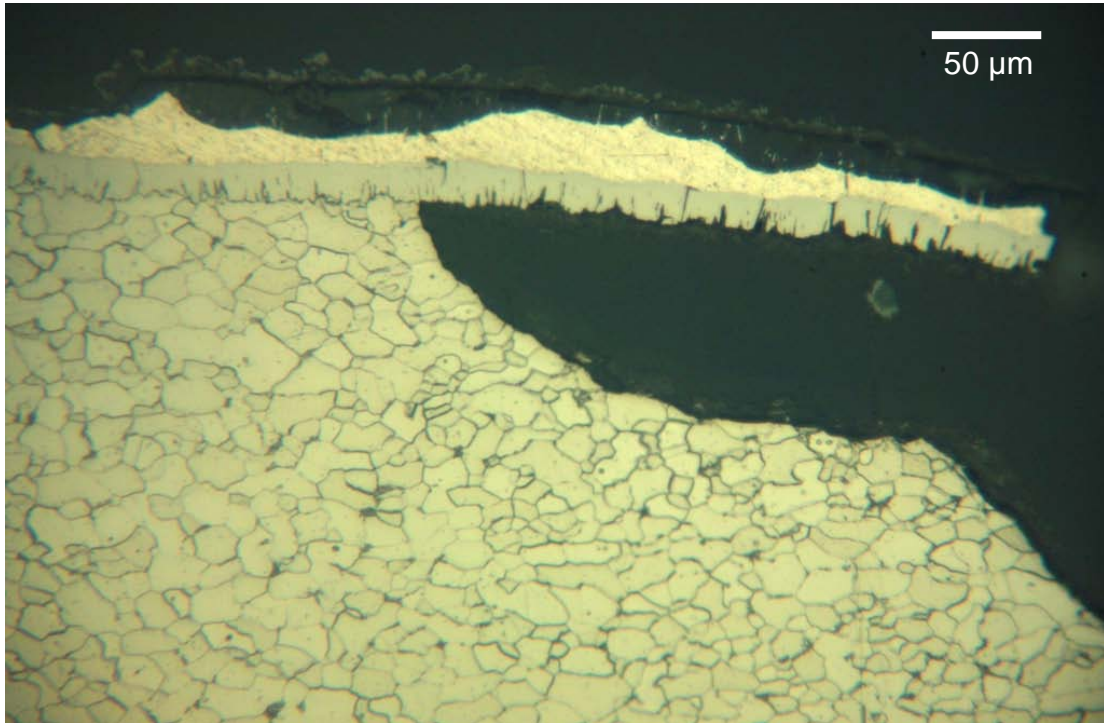


Figure A-11: Metallographic cross section (shown for Cell#3 S⁺) after etching with 1% Nital solution.

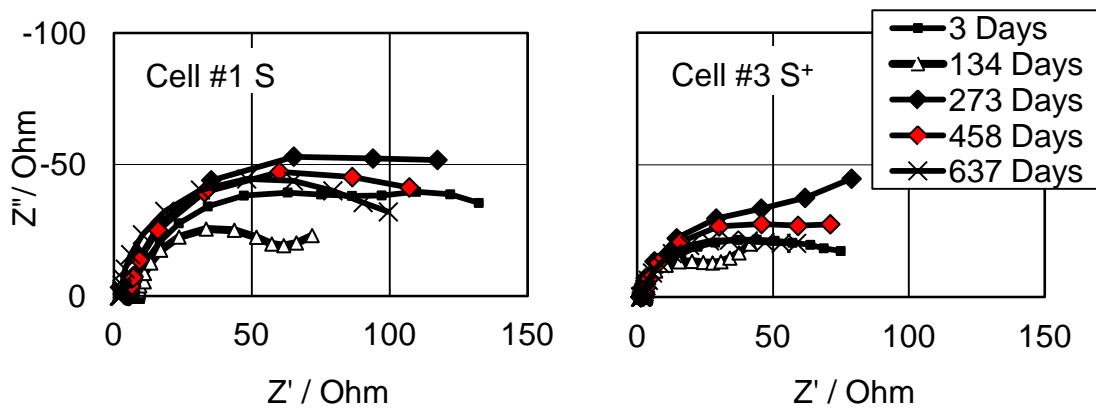


Figure A-12: Representative nyquist plot of the EIS response of exposed edge specimens in S (Left) and S⁺ (Right) solutions. Shown for Cell #1 and Cell #3. [10 mHz (last datum) to 100 kHz; 3 data/decade; lines joining data are shown for clarity but do not represent a data fit].

Appendix 4: Limestone Composition Analysis by X-ray Fluorescence Spectrometry

Table A-13: Limestone composition*

<u>Analyte</u>	<u>Weight %</u>		
SiO ₂	0.50		
Al ₂ O ₃	0.17	T-Alk (Na ₂ O + 0.658K ₂ O)	0.03
Fe ₂ O ₃	0.06		
CaO	54.28	<u>Calculated Compounds</u>	
MgO	0.60	Ca as CaCO ₃	96.88
SO ₃	0.04	Mg as MgCO ₃	1.26
Na ₂ O	0.03	Calculated Carbonates as CO ₂	43.26
K ₂ O	0.01	L.O.I. / CO ₂ Balance	1.02
TiO ₂	0.01		
P ₂ O ₅	0.01	<u>Calculated Compounds - Mg as Dolomite</u>	
Mn ₂ O ₃	<0.01	Mg as CaMg(CO ₃) ₂	2.76
SrO	0.08	Residual Ca as CaCO ₃	95.38
Cr ₂ O ₃	<0.01		
ZnO	<0.01		
BaO	<0.01		
L.O.I. (950°C) ²	43.95		
<u>Total</u>	<u>99.75</u>		

*Analysis performed by CTL Group in accordance with ASTM C1271.

Appendix 5: Corrosion of Plain Corrugated Galvanized Steel Pipe Joining SRAP Segments

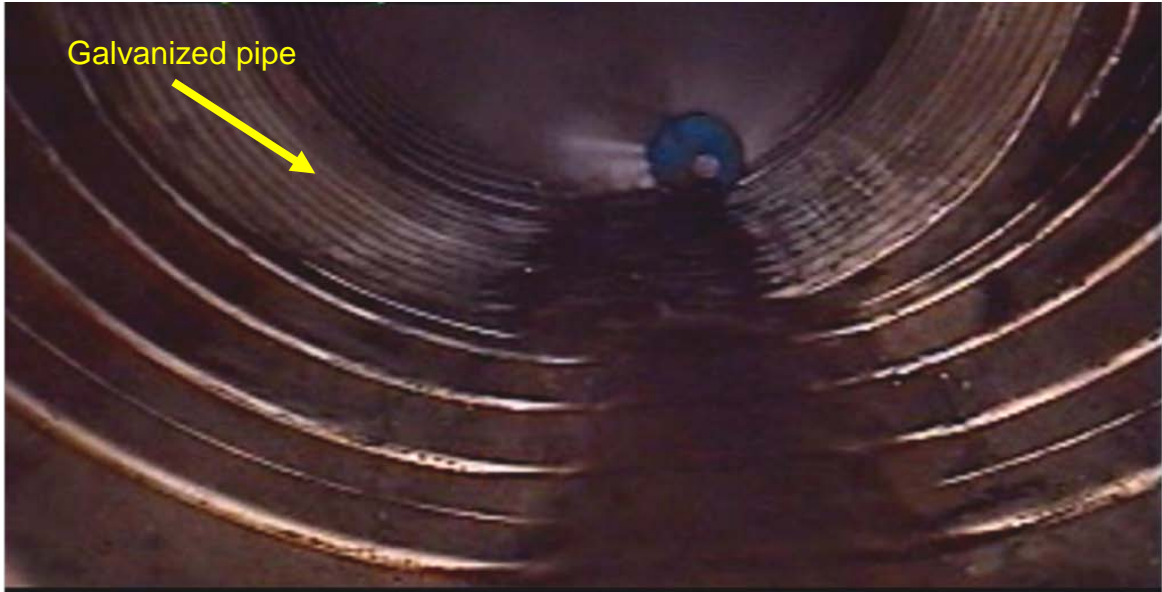


Figure A-13: Snap shot of a video from inside a pipe that shows plain corrugated galvanized pipe is joining the segments of SRAP.

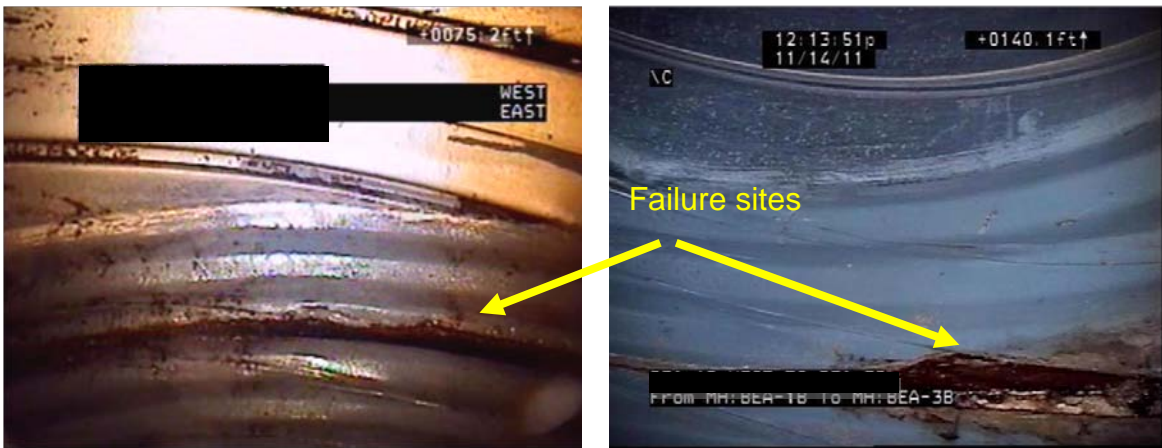


Figure A-14: Snap shots of a video from inside a pipe with severe corrosion of plain corrugated galvanized pipes.

ABOUT THE AUTHOR

In December 2007, Mersedeh Akhoondan completed her combined bachelor's and master's degree in Civil Engineering at the University of South Florida. She specialized in Structures and Materials Engineering with an emphasis on the environmental compatibility and durability of construction materials. Her MS thesis addressed the effect of mechanical forming on the corrosion performance of aluminized steel. Immediately afterwards, she started doctoral work, also at USF, on the electrochemical corrosion of coated steel in aggressive natural waters with added emphasis on the corrosion resistance of novel concrete reinforcing alloys. The work was largely supported by the Florida Department of Transportation, and addresses key issues in national infrastructure durability. The findings from her work have already impacted FDOT practice in the selection of pipe backfill material.